



Copyright Undertaking

This thesis is protected by copyright, with all rights reserved.

By reading and using the thesis, the reader understands and agrees to the following terms:

1. The reader will abide by the rules and legal ordinances governing copyright regarding the use of the thesis.
2. The reader will use the thesis for the purpose of research or private study only and not for distribution or further reproduction or any other purpose.
3. The reader agrees to indemnify and hold the University harmless from and against any loss, damage, cost, liability or expenses arising from copyright infringement or unauthorized usage.

IMPORTANT

If you have reasons to believe that any materials in this thesis are deemed not suitable to be distributed in this form, or a copyright owner having difficulty with the material being included in our database, please contact lbsys@polyu.edu.hk providing details. The Library will look into your claim and consider taking remedial action upon receipt of the written requests.

**INVESTIGATION ON SUPERHYDROPHOBIC
MICRO/NANO-STRUCTURED SURFACES
FABRICATED BY ULTRAPRECISION
MACHINING AND HYDROTHERMAL
SYNTHESIS FOR SELF-CLEANING AND
CORROSION RESISTANCE**

FU YEXIANG

PhD

The Hong Kong Polytechnic University

2022

The Hong Kong Polytechnic University

Department of Industrial and Systems Engineering

**Investigation on Superhydrophobic Micro/nano-
structured Surfaces Fabricated by Ultraprecision
Machining and Hydrothermal Synthesis for Self-
cleaning and Corrosion Resistance**

FU Yexiang

A thesis submitted in partial fulfillment of the
requirements for the degree of Doctor of Philosophy

July 2021

CERTIFICATE OF ORIGINALITY

I hereby declare that this thesis is my own work and that, to the best of my knowledge and belief, it reproduces no material previously published or written, nor material that has been accepted for the award of any other degree or diploma, except where due acknowledgement has been made in the text.

_____ (Signed)

_____ Fu Yexiang (Name of student)

Abstract

Superhydrophobic surfaces have attracted researchers' interest because of the academic aspects and the industrial applications. Many types of superhydrophobic surfaces been developed and investigated in many application fields including self-cleaning, anti-fogging, drag reduction, corrosion resistance, *etc.* In these studies, the hierarchical surfaces integrating the microstructures and the nanostructures are believed to possess enhanced hydrophobicity and could present some superior properties in certain applications. However, research related to superhydrophobic micro/nano-structured surfaces is still limited and incomplete. The effect of the integration of micro and nano structures has not been fully investigated and is difficult to determine simply through basic contact angle measurements. Therefore, the role of superhydrophobic micro/nano structures in application fields including self-cleaning and corrosion resistance is well worth studying and could provide additional ways to evaluate hydrophobicity and help achieve a better understanding of wetting mechanisms.

In this thesis, the theoretical and experimental study on superhydrophobic micro/nanostructured surfaces can be divided into three parts. In the first part, two types of micro/nano-structured surfaces, i.e., the Cu₂O-STA microgroove surface and the NiO-FAS-17 microgroove surface were developed, and the wettability evaluated. The micro/nano-structured surfaces were fabricated by integrating ultraprecision machining (UPM) and hydrothermal synthesis. The UPM fabricated microgrooves were the base structure on which a thin layer of Cu₂O or NiO micro/nanostructures with stearic acid (STA) or FAS-17 treatment was prepared by hydrothermal synthesis, thus forming hierarchical structured surfaces. Contact

angle measurements were conducted on the prepared surfaces and satisfactory hydrophobicity was achieved. The Cu₂O-STA microgrooves presented a contact angle of $143.2^{\circ} \pm 1.2^{\circ}$ while the NiO-FAS-17 microgrooves presented a contact angle of $161.3^{\circ} \pm 1.2^{\circ}$ and contact angle hysteresis of $3.3^{\circ} \pm 1.2^{\circ}$.

In the second part, the Cu₂O-STA microgroove surfaces were investigated for corrosion resistance. Electrochemical characterization was performed through the techniques of electrochemical impedance spectrometry and Tafel polarization to reflect the corrosion resistance properties. The electrochemical measurements showed that the hydrophobic Cu₂O-STA film on flat substrates presented good corrosion resistance. The performance of the Cu₂O-STA microgroove surfaces was even better with improved impedance and reduced corrosion current density. This reveals an enhancement of hydrophobic corrosion resistance via introduction of UPM fabricated microgrooves to form a hierarchical architecture.

In the third part, water droplet bouncing experiments were performed on superhydrophobic NiO-FAS-17 microgroove surfaces to study the self-cleaning effect. The process of droplet impact was recorded to determine properties which included the first rebound height, restitution coefficient, water-surface contact time and spreading factor against the governing parameter Weber number (We) for bouncing behavior analysis. The results reflected good superhydrophobic self-cleaning effects on both the NiO-FAS-17 coated flat surface and the NiO-FAS-17 microgroove surface, while a larger first rebound height and stronger tendency of droplet break-up were recorded on the latter one. This indicates that the micro/nano-structured surfaces possess an improved hydrophobic self-cleaning effect.

The originality and significance of the present research lie in the following aspects: (i) a novel method integrating UPM and hydrothermal synthesis is developed to fabricate superhydrophobic micro/nano-structured surfaces; (ii) enhancement of micro/nano-structured surfaces in hydrophobic corrosion resistance is achieved; (iii) enhancement of micro/nano-structured surfaces over nanostructures in regard to the self-cleaning effect is revealed through analysis in droplet bouncing behaviors. Both (ii) and (iii) can provide the means to compare the hydrophobicity of micro/nano-structured surfaces and nanostructured surfaces with the same surface chemical composition and can improve the understanding of wetting of micro/nano-structures.

Publications arising from this study

Journal papers

1. Fu, Y., Zhao, Z., Yip, W., & To, S. (2020). Novel fabrication of a hierarchical structured surface with improved corrosion inhibition by using hydrothermal synthesis and ultraprecision machining. *Surface and Coatings Technology*, 385, 125432.
2. Zhou, R., Fu, Y., Chao, K.-A., & Cheng, C.-H. (2019). Green synthesis of nanoarchitected nickel fabrics as high performance electrodes for supercapacitors. *Renewable Energy*, 135, 1445-1451.
3. Fu, Y., Zhao, F., Zhao, Z., Tang, H., To, S & Cheng, C. Water droplet bouncing on a hierarchical superhydrophobic surface fabricated by hydrothermal synthesis and ultraprecision machining (under review).

Conference paper

1. Fu, Y., To, S. (2019). Investigation of a hierarchical Cu₂O-STA grooved hydrophobic surface on its corrosion resistance properties. 8th International Conference of Asian Society for Precision Engineering and Nanotechnology, Matsue, Japan.

Acknowledgements

First of all I would like to express my sincere gratitude to my chief supervisor Prof Sandy To, a knowledgeable professor from the Hong Kong Polytechnic University. Her patience, encouragement and valuable guidance have been supporting me during my PhD study. I am grateful to my co-supervisor Dr Ching-Hsiang Cheng for his continuous guidance and support.

Besides my supervisor and co-supervisor, I am thankful for the support from the group members Dr Waisze Yip, Dr Thomas Cheng, Dr Zhanwen Sun, and Dr Zejia Zhao. They have been sharing their experience and knowledge and providing valuable advice. I would like to show my thanks to the staff members Mr. Ka Chun Cheung, Mr. Tai Wa Chung, Mr. David Lai, Mr. Jon Wong, Mr. Fan Tsz Hin and Ms. May Chun from the State Key Laboratory of Ultra-precision Machining Technology. They provided me with their technical support in experiment issues. I am grateful to my senior mates Dr Ruitao Zhou and Dr Hui Tang, who have helped me a lot in some technical problems. I would also express special thanks to my workmates Dr Yang Li, Dr Wei Zai and Dr Fuwang Zhao for their kind instructions.

Special thanks go to the Research Committee of the Hong Kong Polytechnic University for its financial support of my PhD project.

Finally, I would like to express my thanks to Jiongjiongxion and my family for their support and understanding throughout the years I have been far from home for my studies.

Table of contents

Abstract	i
Publications arising from this study	iv
Acknowledgements	v
Table of contents	vi
List of figures	ix
List of tables	xvi
Chapter 1 Introduction	1
1.1 Background	1
1.2 Research objectives	2
1.3 Organization of the thesis	3
Chapter 2 Literature review	4
2.1 Introduction to superhydrophobicity	4
2.2 Wetting of solid surfaces	7
2.2.1 Static wetting properties	7
2.2.2 Dynamic wetting properties	12
2.3 Artificial superhydrophobic surfaces with micro/nano-structures	14
2.3.1 Top-down approaches	15
2.3.2 Bottom-up approaches	19
2.3.3 Ultraprecision machining	24
2.3.4 Hydrothermal synthesis	28
2.4 Hydrophobic self-cleaning	30
2.4.1 Development of surfaces with self-cleaning effect	31
2.4.2 Measurements of contact angles	33
2.4.3 Water droplet bouncing behaviors on superhydrophobic surfaces	35

2.5 Hydrophobic corrosion resistance	42
2.6 Summary	45
Chapter 3 Methodology	47
3.1 Ultraprecision machining of microgrooves	47
3.2 Hydrothermal synthesis of micro/nano-structures	50
3.3 Electrochemical characterization	54
3.4 Contact angle measurement.....	56
3.5 Water droplet bouncing experiments	57
Chapter 4 Investigation of micro/nano-structured surfaces fabricated by UPM and hydrothermal synthesis on surface wettability	59
4.1 Introduction	59
4.2 Experimental details	60
4.2.1 Ultraprecision machining of microgroove surfaces.....	60
4.2.2 Hydrothermal synthesis of Cu ₂ O layer.....	62
4.2.3 Hydrothermal synthesis of NiO layer.....	63
4.2.4 Characterization methods	64
4.3 Results and discussion.....	65
4.3.1 Topography of UPM fabricated microgrooves.....	65
4.3.2 Morphology of micro/nano crystals acquired by hydrothermal synthesis	69
4.3.3 Surface wettability and anisotropy	75
4.4 Concluding remarks	91
Chapter 5 Hydrophobic corrosion resistance of micro/nano-structured surfaces	93
5.1 Introduction	93

5.2	Experimental details	95
5.3	Results and discussion	98
5.3.1	Characterization of the Cu ₂ O-STA microgrooves	98
5.3.2	Corrosion behaviors of the Cu ₂ O-STA microgrooves	101
5.4	Concluding remarks	108
Chapter 6 Water droplet bouncing behaviors on superhydrophobic micro/nano-structured surfaces		110
6.1	Introduction	110
6.2	Experimental details	111
6.3	Theoretical analysis for droplet impact	113
6.3.1	The mass-spring system of the bouncing process	113
6.3.2	Energy dissipation	117
6.3.3	Droplet shape analysis	119
6.4	Results and discussion	120
6.4.1	Droplet bouncing behaviors on less hydrophobic surfaces	122
6.4.2	Droplet bouncing behaviors on the NiO-FAS-17 microgroove surfaces	125
6.4.3	Anisotropy of the NiO-FAS-17 microgroove surfaces	139
6.4.4	Energy dissipation in the bouncing process	140
6.5	Concluding remarks	144
Chapter 7 Conclusions and suggested future work		147
7.1	Overall conclusions	147
7.2	Suggested future work	150
Appendices		153
References		154

List of figures

Fig. 2.1 (a) An SEM image of a lotus leaf surface and (b) the zoom-in view of a single papilla.	6
Fig. 2.2 SEM images of a rice leaf with an anisotropic tendency. The inset shows the magnified image of a single papilla. The arrow points out the direction the hydrophobic papillae are distributed.....	7
Fig 2.3 Schematic of a liquid drop showing the terms in Young's equation.	8
Fig. 2.4 Schematic of Wenzel mode on a rough groove surface as an example..	9
Fig. 2.5 Schematic of Cassie-Baxter mode on a rough groove surface as an example.	10
Fig. 2.6 The apparent contact angle versus equilibrium contact angle derived from the Wenzel mode and the Cassie-Baxter mode.....	11
Fig. 2.7 (a) Schematic of the microscale grooves and the velocity field. (b) Flow in the microchannel with grooved walls.	17
Fig 2.8 SEM images of the PDMS microhole surface. This picture is reprinted from Kashaninejad, Nguyen, & Chan, 2012.....	18
Fig 2.9 SEM images of typical microchannels fabricated by laser texturing under different energy density. Picture reprinted from reference Gregorčič, Šetina-Batič, & Hočevár, 2017.....	19
Fig. 2.10 (a) SEM images of the prepared petal-like zinc surface in a large area. (b) The picture of water and oil droplets on the superhydrophobic surface. (c) Contact angles of water (left) and oil (right) droplets. Reprinted from reference Meng, Wang, Xi, Tang, & Jiang, 2008.....	20
Fig. 2.11 An SEM image of PTFE microspheres prepared by electrospaying. Reprinted from Burkarter <i>et al.</i> , 2007.....	21

Fig 2.12 SEM images of oxide crystals prepared under different hydrothermal bath concentrations and heating temperatures. Reprinted from Song <i>et al.</i> , 2010.	22
Fig 2.13 SEM images under three magnifications presenting nanostructures on flat, micropillars and silicon-lotus wax hierarchical structures. Reprinted from Jung & Bhusan, 2010.	23
Fig. 2.14 The SEM image of a silicon nanogrates with approximately 230 nm pitch and 500 nm depth. The inset shows the apparent contact angle of water about 150°. Reprinted from reference C.-H. Choi, <i>et al.</i> , 2006.	24
Fig. 2.15 Sinusoidal grid microstructures viewed under an optical microscope fabricated at different spindle speed and feed rate.....	27
Fig. 2.16 Top view of a water drop on the (a) flat, (b) microgroove and (c) micropillar COC surface.	27
Fig. 2.17 Typical hydrothermally prepared metal oxide nanostructures (a) Co_3O_4 (b) ZnO (c) TiO_2 and (d) CuO	29
Fig. 2.18 Schematic diagram of (a) the sessile drop method and (b) the Wilhelmy method for dynamic angles measurement.....	34
Fig. 2.19 The water droplet in motion illuminated by a continuous lamp. The plane where the drop lands is slightly tilted to reveal the whole trajectory. The vertical scale of the whole picture is 1 cm.	37
Fig. 2.20 Images of outcomes of normal impact of water droplets on a solid dry surface	39
Fig. 2.21 Dynamic interactions of droplets with different surfaces. (a) microtextured surfaces with large spacing, (b) microtextured surfaces with small	

spacing, (c) hierarchical textured surface and (d) nanoporus surface in Varanasi's work (Varanasi, Deng, Hsu, & Bhate, 2009).....	40
Fig. 2.22 A schematic diagram of corrosion resistance improved by superhydrophobicity	44
Fig. 3.1 Images of (a) Moore Nanotech 350FG and (b) experimental setup for machining.....	48
Fig. 3.2 The image of the tip of the facet diamond tool under an optical microscope	49
Fig. 3.3 The process of hydrothermal synthesis.....	51
Fig. 3.4 The schematic of a three-electrode electrochemical cell.....	55
Fig. 4.1 The schematic diagram to show the sequence to fabricate a single microgroove	62
Fig. 4.2 The images of the machined surface exactly after groove shape formation. Distinct distorted parts could be seen at the edge of the grooves	67
Fig. 4.3 Surface profile acquired by the interferometer. (a) the 3D plot of the copper microgrooves, (b) cross-section view perpendicular to the groove direction of copper microgrooves and (c) cross-section view of microgrooves after coated with cuprous oxide.....	69
Fig. 4.4 SEM images of cuprous oxide on copper substrate prepared under different heating temperature (a) 90°C(b)110°C and (c)130°. The bath concentration is 20mM and the heating time is 2h. In some images the larges needles are free oxide sediments that are not washed away.	71
Fig. 4.5 SEM images of cuprous oxide on copper substrate prepared under different bath concentrations (a)5mM (b) 10mM and (c) 20mM. The temperature	

is 90°C and the heating time is 6h. In some images the larges needles are free oxide sediments that are not washed away. 72

Fig. 4.6 XRD of prepared Cu₂O film on copper substrate..... 73

Fig. 4.7 The NiO nanoflake layer observed under the SEM. The magnified (×1000) view of sample from (a) 20 mM hydrothermal bath, the zoom-in (×10000) view of sample from (b) 4 mM hydrothermal bath, (c) 20 mM hydrothermal bath and (d) 100 mM hydrothermal bath..... 74

Fig. 4.8 The schematic showing the geometric terms of the microgrooves..... 76

Fig. 4.9 The droplets on microgroove surfaces viewed from different directions under a goniometer (a) 5-30 microgroove surface (b) 15-30 microgroove surface (c) 30-30 microgroove (d) 60-30 microgroove (e) 100-30 microgroove..... 78

Fig. 4.10 The images of 5 μL droplets deposited on varied microgroove copper surfaces (a) 5-30, (b) 15-30, (c) 30-30, (d) 60-30, (e) 100-30 and (f) flat under the optical microscope. 79

Fig. 4.11 The images of 5 μL droplets deposited on the micropillar copper surface and the 30-30 microgroove copper surface. The droplet shape changes with the distribution of micropatterns as water penetrates into the patterns..... 80

Fig. 4.12 Images of the static contact angle of (a) bare copper, Cu₂O-STA coated (b) flat copper plate, (c) 15-30 microgrooves, (d) 30-30 microgrooves, (e) 60-30 microgrooves and (f) 100-30 microgrooves..... 83

Fig. 4.13 The surface profile of (a) ELD prepared nickel layer on polished copper surface, (b) polished T2 copper, (c) Cu₂O coating and (d) NiO coating 84

Fig. 4.14 Snapshots of the static contact angle of ELD prepared nickel coated flat copper surface 85

Fig. 4.15	Snapshots of the contact angle of Ni-FAS-17 coated (a) flat copper surface and grooved surface from (b) parallel direction and (c) orthogonal direction	86
Fig. 4.16	Snapshots of the advancing contact angle of NiO-FAS-17 coated (a) flat surface, (c) grooved surface from the orthogonal direction and (e) the parallel direction, and the receding angle of NiO-FAS-17 coated (b) flat surface, (d) grooved surface from the orthogonal direction and (f) the parallel direction	90
Fig. 5.1	The schematic diagram of the fabrication of the hierarchical Cu ₂ O-STA modified microgroove surface	96
Fig. 5.2	(a) the schematic diagram of microgrooves surface generation and (b) the cross-section view of the trapezoidal grooves	97
Fig. 5.3	SEM images of (a) copper microgrooves fabricated by UPM, Cu ₂ O-STA film on (b) flat copper plate and (c) copper microgrooves, cross-section view of Cu ₂ O-STA film and (e) a photo of a sealed sample.....	99
Fig. 5.4	The contact angles of (a) flat copper plate and (b) Cu ₂ O-STA film on copper microgrooves and (c) the air layer of Cu ₂ O-STA film on copper microgrooves immersed in water	101
Fig. 5.5	Nyquist (a) and Bode (b) plots of the bare Cu, Cu ₂ O-STA modified flat copper and Cu ₂ O-STA modified grooved copper. The inset of Nyquist plots is the amplification of the high frequency part.....	104
Fig. 5.6	The equivalent electric circuits for modeling the EIS spectra of (a) bare copper, bare copper microgrooves, (b) the Cu ₂ O-STA modified flat copper and grooved copper with 3.5 wt.% NaCl solution as the electrolyte.....	104
Fig. 5.7	Potentiodynamic polarization curves in 3.5 wt.% NaCl solution.....	106

Fig. 5.8	Potentiodynamic polarization curves in 3.5 wt.% NaCl solution of samples after 7 days or 14 days immersion in 3.5% NaCl aqueous solution. ...	107
Fig. 6.1	The schematic of impact of water droplets.....	113
Fig. 6.2	The schematic diagram showing comparison between the mass-spring system and the bouncing droplet.....	114
Fig. 6.3	Images of a typical case of the water droplet bouncing movement on the NiO-FAS-17 coated superhydrophobic surface.....	122
Fig. 6.4	Images of a water droplet performing one rebound and the subsequent oscillating on the copper micropillar surface.....	124
Fig. 6.5	Images of a water droplet oscillating on the Ni-FAS-17 coated flat copper surface.....	124
Fig. 6.6	Images of three droplet bouncing types. The fragmented water drops are circled in red.	127
Fig. 6.7	Temporal evolution of the spreading factor for impinging water droplets on NiO-FAS-17 coated flat copper surfaces at different Weber numbers.....	128
Fig. 6.8	Temporal evolution of the spreading factor for impinging water droplets on different NiO-FAS-17 coated superhydrophobic surfaces	129
Fig. 6.9	The contact time of the first bounce of the 7.7 μ L droplet on the NiO-FAS-17 coated 30-30 microgroove surface	131
Fig. 6.10	Diagram of the first rebound height (black dots), the restitution coefficient (red dots) and the restitution coefficient predicted from the mass-spring model (blue dots) against We of water droplets impacting on the NiO-FAS-17 coated flat copper surface	133
Fig. 6.11	Diagram of first rebound height against We of the water droplet impacting on NiO-FAS-17 coated 30-30 microgroove copper surface	135

Fig. 6.12	Diagram of first rebound height against We of the water droplet impacting on NiO-FAS-17 coated 5-30 microgroove copper surface	136
Fig. 6.13	Column chart of first rebound height against We for comparison of different types of surfaces	137
Fig. 6.14	Comparison of the fragmentation of bouncing drops on (a) the NiO-FAS-17 coated flat copper surface and (b) the NiO-FAS-17 coated 30-30 microgroove copper surface under $We = 11.1$	138
Fig. 6.15	The maximum diameter versus We of the water droplet impacting on NiO-FAS-17 coated flat copper surface	142
Fig. 6.16	The maximum diameter and the maximum contact diameter versus We of the water droplet impacting on NiO-FAS-17 coated 30-30 microgroove copper surface	142
Fig. 6.17	Comparison of total energy and several ways of energy dissipation during the first rebound versus We	144

List of tables

Table. 4.1	The geometric parameters of a microgroove surface with different groove depth.....	65
Table. 4.2	The geometric parameters of the 18 μm -depth microgroove surfaces with different groove period	66
Table 4.3	Wetting properties of different Ni coated surfaces	87
Table 4.4	Dynamic wetting properties of NiO-FAS-17 coated surfaces	88
Table 5.1	Fitted parameters of EIS spectra	104
Table 5.2	Electrochemical parameters from polarization curves of different samples.....	106
Table 5.3	Electrochemical parameters from polarization curves of different samples.....	108
Table. 6.1	The maximum diameter of the droplets impacting on different sample surfaces	140

Chapter 1 Introduction

1.1 Background

Superhydrophobic (SHPO) surfaces have been of great interest to researchers for the academic pursuits and industrial applications. The conception comes from the water-repellent properties of the lotus leaf. Water keeps its shape as a droplet on the leaf surface and easily rolls off when the leaf is inclined. In the 1970s the introduction of scanning electron microscopy (SEM) revealed the microstructure of the lotus leaf surface and provided explanation to this phenomenon. By mimicking the SHPO materials discovered in nature, researchers have found ways to improve the hydrophobicity of artificial surfaces. The routes for SHPO surfaces fabrication could be grouped into two categories: creating rough geometric structures on hydrophobic surfaces; modifying rough surfaces with low surface energy materials.

Hydrophobic and superhydrophobic surfaces have been investigated for a wide variety of applications including self-cleaning properties and corrosion resistance. There are many types of techniques used to fabricate such functional surfaces. Laser texturing, lithography, and ultraprecision are typical methods for regularly patterned surfaces. Electrodeposition, etching, hydrothermal methods, anodization, and sol-gel methods are main ways to prepare randomly structured micro/nano materials. Previous work combining these two categories of methods to prepare hierarchical hydrophobic layers is still quite limited in terms of the applications of self-cleaning and corrosion resistance. There is lack in the study of hierarchical structures to compare the effect in water repellency with nanostructured surfaces of the same surface composition. Most hydrophobic

surfaces for anticorrosion thus far were based on coatings with irregular rough structures and do not possess precise control on dimensions and shapes. Research work on hierarchical structured superhydrophobic surfaces integrating microstructured base and nanostructured secondary layer is also incomplete. Basic contact angle measurements are not adequate to elucidate the effect of micro/nano hierarchical structures in comparison with individual microstructure or nanostructures. Further investigation is needed to provide abundant results to better understand the mechanism of superhydrophobicity along with its applications in corrosion resistance and self-cleaning.

To overcome these limitations, we manufactured metal oxide based hierarchical surfaces on the base of copper by combing ultraprecision machining with hydrothermal synthesis in this research work. The ultraprecision machining process enables the formation of regularly shaped copper microgrooves. The hydrothermal synthesis yields a thin layer of rough micro/nanostructure on the surface of the microgrooves, achieving a hierarchical structure. The integration will possibly enhance the water repellency and corrosion resistance compared with the surfaces with a single structure.

1.2 Research objectives

In this study, we aim at investigating the self-cleaning and corrosion resistance of a hierarchical structured surface, where nanostructures are grown on a regularly patterned microstructure. We are to fabricate the microgroove pattern on a smooth copper plate using ultraprecision machining. Rectangular shaped Cu_2O particles or NiO nanoflakes are then deposited on the machined surface by

hydrothermal synthesis. The enhancement of the hierarchical structures in self-cleaning and corrosion resistance will be investigated. To accomplish the aim, several sub-steps will be performed, and respective objectives are listed as follows:

- To fabricate the microgroove pattern on a flat smooth surface and modify Cu_2O crystals on the grooves to acquire a Cu_2O -STA microgroove hierarchical structure with good hydrophobicity.
- To modify NiO nanoflakes on the microgrooves to acquire a NiO-FAS-17 microgroove hierarchical structure with good hydrophobicity.
- To test the enhancement of the Cu_2O -STA microgroove surfaces on the corrosion resistance properties to reveal the effect of micro/nano-structures.
- To investigate the self-cleaning effect of the NiO-FAS-17 microgroove surface through testing the water droplet bouncing behaviors to reveal the effect of micro/nano-structures.

1.3 Organization of the thesis

The thesis contains 7 chapters in total. Chapter 1 identifies the research gap and provides the research objectives. Chapter 2 presents a systematic literature review. Chapter 3 presents an overall view of the methodologies used in this study. Chapter 4, 5 and 6 are about the main research outcomes and related discussions. Chapter 7 presents the overall conclusions to the thesis and suggests the directions for possible future work.

Chapter 2 Literature review

2.1 Introduction to superhydrophobicity

Hydrophobicity together with hydrophilicity is a common term to describe the wettability of solid surfaces, which is among the most important surface properties (Gao & Li, 2010). It is a key role in many practical applications in daily life, industry, and agriculture (D. Ahmad, van den Boogaert, Miller, Presswell, & Jouhara, 2018; E. Y. Bormashenko, 2018; Erbil, 2020). Superhydrophobic surfaces are provoking much interest as they perform good wetting properties and could bring great convenience (Ma & Hill, 2006). Water contact angle (CA) is a term to characterize wettability defined as the angle where the tangent of water-air interface intersects the solid surface. A 90° CA is the threshold to determine whether the surface is hydrophobic or hydrophilic. Surfaces with larger contact angles than 90° is defined as hydrophobic (T. Zhao & Jiang, 2018). When water contacts a hydrophilic surface, it tends to spread and wet a large area and is likely to penetrate the pores and cracks of the solid surface. On a hydrophobic surface, water is repelled and tends to form a spherical shape. When the contact angle is further enlarged and exceeds 150° , the surface is defined as superhydrophobic (S. Wang & Jiang, 2007). Superhydrophobic surfaces could be categorized into two types according to surface adhesion. One type of SHPO surfaces exhibit little adhesion to water, on which water droplets roll easily, while the other type presents relatively strong adhesion (M. Liu, Zheng, Zhai, & Jiang, 2010; Zeqing Wang, Cong, & Zhang, 2016; W. Zhao, Wang, & Xue, 2010).

Superhydrophobic surfaces were originally discovered from the lotus leaf (W. Barthlott & Neinhuis, 1997) and the leaves of some other plants (Bhushan &

Jung, 2006). The pertinent phenomenon, *i.e.*, the lotus effect, refers to self-cleaning properties resulting from superhydrophobicity exhibited by the lotus leaves. Water keeps its shape as a droplet on the lotus leaf and easily rolls off when the leaf is inclined, simultaneously picking up the dirt particles. Such properties are also found in some other plants leaves (Kurokawa et al., 2018) and wings of certain insects (M. Sun et al., 2014; Y. Sun & Guo, 2019).

In the 1970s, the introduction of scanning electron microscopy (SEM) revealed the microstructure of the surface of the lotus leaf and provided the explanation to this phenomenon. Figure 2.1 shows photographs of a lotus leaf and its nanoscale surface observed under an SEM. On the leaf surface there exists micropapillae array with nanodots on a single papilla as the secondary structure. The papillae are several micrometers in height and covered with dense wax coating (Hans J. Ensikat, Petra Ditsche-Kuru, Christoph Neinhuis, & Wilhelm Barthlott, 2011). The roughness caused by the micrometer-scale papillae and the epicuticular wax result in a minimized adhesion of the water to the leaf surface and this is believed to be the base of the water repellency (Baker, 1982; Wilhelm Barthlott & Ehler, 1977; Forbes, 2008; Jeffree, 1986). The surface tension causes a droplet to preserve a nearly spherical shape instead of wetting of the surface (BAEYER, 2000). Many investigations concerning the lotus leaf (Hans J Ensikat, Petra Ditsche-Kuru, Christoph Neinhuis, & Wilhelm Barthlott, 2011; Sanjay S Lathe, Terashima, Nakata, & Fujishima, 2014; Zhai, Li, Li, Li, & Jiang, 2002) also confirmed the superior properties induced by the micropapilla-nanodot hierarchical structures.

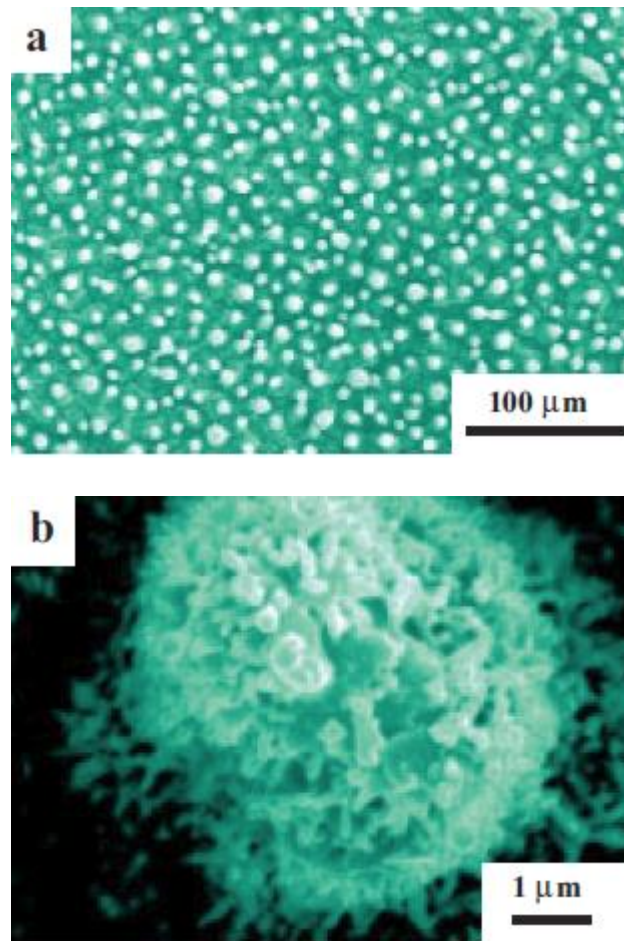


Fig. 2.1 (a) An SEM image of a lotus leaf surface and (b) the zoom-in view of a single papilla.

Anisotropy in wettability is also important and interesting topic of hydrophobic surfaces. Water droplets roll on the surface of some plant leaves in an anisotropic tendency, among which a kind of a rice leaf was studied as an representative (L. Feng et al., 2002). Fig. 2.2 shows the microstructure of the rice leaf surface and the papilla above. While the papillae are distributed in nearly equal distance parallel to the leaf edge (along the arrow in Fig. 2.2), in the perpendicular direction the distribution of the structures is random. The arrangement of the micropapillae defined the anisotropy in terms of the motions of the water droplets.

The sliding angles along the arrow direction and perpendicular to the arrow are different, tested to be around 4° and 12° , respectively. These results offered much information for fabricating solid surfaces with controllable wettability.

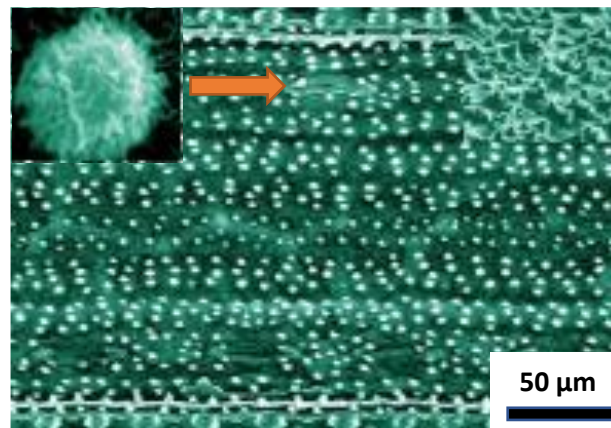


Fig. 2.2 SEM images of a rice leaf with an anisotropic tendency. The inset shows the magnified image of a single papilla. The arrow points out the direction the hydrophobic papillae are distributed.

2.2 Wetting of solid surfaces

2.2.1 Static wetting properties

Hydrophobicity can be first reflected by the contact angle of the surface. The static contact angle refers to a contact angle measured from a static state, which is the mostly used term. A larger contact angle means better hydrophobicity of a surface (Good, 1992; Rothstein, 2010; Strobel & Lyons, 2011).

There has been a lot of theoretical research work on wetting of a solid surface, among which two different classes of superhydrophobic states are exhibited, namely the Wenzel state and Cassie-Baxter state, featured with different

characteristics of the liquid-solid interface (Sanjay Subhash Latthe, Gurav, Maruti, & Vhatkar, 2012; Marmur & Bittoun, 2009; Nosonovsky, 2007). Many of hydrophobic surfaces with micro/nano structures makes it possible to either retain air or water in the interspace and form difference states, especially when the surface is immersed in water, owing to surface tension.

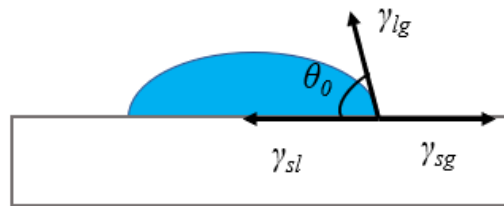


Fig 2.3 Schematic of a liquid drop showing the terms in Young's equation.

The Young's equation is proposed for the contact angle on an ideal surface (perfectly smooth and chemically homogeneous). It is displayed as (Young, 1832)

$$\cos \theta_0 = \frac{\gamma_{sg} - \gamma_{sl}}{\gamma_{lg}}$$

where γ_{sg} , γ_{sl} and γ_{lg} are the interfacial tensions of the solid-vapor, solid-liquid and the liquid-vapor interface, respectively.

For realistic rough surfaces, the wetting mechanism is more complex. The influence of rough surfaces was first proposed by Wenzel, Cassie and Baxter. The Wenzel's model on the contact angle (Wenzel, 1936) describes the condition where liquid completely penetrate the gaps in the rough surface. The Wenzel's contact angle is presented as

$$\cos \theta_w = \frac{r (\gamma_{sg} - \gamma_{sl})}{\gamma_{lg}} = r \cos \theta_0$$

where θ_w is the apparent contact angle. The angle θ_0 is the contact angle on a smooth surface with the same surface chemistry. The ratio r is the surface roughness factor meaning the ratio of the actual contact area to the projected surface area. The Wenzel equation predicts that wetting is lessened by roughness if θ_0 exceeds 90° .

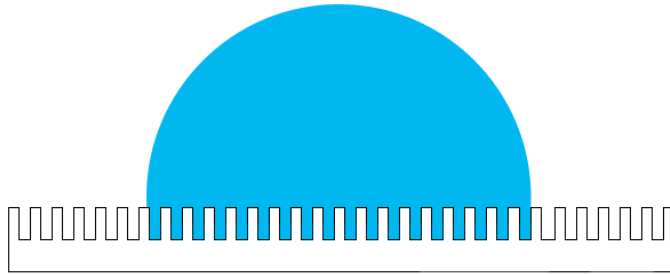


Fig. 2.4 Schematic of Wenzel mode on a rough groove surface as an example.

In some cases, air bubbles may exist in the gaps of the grooves. The liquid droplet is then actually placed on an air-solid composite surface. This wetting condition is proposed as Cassie-Baxter state. The Cassie-Baxter state (Cassie & Baxter, 1944) is a wetting state where the grooves under the droplet are considered to have been filled with vapor instead of the corresponding liquid. The interface between the liquid and the grooves comprises the liquid-solid interface and the liquid-gas interface. The apparent contact angle is the sum of the effect from both phases. It is displayed as

$$\cos \theta_c = f_1 \cos \theta_1 + f_2 \cos \theta_2$$

where θ_c is the apparent contact angle; f_1 and f_2 are the surface fractions of liquid-solid and liquid-gas contact; θ_1 and θ_2 are the contact angle on liquid-solid phase and liquid-gas phase. The contact angle for gas-liquid interface equals 180° , and $f_1 + f_2 = 1$. Consequently, the contact angle can be calculated as

$$\cos \theta_c = f \cos \theta_0 + f - 1$$

It can be concluded from this equation that the extreme case at $f=0$ means the droplet is not in touch with the surface and that at $f=1$ complete wetting occurs.

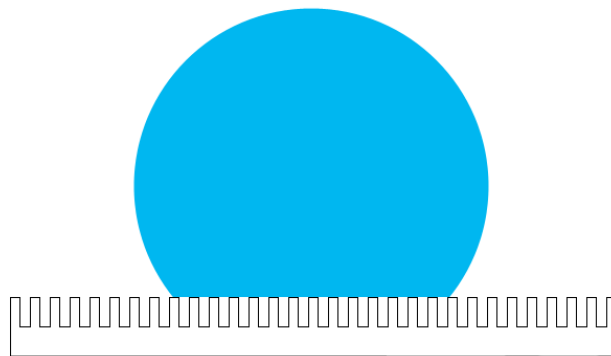


Fig. 2.5 Schematic of Cassie-Baxter mode on a rough groove surface as an example.

In practice, the solid-liquid contact form may change, in most cases, from the Cassie-Baxter to the Wenzel as turbulence like droplet movement, vibration, hydraulic pressure and dissolution would occur (E. Bormashenko, Bormashenko, et al., 2007; E. Bormashenko, Pogreb, Whyman, Bormashenko, & Erlich, 2007; E. Bormashenko, Pogreb, Whyman, & Erlich, 2007; Forsberg, Nikolajeff, & Karlsson, 2011). Besides the state transitions, coexistence could also appear on a

nanopillared surface (Koishi, Yasuoka, Fujikawa, Ebisuzaki, & Zeng, 2009). Factors including pillar height and initial conditions of droplets were found to influence the formation of Wenzel/Cassie-Baxter state. Indeed, both the two equations require consideration on an ideally designed and robust SHPO substrate for precise prediction (Patankar, 2003).

Some discussions are stated in this section based on previous experiments and analysis of the theoretical relationships. In early times of research on surface wettability, a number of fractal surfaces are compared and measured to validate theoretical predictions (Onda, Shibuichi, Satoh, & Tsujii, 1996). A rough substrate with given values of roughness factor r and fraction ratio f was prepared and investigated, presenting results showing an intuitive plot of the apparent contact angle correlated with the equilibrium contact angle according to Wenzel's and Cassie's equation, as shown in Fig. 2.6 (Bico, Marzolin, & Quéré, 1999).

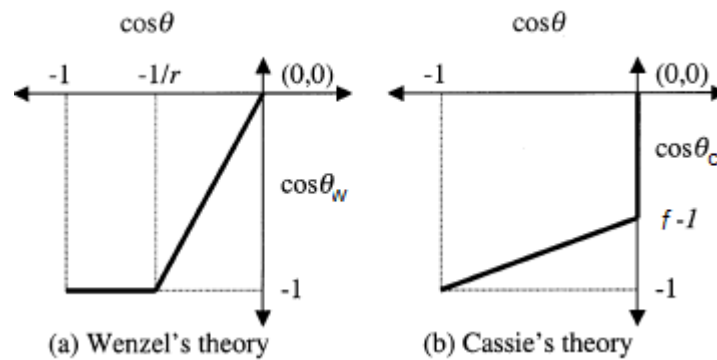


Fig. 2.6 The apparent contact angle versus equilibrium contact angle derived from the Wenzel mode and the Cassie-Baxter mode

The change of apparent contact angles were also recorded in an experiment where a drop is pressed physically and changed its shape (Bico et al., 1999). The apparent contact angle originally in agreement with following Cassie's theory changed from 170° to 130° , which was found to follow the Wenzel's mode. This indicates that the applicability of Wenzel's or Cassie's theory depends a lot on practical conditions. Therefore, Cassie's or Wenzel's equation cannot be simply assumed as the standard when designing a SHPO substrate, as the transition and coexistence may occur.

2.2.2 Dynamic wetting properties

The static contact angle alone is sometimes insufficient to reflect the wettability of a surface, as it cannot assess the mobility of the fluid on surface, or in other words the adhesion to water (Barber, Cohen, & Wagner, 2004; Eral, 't Mannetje, & Oh, 2013). The sliding angle and contact angle hysteresis are two important and classic elements to measure the mobility of a drop on the surface. They are associated with possible applications in such fields as drag reduction and self-cleaning (Jeevahan, Chandrasekaran, Joseph, Durairaj, & Mageshwaran, 2018). The droplet will start to roll as the surface it lands on is inclined. When the droplet comes to this critical state, the sliding angle is equal to the inclined angle of the surface versus the horizontal plane. Contact angle hysteresis (CAH) is the difference between the advancing contact angle and receding contact angle (Changwei, Hao, & He, 2009; Eral et al., 2013). The value of the sliding angle is positively correlated with CAH, which was first proposed in the 1960s (Furmidge, 1962). A large sliding angle or CAH means strong adhesion to the water droplet.

A droplet will rest on a surface with large CAH even though it is inclined to a large angle. The droplet deforms and tends to move downwards, while CAH tends to keep it in place.

On a smooth surface, the sliding angle α satisfies the following equation (Furmidge, 1962):

$$\rho g V \sin \alpha = 2 R k$$

where ρ and V are the density and volume of the droplet, g means the gravity acceleration, R is the radius of the area where the surface is in contact with the liquid and k is a constant. According to Frenkel's research (Frenkel, 2005), the constant k can be expressed as

$$k = \gamma_{LV}(1 + \cos \theta_0)$$

using the static contact angle in θ_0 Young's equation. Verified by Furmidge, there is a relationship where k can be replaced by the advancing contact angle θ_a and the receding contact angle θ_r

$$\rho g V \sin \alpha = 2 R \gamma_{LV}(\cos \theta_r - \cos \theta_a)$$

producing another expression for the constant k

$$k = \gamma_{LV}(\cos \theta_r - \cos \theta_a)$$

To promote the model to sliding conditions on rough surfaces, the wetted radius R and the constant k should be substituted (Lv, Yang, Hao, He, & Zheng, 2010). The radius R' is expressed with V and the apparent static contact angle θ (Yi, Liu, Wu, & Li, 2019):

$$R' = \left[\frac{3V}{\pi(2 - 3 \cos \theta + \cos^3 \theta)} \right]^{\frac{1}{3}} \sin \theta$$

The square root of solid area fraction f is introduced as a modifier of the constant k and the expression of the sliding angle was yielded as

$$\rho g V \sin \alpha = 2R' \gamma_{LV} (1 + \cos \theta_0) \sqrt{f}$$

This relationship is specially for the rough surfaces whose contact state is the Cassie-Baxter mode. However, the solid area fraction under a specific water droplet is sometimes difficult to determine, which limits the application of these equations.

2.3 Artificial superhydrophobic surfaces with micro/nano-structures

Superhydrophobic surfaces in the nature have shown that surface wettability is governed by both the surface chemistry and geometry (Ball, 1999; L. Feng et al., 2002; Jiang et al., 2000; Koch, Bhushan, & Barthlott, 2009; Koch, Bhushan, Jung, & Barthlott, 2009; Y. Y. Yan, Gao, & Barthlott, 2011). To mimic the structure, there are a variety of fabrication methods available that could be grouped into top-down approaches and bottom-up approaches (Jeevahan et al., 2018). With these methods rough surfaces could be fabricated, coated with materials of low surface energy, in which way superhydrophobic surfaces can be produced. This section will review the artificial superhydrophobic surfaces fabricated by these methods.

The top-down technique refers to fabrication routes of structures through material removal process. The main techniques include lithography (Dong et al., 2019), micromachining (Ding, Cao, Wang, Xu, & Wang, 2019), plasma treatment (Ryu et al., 2017), laser texturing (Ta et al., 2015) and chemical etching (X. Zhang

et al., 2019). The bottom-up approach is identified as structure build-up with material addition and mainly comprises chemical vapor deposition (CVD) (F. Zhang et al., 2017), electrochemical deposition (Zhou, Zhu, & Yan, 2018) and sol-gel method (M. Yang et al., 2018). Top-down methods generally produce structures possessing air fraction in microscale while bottom-up methods can form complex surfaces by add building blocks of materials for micro/nano fabrication. Hence, bottom-up approaches are much more suitable for fabricating surfaces with small gaps as air fraction rather than top-down approaches (Hosono, Fujihara, Honma, & Zhou, 2005).

The strategies researchers applied to mimic the SHPO materials in nature and make efforts to fabricate artificial SHPO surfaces can be categorized conventionally in two. One is to fabricate rough architecture on a hydrophobic surface. The other is to prepare a modification layer with low surface energy on a smooth surface (J. Feng, Wang, & Zhao, 2009). Up to now, top-down approaches, bottom-up approaches or a combination of the two types have been developed for structured surfaces, while the top-down methods mainly produce regularly patterned surfaces and the bottom-up approaches mainly yield randomly structured surfaces (Z. Ahmad, Rehman, & Ahsan, 2009; L. Feng et al., 2002; Jeevahan et al., 2018; Y. Y. Yan et al., 2011; Xi Zhang, Shi, Niu, Jiang, & Wang, 2008). Specific techniques to prepare superhydrophobic surfaces are quite varied with different complexity and cost. The related research work and their advantages and limitations will be stated in this section.

2.3.1 Top-down approaches

Lithography is a commonly used method that is fit for fabrication of regularly patterned surface structures. It is a sophisticated technique with abundant sub-techniques including photolithography (M.-H. Chen, Hsu, Chuang, & Tseng, 2009; Kwon, Patankar, Choi, & Lee, 2009; C. J. Long, Schumacher, & Brennan, 2009), soft lithography (Yong Chae Jung & Bhushan, 2009; J. Ou, Moss, & Rothstein, 2007; Reyssat & Quéré, 2009), nanoimprint lithography (Y.-W. Choi, Han, Lee, & Sohn, 2009) and colloidal lithography (Xuemin Zhang et al., 2009). For microfabrication or nanofabrication discussed in this thesis, it specially refers to photolithography. Photolithography is a process for microfabrication that transfers a geometric pattern from a photomask to a photoresist on a thin film or the bulk as the substrate. Followed by a series of chemical treatment, the transferred surface pattern will be acquired.

Byun *et al.* (Byun, Kim, Ko, & Park, 2008) fabricated a microchannel with microgrooved walls made of polydimethylsiloxane (PDMS) using a standard soft lithography process, as shown in Fig. 2.7. The width and pitch of the grooved walls could be tuned and finally reached a contact angle of 145° . The microchannel is beneficial for the slippage effect and visualization of the near-wall flow. The slip length could be directly measured on hydrophobic microchannel with approximately $2\ \mu\text{m}$ in comparison with a hydrophilic glass wall microchannel presenting a no-slip boundary.

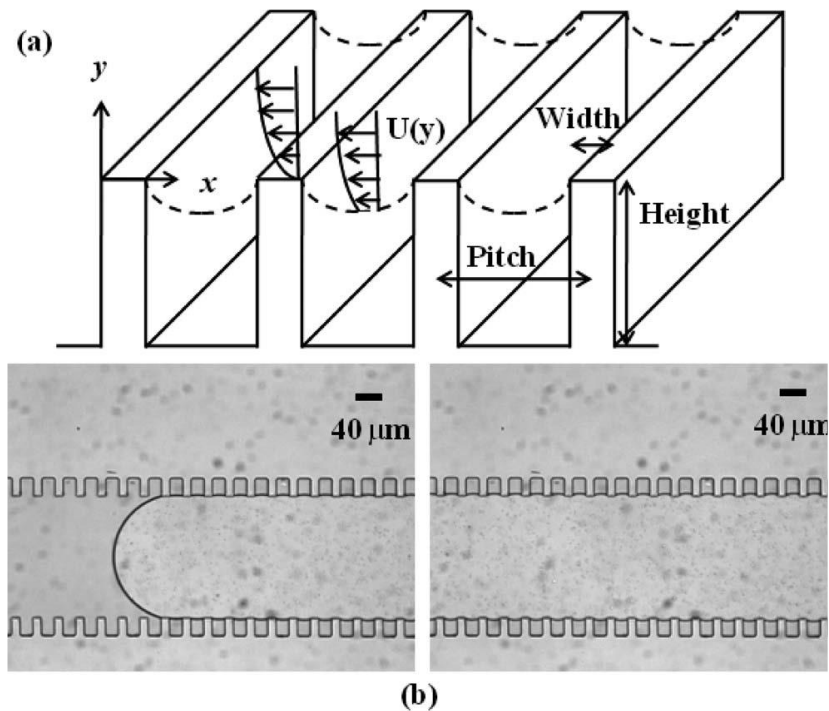


Fig. 2.7 (a) Schematic of the microscale grooves and the velocity field. (b) Flow in the microchannel with grooved walls.

A film or a bulk could be selectively eroded in specially prepared etching medium. This process can also be assisted with plasma or laser. Kashaninejad *et al.* (Kashaninejad, Nguyen, & Chan, 2012) used a typical DRIE method to produce microholes on PDMS and applied it as the bottom wall of a microchannel, as in Fig. 2.8. The microhole surface could present a contact angle as 141° . The effects on the slip length and flow velocity in the microchannel was experimentally investigated. Good hydrophobic drag reduction effect was revealed with a maximum increase in the relative velocity of 39%.

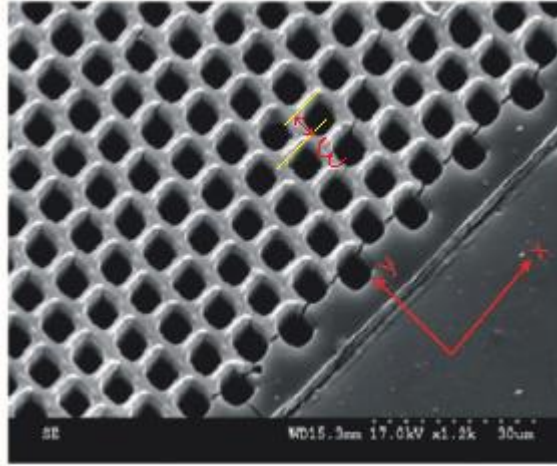


Fig 2.8 SEM images of the PDMS microhole surface. This picture is reprinted from Kashaninejad, Nguyen, & Chan, 2012.

Femtosecond laser micromachining provides such a process that can be applied to widely used engineering materials. It is a comparatively fast and simple process (Ahmmed, Grambow, & Kietzig, 2014; J. Cheng et al., 2013; Faisal, Zindani, Kumar, & Bhowmik, 2019). Wu *et al.* (B. Wu et al., 2009) created patterned stainless steel using femtosecond laser machining and acquired hydrophobicity by subsequent salinization. Kietzig et al. (Kietzig, Negar Mirvakili, Kamal, Englezos, & Hatzikiriakos, 2011) extended this method beyond iron-based materials to include different and pure metallic substrate. Long *et al.* (J. Long, Zhong, Fan, Gong, & Zhang, 2015; J. Long, Zhong, Zhang, & Fan, 2015) proposed picosecond laser processing on aluminum and copper and investigated the wettability conversion of the fabricated surfaces. Infrared nanosecond fiber laser processing (Ta et al., 2015) was also utilized to acquire superhydrophobic metallic surfaces, which provided a robust operating system, increases the processing rate and lowered the cost. Gregorcic *et al.* (Gregorčič, Šetina-Batič, & Hočevar, 2017; Može, Zupančič, Hočevar, Golobič, & Gregorčič, 2019) further investigated into

the laser processing technique for superhydrophobic metallic surfaces fabrication. As shown in Fig. 2.9, samples with different morphology were fabricated and the wettability depending on laser fluence was studied. The laser textured metallic surface were also promoted into applications of corrosion resistance (Emelyanenko et al., 2018; Trdan, Hočevvar, & Gregorčič, 2017).

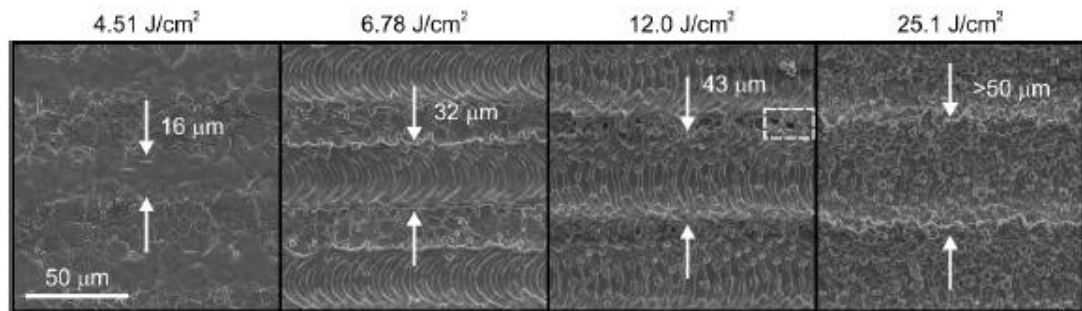


Fig 2.9 SEM images of typical microchannels fabricated by laser texturing under different energy density. Picture reprinted from reference Gregorčič, Šetina-Batič, & Hočevvar, 2017.

2.3.2 Bottom-up approaches

There are various facile bottom-up techniques that are suitable for fabrication randomly structured surfaces, among which are mostly nanostructured surfaces. These methods including etching, electrochemical deposition, electrospraying, hydrothermal synthesis and self-assembly could also be used following methods like lithography and micromachining to produce secondary structures and result in a synergistic effect. In this section, a number of typical products are presented to show the artificial superhydrophobic surfaces.

A typical wet chemical method applied for fabricating superamphiphobic surfaces upon some engineering metals and alloys is shown in Fig. 2.10 (Meng,

Wang, Xi, Tang, & Jiang, 2008). This is via a chemical reaction in perfluorocarboxylic acid solutions, where the process time and reagent concentration could be tuned to control the morphology of the etched layer. The reaction yields surface chemistry composition with low surface energy and rough structures. Fig. 2.10 displays the nanosheets completely spreading on zinc substrates, which presents good water and oil repellency as shown in the camera pictures.

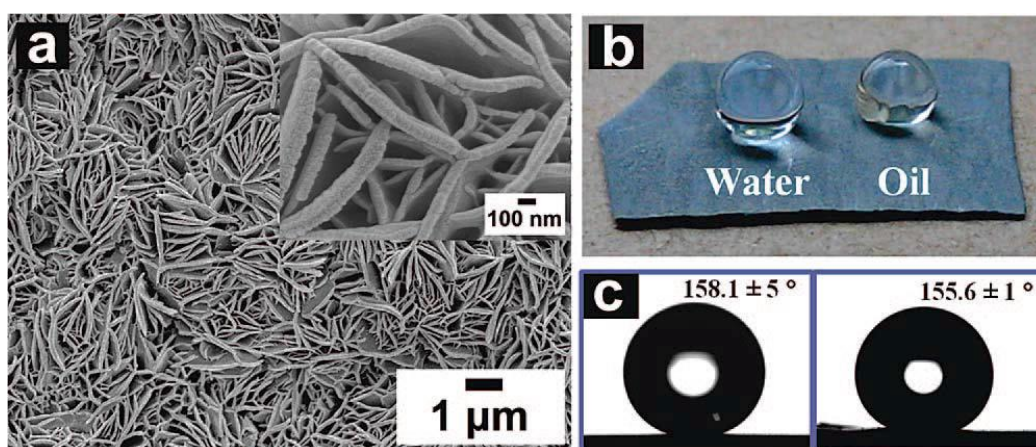


Fig. 2.10 (a) SEM images of the prepared petal-like zinc surface in a large area. (b) The picture of water and oil droplets on the superhydrophobic surface. (c) Contact angles of water (left) and oil (right) droplets. Reprinted from reference Meng, Wang, Xi, Tang, & Jiang, 2008.

Electrospraying (Burkarter et al., 2007) was employed to deposit superhydrophobic polytetrafluoroethylene (PTFE) films on FTO glass. Good water repellency was displayed with contact angle of 160° and the sliding angle nearly 2° . The properties were due to the nanostructured PTFE coating shown in

Fig 2.11. The coating was featured with microspheres with nanoscaled bulges, providing roughness for the superhydrophobic surfaces.

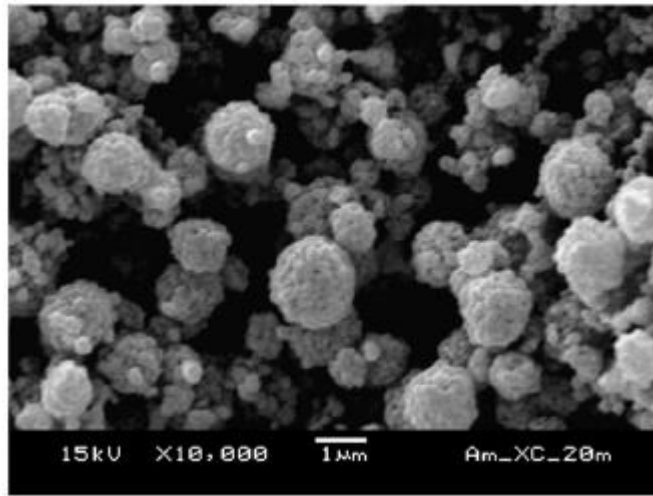


Fig. 2.11 An SEM image of PTFE microspheres prepared by electrospinning. Reprinted from Burkarter *et al.*, 2007.

The micro/nanostructures could also be prepared through an *in-situ* hydrothermal method. 3D iron oxide micro/nanoflakes (Song, Shen, Ji, & Jing, 2010) were constructed on an iron plate surface after heated in potassium carbonate solutions. The process was then followed with vinyltriethoxysilane treatment. This is also a typical route for fabrication of metal oxide based hydrophobic coatings. The resultant surface fully covered by the micro/nanoflakes was able to present superhydrophobicity.

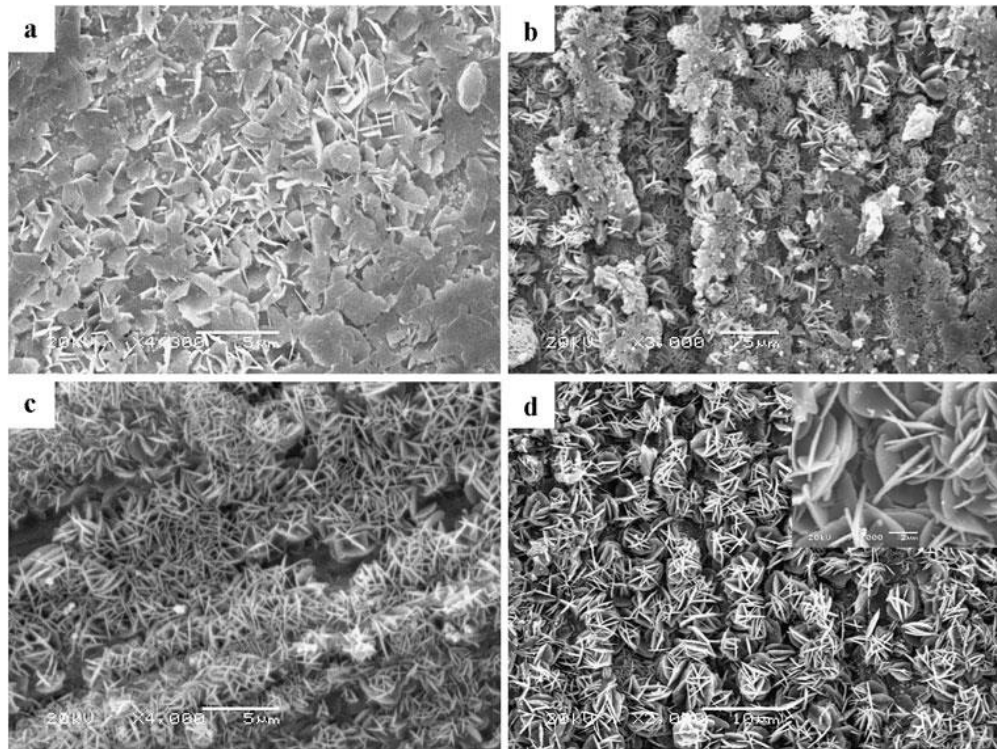


Fig 2.12 SEM images of oxide crystals prepared under different hydrothermal bath concentrations and heating temperatures. Reprinted from Song *et al.*, 2010.

The techniques are not necessarily independent. In many cases researchers performed a combination to acquire an SHPO surface. For example, photolithography can be followed by plasma etching to acquire complex roughness on multiple layers on a surface (del Barrio & Sánchez-Somolinos, 2019; Petlin, Tverdokhlebov, & Anissimov, 2017). Jung *et al.* (Y. C. Jung & Bhushan, 2010) developed biomimetics materials based on microposts by soft lithography as shown in Fig. 2.13. Then lotus wax was disposed and formed a film by self-assembly as the second step to prepare a hierarchical structure. In their work, surfaces with flat, nano, micro, and hierarchical structures were assembled as walls

of a channel and the pressure drop was measured to figure out the drag reduction efficiency.

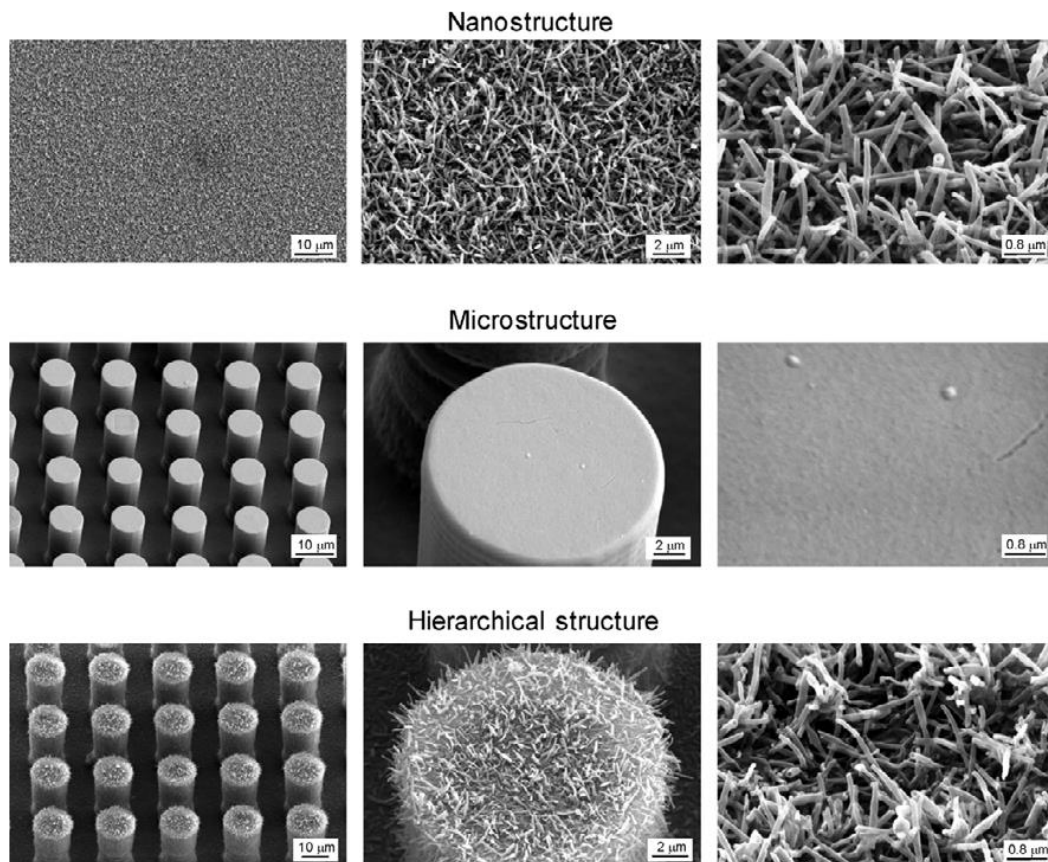


Fig 2.13 SEM images under three magnifications presenting nanostructures on flat, micropillars and silicon-lotus wax hierarchal structures. Reprinted from Jung & Bhusan, 2010.

Combination of different techniques is not limited to fabrication of hierarchical structures. To produce some specific regular patterned structures, researchers also applied multiple techniques on a single product. Choi *et al.* (C.-H. Choi, Ulmanella, Kim, Ho, & Kim, 2006) fabricated well-defined nanogrates with a very high aspect ratio by interference lithography followed by deep reactive ion etching on a silicon base. In this way they acquired a robust hydrophobic surface

over a large area as displayed in Fig. 2.14. Their work was ever the first to utilize nanoscale regular patterns to measure the interaction with liquid flows.

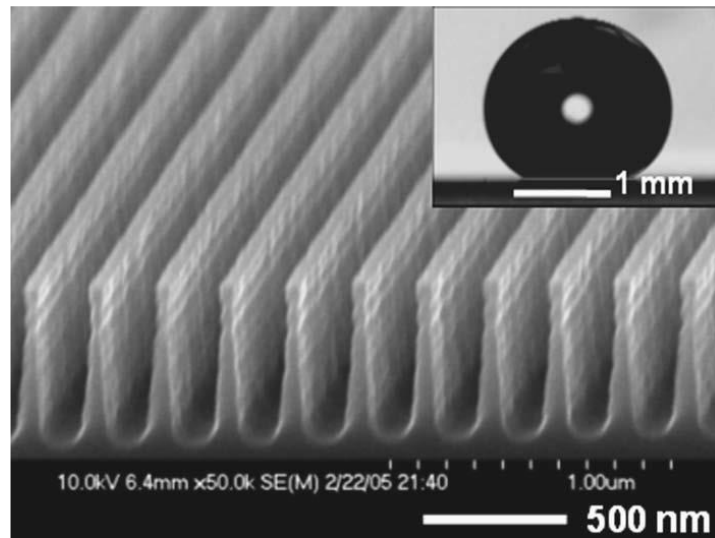


Fig. 2.14 The SEM image of a silicon nanogratings with approximately 230 nm pitch and 500 nm depth. The inset shows the apparent contact angle of water about 150° . Reprinted from reference C.-H. Choi, *et al.*, 2006.

2.3.3 Ultraprecision machining

Among the varied top-down methods, ultraprecision machining is an efficient and feasible way to fabricate high quality surfaces. The products could reach the standard in form accuracy of sub-micrometer and surface roughness up of nanometer (Brinksmeier, Gläbe, & Schönemann, 2012; Duo Li, Wang, Tong, Blunt, & Jiang, 2019; Zhiyu Zhang, Yan, & Kuriyagawa, 2019). The definition of ultraprecision keeps updating with the continuous progress in sciences and

technologies. It covers the indexes of profile and roughness and difficulties for specially-targeted surfaces under certain technical circumstances.

Current ultraprecision machining technologies can be categorized in four fields, namely ultraprecision cutting, ultraprecision grinding, ultraprecision polishing and ultraprecision non-traditional machining. Ultraprecision cutting is the technology using tools made of diamonds and sometimes other hard materials. It comprises branches including turning, milling, boring and compound machining (J. Yuan, Lyu, Hang, & Deng, 2017). It is mostly used to fabricate micropatterned surfaces for a variety of applications requiring components with stringent requirement in accuracy and surface integrity. The pursuits of this technology include improving the product surface quality, improving reliability and stability of machining process, promoting miniaturization, and improving interchangeability of components. With the development of automobiles, energy technology, medical instrument, optical engineering and some other industry areas, there is a growing need for equipment and components produced by ultraprecision machining (Schneider, Das, Kirsch, Linke, & Aurich, 2019; Takino, Kanaoka, & Nomura, 2011; SJ Zhang, To, Wang, & Zhu, 2015; Shaojian Zhang, Zhou, Zhang, Xiong, & To, 2019). Key techniques of ultraprecision machining including single-point diamond cutting (SPDT), fly cutting and five-axis milling have been developed to fulfill the growing need (Brinksmeier et al., 2010; G. Chen, Liang, Sun, Chen, & Wang, 2013; Hatefi & Abou-El-Hossein, 2020; SJ Zhang, To, Zhu, & Zhang, 2016).

Ultraprecision machining is applied to achieve nano-level surface roughness on planar surfaces, aspherical surfaces and complex curved surfaces on many kinds of materials including copper, acrylic, ceramics and other compound

materials. Besides, it is also utilized for microstructure cutting. Compared with MEMS technique, laser-texturing, and some other micromachining technologies, UPM possesses the advantages in yielding 3D structures, machining flexibility, efficiency, and cost. It is especially effective in fabricating microstructures under 100 μm with relatively high depth-width ratio. Meanwhile processing of a material at its lowest scale ensures good surface finish of the structures. In a UPM process, a diamond tool could incorporate up to five controlled axes and thus provides more degrees of freedom. This makes it easier and more flexible to fabricate complicated structures than other mechanical and chemical processes (Davies, Evans, Vohra, Bergner, & Patterson, 2003; S. Zhang et al., 2019). There are some typical structures such as micropyramids (Ge et al., 2018), microgrooves (C. T. Cheng, Zhang, & To, 2016), freeform compound-eye microlens array (Lei Li & Allen, 2012) and rotational microridges (Likai Li & Allen, 2011), which are utilized in fields including optics and energy.

Superhydrophobic surfaces fabricated with the aid of ultraprecision machining have not been studied a lot. Such investigations are essential as the wettability of the UPM fabricated components are critical in some areas. The precise control of the geometry of the UPM fabricated patterns is also beneficial for the study into the mechanism of wetting behaviors. Microstructured surfaces with sinusoidal grids (Lu, Lee, Lee, & Park, 2012) were fabricated by fast tool servo diamond turning as in Fig. 2.15. By tuning the fabrication parameters (spindle speed, feed rates), slightly different geometries of the sinusoid grids could be acquired. The best hydrophobic grid surface can reach a static contact angle of 120.5°.

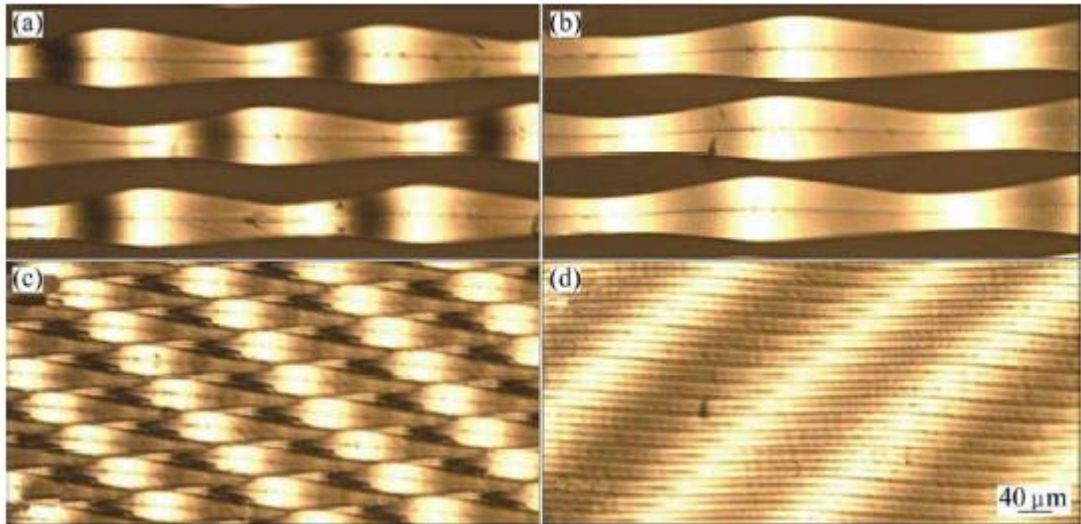


Fig. 2.15 Sinusoidal grid microstructures viewed under an optical microscope fabricated at different spindle speed and feed rate

Cheng *et al.* (C. T. Cheng et al., 2016) designed and fabricated microgroove and micropillar surfaces on cyclic olefin copolymer (COC) by ultraprecision raster milling to study the wetting properties. The shape boundaries have helped the definition of the area fraction of the wet area of the patterned surface, which was related to the formation of the contact angle. The developed fabrication routes can provide potential for mass production of patterned surfaces with a contact angle over 140° .

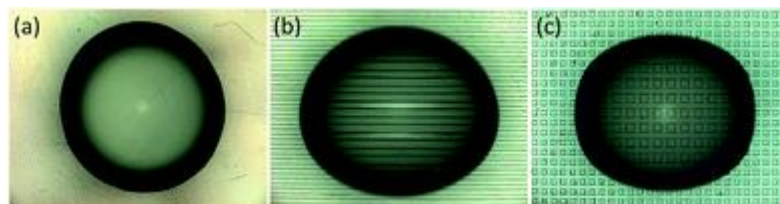


Fig. 2.16 Top view of a water drop on the (a) flat, (b) microgroove and (c) micropillar COC surface.

2.3.4 Hydrothermal synthesis

Hydrothermal synthesis is a chemical reaction in water driven by high temperature and pressure. The process is performed by heating hydrothermal bath in a sealed pressure vessel. It is a major synthetic method for inorganic micro/nanostructures, after which simple chemical treatment is supplemented to gain hydrophobicity. It is a facile and popular route as a low-temperature solution-based chemical strategy. Other advantages of hydrothermal synthesis include convenient manipulation, high yield, and control over product morphology.

The product of hydrothermal method relies on the chemical reactions in precursor solution in the sealed reaction vessel. As for fabrication of micro/nano structured surfaces, substrate is needed in a hydrothermal process. In the growth process, a crystalline film grows on a substrate of a different material, which is well-cleaned in advance and placed in the vessel with the precursor. After the reaction, the product with structured crystals could be found to have grown on the substrate (Shi, Song, & Zhang, 2013). Metal oxide or hydroxide is the representative products of the process, which is acquired through hydrolysis of the corresponding metal salt. Researchers have prepared varied products including but not limited to TiO₂, ZnO, Co₃O₄, and CuO micro/nano structures presenting different morphology on various substrates (glass, pure metal, ceramics, fabrics *et al.*) utilized mainly in application fields of energy, optics and sensors (Gerbreders et al., 2020; S. Huang, Yu, Wang, & Li, 2018; Z. Huang et al., 2021; Liang, Qiao, Cui, & Hou, 2019; Shen, Xu, Lin, & Pan, 2017; Y.-Y. Sun, Zong, Li, & Wei, 2018). There are also a lot of research reporting hydrothermally prepared superhydrophobic surfaces and its related applications. Varied materials were prepared and investigated for hydrophobicity, covering applications such as self-

cleaning, corrosion resistance, anti-icing and anti-bacterial (Chu, Sun, Tong, & Jiang, 2021; He et al., 2021; Jeong, Bolortuya, Eadi, & Kim, 2020; Lan, Zhang, Wang, Fan, & Zhang, 2021).

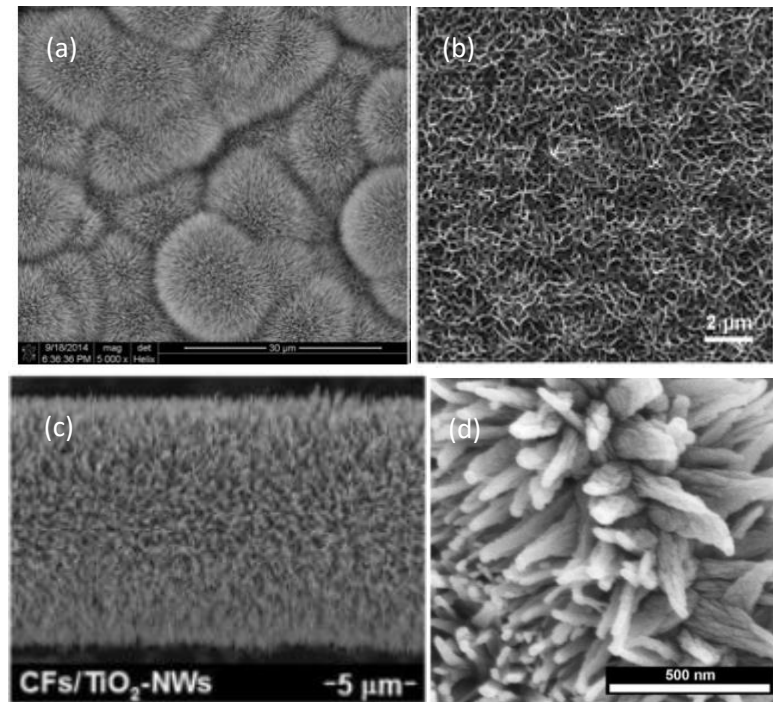


Fig. 2.17 Typical hydrothermally prepared metal oxide nanostructures (a) Co_3O_4 (b) ZnO (c) TiO_2 and (d) CuO

Hydrothermal synthesis of metal oxide could be performed on UPM-fabricated metal micropatterns. This indicates that combination of the two methods is facile for fabrication of hierarchical surfaces for potential hydrophobic applications. As UPM could be performed on most nonferrous metals and hydrothermally prepared nanomaterials could be prepared on most metal substrate with proper pretreatment, such hierarchical surface could be prepared on various metal or alloy substrate. In this research only copper substrate is selected for investigation in exploring novel fabrication routes for ultimate hydrophobic properties and the mechanism in certain hydrophobic applications. This could be

promoted to other types of substrates such aluminum and magnesium that require superhydrophobic coatings.

2.4 Hydrophobic self-cleaning

Self-cleaning is one of the most attractive topics because it is an ability to maintain a clean surface without any external aid (Sanjay S. Latthe et al., 2019; Sethi & Manik, 2018). Superhydrophobic and superhydrophilic surfaces can both have self-cleaning effect based on different mechanisms. Water droplets will spread on a superhydrophilic surface, enlarge the contact with dirt and debris and wash them away from the surface. Unlike superhydrophilic surfaces, SHPO surfaces are repellent to water. The basic principle is the formation of a spherical water droplet that collects dirt on the surface, as is the inherent ability of the lotus leaf (Dalawai et al., 2020).

The goal in developing superhydrophobic self-cleaning surfaces is to make the water repellent property reappear on an artificial surface. This is reflected in a large static contact angle and a small contact angle hysteresis. The sliding properties, or in other words, the dynamic wetting properties is critical as self-cleaning surfaces need to allow for water on the surface to easily flow away. Water droplet bouncing is also presented in this section as another method to characterize the self-cleaning effect. It is a powerful addition to describe wettability of surfaces with very good water repellency, as dynamic contact angles are sometimes difficult to measure and not applicable to distinguish the hydrophobicity of multiple surfaces.

2.4.1 Development of surfaces with self-cleaning effect

The development of a superhydrophobic material is critical to gain self-cleaning effect on a surface. In many cases, coatings are used to protect patterned surfaces and provide hydrophobicity. Such coatings possess advantages including low fabrication and maintenance cost, good durability, additional properties including prevention of ice, corrosion, or pollution. These coatings could potentially be used in areas of textiles, garments, automotive, building, etc.

To modify low surface energy materials on metallic materials, formation of metal oxides is a commonly used method. It can be followed with spontaneous adsorption of organic molecules to achieve a hydrophobic surface. As the surrounding environment is always fixed in practical cases, the decrease of surface tension of the surface material is essential. The surface energies of some commonly used chemical groups are known as $\text{CH}_2 > \text{CH}_3 > \text{CF}_2 > \text{CH}_2\text{F} > \text{CF}_3$. A smooth surface attached with $-\text{CF}_3$ chemical group could reach a largest static contact angle of about 120°C (Vazirinasab, Jafari, & Momen, 2018). When adsorbed on rough surfaces, the contact angles would be further increase and would be a chance that superhydrophobicity is achieved. Immobilization of fluoromethyl groups is always through the self-assembly of fluoroalkyl-silane. Reaction with water transforms the siloxane groups into silanol groups, which forms covalently bound silanes on the metal oxide surface in the dehydration condensation process. Meanwhile, dehydration take place among the silanol groups and leads to the formation of polysiloxanes. Therefore, the fluoromethyl protuberances present good coverage on the oxide surface and result in hydrophobicity (Kang et al., 2012). Immobilization of alky groups is performed also by spontaneous reactions of fatty acids with metal oxides. Corresponding salts

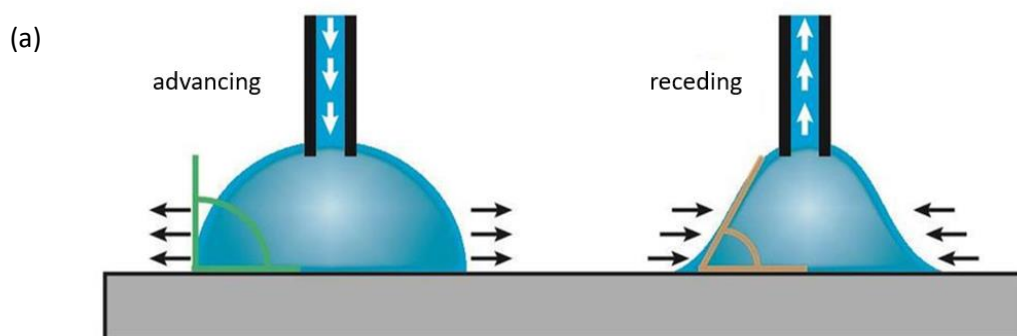
are produced and bond the alkyl groups with the oxides. The long chain alkyl groups make up the protuberances and act hydrophobic (Wan et al., 2018).

Associated with the two most common used low surface energy organics, stearic acid and 1H, 1H, 2H, 2H-perfluorodecyltriethoxysilane (FAS-17), different metal oxides including Al₂O₃ (Prado, Sriyai, Ghislandi, Barros-Timmons, & Schulte, 2010), Fe₃O₄ (J. Hu et al., 2019), NiO (Z. Q. Yuan, Hao, Bin, Wang, & Chen, 2012), ZnO (Y. Cheng et al., 2017) and CuO (Xiao et al., 2015) were prepared to fabricate superhydrophobic coating. For corrosion resistance on copper materials, the hydrophobic coatings are usually based on cupric oxide or cuprous oxide. Liu et al. (T. Liu et al., 2007) prepared myristic acid chemically adsorbed onto the copper wafer for superhydrophobic corrosion resistance. A flower-like nanostructure was formed on the copper surface and induced good water-repellent property. Kong et al. (Kong, Chen, Yang, Yu, & Zhang, 2008) prepared slice-like structure by building Cu₂(OH)₃NO₃ crystal via a facile solution-immersion method. The sample was able to retain hydrophobicity at elevated temperature and thus broadened the use as engineering materials. Similar to Liu's work, Chen et al. (Y. Chen et al., 2009) applied one-step solution immersion method with another fatty acid to prepare superhydrophobic film directly on copper. She et al. (She et al., 2012) applied CuO-lauric acid superhydrophobic coating on magnesium alloy. Transitional layers were deposited to enhance the attachment between CuO and the magnesium alloy substrate. Micro/nanostructures can be acquired either by direct reaction between fluoroalkylsilane or fatty acid, always assisted with heating or DC voltage (Su & Yao, 2014), or by formation of metal oxide crystal and subsequent self-assembly of the fatty acid or fluoroalkylsilane (P. Li, Chen, Yang, Yu, & Zhang, 2014). This

can be either achieved by hydrothermal synthesis (Wan et al., 2018) or anodization process (P. Li et al., 2014; Xiao et al., 2015).

2.4.2 Measurements of contact angles

There are three types of methods to experimentally determine the key property of dynamic wetting behaviors, the contact angle hysteresis (CAH) (Eral et al., 2013; Montes Ruiz-Cabello, Rodríguez-Valverde, Marmur, & Cabrerizo-Vílchez, 2011; Strobel & Lyons, 2011). The first one is the tilted plate method where curvatures of the droplet are measured on a rotating plane. The dynamic contact angles are measured when the droplet starts sliding (Tadmor et al., 2009). The second method is the sessile drop method. Water is pumped into and out of a needle forming droplets with changing volume compressed onto the sample surface. The advancing and receding contact angles can be acquired in this process. The third method is the Wilhelmy method. The sample surface is inserted into or pulled out of a water bath under a controlled speed. No moving droplets are utilized in this process (Volpe & Siboni, 2018).



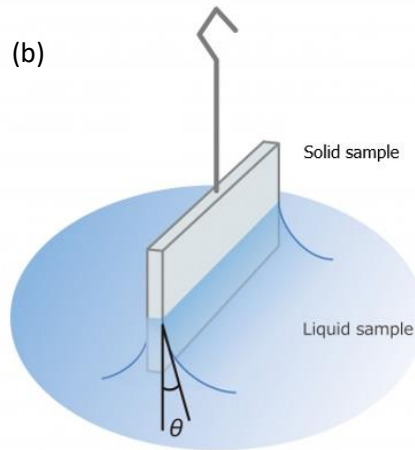


Fig. 2.18 Schematic diagram of (a) the sessile drop method and (b) the Wilhelmy method for dynamic angles measurement

The equipment required for the three methods are not complicated, where a camera, a needle and a pump or a motor and a force sensor would be quite enough. There are shortcomings that limit the measurement conditions for the methods. In the tilted plate method, the droplet needs to move at a finite velocity so that the camera could capture the droplet movement properly. A more critical drawback is that the pressure difference within the droplet may cause deformation which does not result from surface wettability. The optical measurement would record such an error and influence the fitting of the curvature (Krishnan et al., 2005). There were also findings (Krasovitski & Marmur, 2005) showing sliding may occur before the advancing or receding contact angles are reached. Some factors including the placement of the droplet and the droplet shape (Pierce, Carmona, & Amirfazli, 2008) were revealed later. This indicates that the tilted plate method is a relatively rough method to determine the dynamic contact angles.

The sessile drop method is a simple method based on optical imaging, which is easy for comprehension and visual clarity (Di Mundo & Palumbo, 2011;

Müller & Oehr, 2011; Strobel & Lyons, 2011). To perform the measurement is simply to place a droplet on the interesting areas (Buehrle, Herminghaus, & Mugele, 2003). Hence the method provides good compatibility and could be used on any part of a large surface.

In some experiments, the wetting properties of the whole sample surface are of interest. The Wilhelmy method will then be a better method than the Sessile drop method, as it reflects the average over a large surface quickly in a single test. For the Sessile drop method, a series of experiments on different locations are required, and sometimes it is not feasible to properly characterize an extremely large surface.

2.4.3 Water droplet bouncing behaviors on superhydrophobic surfaces

The dynamics of water droplets impacting a solid surface was coined in the early years in last century (Worthington, 1908). It has fascinated researchers' interest in recent years, concerning the remarkable wealth its industrial applications could bring about. These applications cover a wide variety of fields. One of the fundamental applications is spray cooling, which provides promising options for high rate heat transfer (Panão & Moreira, 2009). Drop-on-demand inkjet printing also benefits from the improvement on the physics of droplet impinging (Yusof et al., 2011). Droplet-based microfluidic is also a developing technology on food, chemical and biomedical industries (Dehghan Manshadi, Khojasteh, Mohammadi, & Kamali, 2016; Lakehal, Narayanan, Caviezel, von Rickenbach, & Reboux, 2013; Neužil, Giselbrecht, Länge, Huang, & Manz, 2012).

Water droplet impacting also plays an important role in superhydrophobic anti-icing (Sarkar & Farzaneh, 2009; C. Yang et al., 2016).

Different phenomena would arise when water droplets collide on a surface, which could be categorized as deposition, splashing, receding and rebound (Yarin, 2006). The outcome of a drop impacting on the surface is based on multiple factors including droplet properties (density, surface tension, viscosity, etc.), kinetic parameters and characteristics of the surface impacted. Some dimensionless parameters have been employed to account for the factors. The most crucial numbers are Reynolds number, $Re = \rho v L / \mu$, Weber number, $We = \rho v^2 L / \sigma$ and Capillary number, $Ca = \mu v / \sigma$, where v is the impact velocity, L is the characteristic length (the diameter for a droplet) and ρ , μ and σ are liquid density, dynamic viscosity and surface tension, respectively (Tsai, Pacheco, Pirat, Lefferts, & Lohse, 2009). The characteristics of the surface droplets impact on mainly refers to the surface geometries that can be altered through surface roughness and texturing, and the wettability which is controlled by surface energy and the roughness. Therefore, superhydrophobicity is associated with the water droplet bouncing behaviors.

Superhydrophobic surfaces increase the mobility of drops due to the reduced contact with water and decreased the contact angle hysteresis. A shear-free air-water interface is also formed under this condition and minimizes the viscous dissipation. The droplet impacting on such surfaces usually presents a complete or partial rebound or splashing. The outcomes are dependent on the impact velocity and the droplet properties. A falling drop collides a surface, converting its inertial energy into interfacial energy, reflected by the spreading and deformation. The extent of energy dissipation during the impact and interaction

with the surface will determine the rebound characteristics, since the droplet may either stick on the surface or rebound (Antonini, Villa, Bernagozzi, Amirfazli, & Marengo, 2013; Kim, Lee, Kim, & Kim, 2012; Y. Liu, Whyman, Bormashenko, Hao, & Wang, 2015).

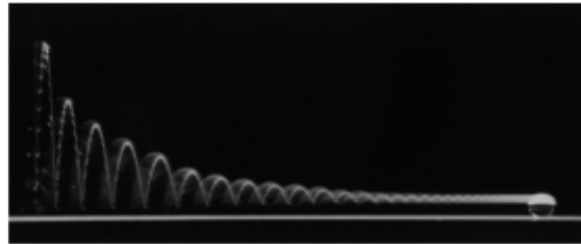


Fig. 2.19 The water droplet in motion illuminated by a continuous lamp. The plane where the drop lands is slightly tilted to reveal the whole trajectory. The vertical scale of the whole picture is 1 cm.

The water droplet bouncing process was carefully investigated both experimentally and theoretically by Richard (Denis Richard, Clanet, & Quéré, 2002; D. Richard & Quéré, 2000), which presented a comprehensive discussion on the impact process. Water droplets were able to bounce on a superhydrophobic surface for many times, as shown in Fig. 2.19, while the research focus was the first bounce of the whole process. In their work, rebound characteristics were analyzed. Three ways for energy dissipation were discussed. Besides water droplet experiments, balloon experiments were also designed and performed to mimic some ideal cases of water droplets. Their work is mainly focused on low Weber number not exceeding 1. Bouncing cases of extreme elasticity was achieved featured by a high restitution coefficient. It was believed that there was a limit for

the restitution coefficient, as the droplet would oscillate after the impact, transferring parts of the kinetic energy into oscillation.

Six possible outcomes were presented in a droplet impact experiment on a solid dry surface (Rioboo, Tropea, & Marengo, 2001). These outcomes shown in Fig. 2. 20, were yielded based on a variety of parameters including impact velocity, diameter of the droplet, dynamic viscosity and wettability of the surface. Improved impact velocity or wettability is beneficial for the outcome of rebound (partial rebound and complete rebound). Although rebound of water drops can also be facilitated by elevating surface temperature, especially when Leidenfrost effect occurs (Fujimoto & Hatta, 1996), it is more known and studied as a phenomenon in the process of bouncing on a superhydrophobic surface.

Besides the previously mentioned work by Ricard studying on curious phenomena of bouncing at very low We , Renardy et al. (Renardy et al., 2003) investigated the drop movement moderate impact velocities. They determined some criteria based on dimensionless parameters including Re , We and Ca for the conditions when the drop would form an Aztec pyramid shape, became toroidal or the drop center dried out.

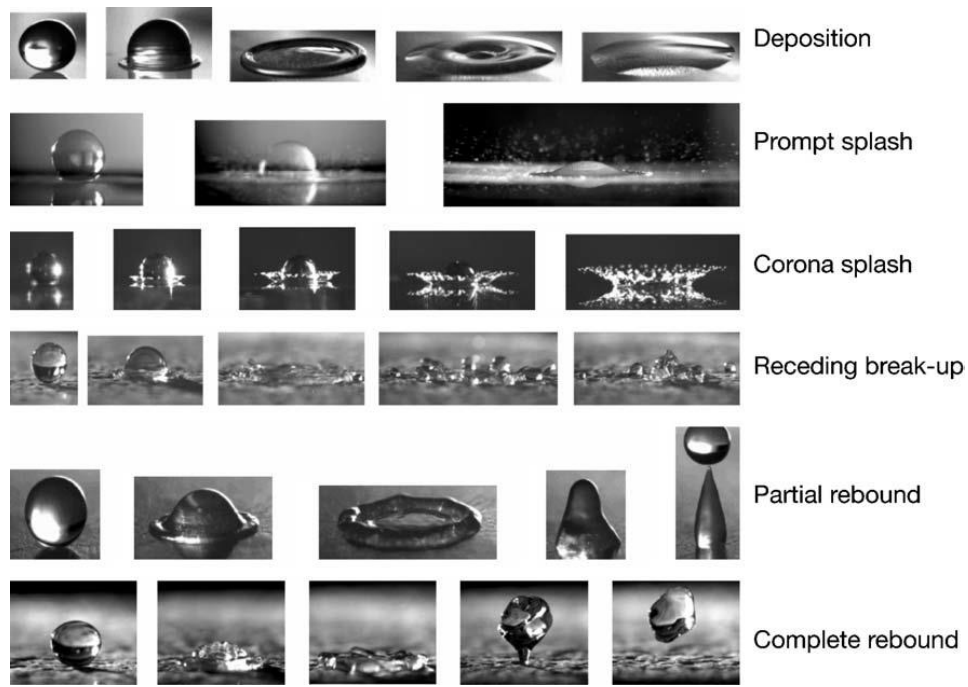


Fig. 2.20 Images of outcomes of normal impact of water droplets on a solid dry surface

Later researchers started trying out various methods to fabricate superhydrophobic surfaces and investigate droplet impact behaviors on them. Wang et al. (Z Wang, Lopez, Hirsra, & Koratkar, 2007) reported superhydrophobic carbon nanotube arrays with different wettability that display different responses for water droplet impact. They concluded in their experiments that droplets perform full rebound on superhydrophobic samples while got stuck less hydrophobic samples owing to the large contact angle hysteresis resulting in pinning of the contact line. Silicon based micropatterned surfaces fabricated from photolithography was investigated for the impact behaviors of a droplet on it (Yong Chae Jung & Bhushan, 2008). The transition of solid-air-liquid interface dependent on the drop and the surface geometry parameters was investigated in this work. Based on this work Nosonovsky (Nosonovsky & Bhushan, 2008)

focused on the energy barrier separating stuck and rebound states for impacting droplets. He proposed a third property of impacting droplet repelling ability besides the well-known CA and CAH, as a property that should be considered in the design of water-repellent surfaces.



Fig. 2.21 Dynamic interactions of droplets with different surfaces. (a) microtextured surfaces with large spacing, (b) microtextured surfaces with small spacing, (c) hierarchical textured surface and (d) nanoporous surface in Varanasi's work (Varanasi, Deng, Hsu, & Bhate, 2009).

As micropatterned structures and nanostructures have effect on surface wettability from different aspects, droplet bouncing on both individual structures and hierarchical structures have attracted researchers' interest these years. Tsai et al. (Tsai et al., 2009) fabricated such samples through catalytic vapor deposition

of carbon nanofilaments (CNFs) and micromolding of PDMS and conducted some comparisons. The two surfaces presented similar static contact angles and impact evolutions at small We , while splashing was more pronounced at larger We on CNFs surfaces with multiscale surface roughness. Varanasi et al. (Varanasi et al., 2009) tried out droplet impact on hierarchical structures comprising of micropost array with nanodentrites. His work was mainly about the ability to resist droplet impact at relatively large velocity and discussed the issue from the angle of pressure. Chen et al. (L. Chen, Xiao, Chan, Lee, & Li, 2011) prepared dual-scaled superhydrophobic surface by depositing carbon nanotubes on patterned silicon and compared its droplet impact interactions with that of a lotus leaf. The two materials present similar bouncing behaviors and abundant bouncing outcomes varying with impact velocity were tested.

Besides conventional CAs and CAHs, bouncing characteristics were studied to provide an indication of water repellency of a surface. Crick et al. (C. R. Crick & Parkin, 2011) proposed the number of bounces to define the hydrophobicity of a surface and first reported a linear relationship between the number of bounces and the static contact angle on a series of samples with similar microstructures. Spreading factor, which is a dimensionless number defined as the diameter of the spreading drop normalized by the original diameter, is another property used to characterize the hydrophobicity of the surface impacted (Antonini, Amirfazli, & Marengo, 2012; Kim et al., 2012; J. B. Lee & Lee, 2011). The spreading diameter is believed to slightly decrease with the increasing hydrophobicity of the surface at proper kinetic parameters. The restitution coefficient is another distinct property reflecting the surface hydrophobicity (Hao et al., 2015; B.-B. Wang, Zhao, & Yu, 2011). It is the ratio of the velocity after

impact to the velocity before impact. It usually exceeds 0.8 at low We for superhydrophobic surfaces and is believed to increase as the hydrophobicity is further improved.

In recent years, some special types of water droplet bouncing behaviors were also investigated. Droplets bouncing on superhydrophobic surfaces under an electric field was investigated (Khojasteh, Manshadi, Mousavi, & Kamali, 2016). The spreading diameter of the droplet was found to decrease significantly under high voltages. Bouncing on elastic surfaces were also investigated and compared with equivalent rigid surfaces (Weisensee, Tian, Miljkovic, & King, 2016). The elastic substrate bounced back the droplet, causing early retraction of droplet and thus reduced the contact time. A special type of drop rebound named pancake bouncing has been investigated in recent years (Y. Liu et al., 2014; Yahua Liu et al., 2015). It was featured with a flattened pancake shape when the drop just left the substrate. This was realized by designing surfaces with tapered textures behaving like springs and also caused reduction in contact time.

Although research on water droplet impact is not necessarily limited to a certain type of surfaces, the bouncing characteristics on superhydrophobic surfaces as properties to evaluate self-cleaning effect is worth further study. The underlying mechanism of synergetic effect of micro and nanostructures on hydrophobicity remains unclear. There is still some work to be done in studying the water droplet bouncing dependent on surface geometry.

2.5 Hydrophobic corrosion resistance

Corrosion is among the most important problems in our society. It induces serious damages to metal-based structure materials and causes great economic loss. Methods to increase corrosion resistance has therefore attracted researchers' interest. Hydrophobic/superhydrophobic coatings are believed to protect the underneath solid materials from wet corrosion. Many components are made of light metals or chemically active metals which are susceptible to corrosion. When they are used in specific applications where repelling water is essential, anticorrosion treatment becomes significant. Such components exist in various demanding applications including aerospace, automobiles, medical prostheses, architecture and electronic industry.

Hydrophobic surfaces improve corrosion resistance by limiting interactions with corrosive species, mostly water rich in ions, which easily speeds up electrochemical reactions to damage the solid surface. This can be explained from two aspects. Smooth metal surfaces without protective coatings corrode easily as the contact with aggressive solutions. The rough hydrophobic surface represents the formation of gaps within the surface structure. Air can be easily trapped in these gaps and forms a passivation layer. The ions in the aqueous media can barely invade the solid surface from the air layer. The actual area where hydrophobic surfaces are in contact with the aqueous media is decreased, which mean an improvement in corrosion resistance.

Capillarity is another important factor that can explain the improvement of hydrophobic surfaces in corrosion resistance. (T. Liu et al., 2007). The capillary pressure p_c can be calculated according to the Young-Laplace equation:

$$p_c = \frac{2\gamma\cos\theta}{R}$$

where γ is the surface tension, θ is the contact angle, R is the size of the gaps within the rough surface. When an SHPO surface is immersed in water, a considerable capillary pressure would be provided due to small structure dimensions and large contact angle. The corrosive aqueous media can be forced out because of the pressure and thus protection for the solid materials underneath is achieved. A general description of mechanisms in corrosion resistance improvement of superhydrophobic surfaces is shown in Fig. 2.22.

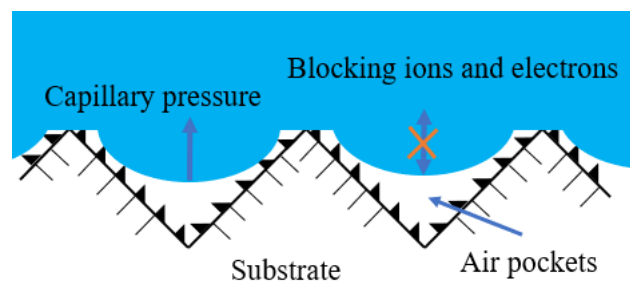


Fig. 2.22 A schematic diagram of corrosion resistance improved by superhydrophobicity

Many superhydrophobic surfaces have been fabricated to investigate the anticorrosion properties through varied characterization and analysis. As such surfaces are acquired in many cases on metal-based structure materials, laser-texturing is a popular method to provide a roughened base for gaining hydrophobicity (Emelyanenko et al., 2018; Gregorčič et al., 2017; Trdan et al., 2017). Another strategy is to attach superhydrophobic coating material onto the target surface with simple methods like spraying and dip-coating. Some measures including surface pretreatment and heating are applied to help solidification of the prepared coatings (Guo et al., 2020; Dawei Li, Ma, Zhang, & Chen, 2021).

Preparing metal oxide nanostructures followed by chemical modification is also a suitable and effective method to form hydrophobic/superhydrophobic surface on metals or alloy due to the affinity between metals and the corresponding oxides (W. Wu et al., 2020; Y. Yan et al., 2020).

It is noted that many of the results were irregular-structured surfaces or coating acting as hydrophobic corrosion inhibitor. Research on anticorrosion of hierarchical structures integrating regularly machined micro-structured base and secondary micro/nanostructures is still incomplete. Thorough studies might be performed in this area to reveal the role of hierarchical micro/nanostructures in hydrophobic corrosion resistance.

2.6 Summary

A review of the research background of superhydrophobic surfaces, the wetting theories, the fabrication methods and the applications in self-cleaning and corrosion resistance is presented in this chapter. Routes to improve hydrophobicity both from surface geometry and chemical composition have been reviewed. The advantages of ultraprecision machining and hydrothermal synthesis in fabrication of micro/nano-structures have been discussed.

The limitations of existing research have been identified through literature study. There has been limited work concerning the investigation of superhydrophobic micro/nano-structured surfaces in specific application fields including corrosion resistance and self-cleaning. The study on the effect of micro/nanostructures in surface wettability, especially in terms of specific superhydrophobic applications is incomplete. Investigation in comparison of

hydrophobicity micro/nano-structured surface and nanostructured surface with the same chemical composition is limited. Basic contact angle measurement cannot realize this comparison. Investigation of superhydrophobic micro/nano-structured surfaces on the performance of corrosion resistance and water droplet bouncing experiments could be conducted to contribute to filling these gaps.

Chapter 3 Methodology

Methods and techniques applied in this research can be divided into two categories: sample fabrication methods and characterization methods. To prepare hydrophobic/ superhydrophobic samples a set of fabrication methods were utilized including ultraprecision machining, electroless deposition and hydrothermal synthesis. Ultraprecision machining is used to fabricate groove patterns on copper substrate, which provides the geometry of the base structure. Electroless deposition is for depositing smooth nickel layer on the copper substrate. Hydrothermal synthesis is for preparation of metal oxide nanoparticles on flat or structured substrate.

Characterization of the fabricated samples includes morphological characterization, electrochemical characterization and surface wettability tests. To investigate the topography of the prepared samples, the interferometer and the scanning electron microscopy are used. X-ray diffraction is used to help determine the composition. Electrochemical characterization is conducted to evaluate the corrosion behavior. Wettability tests include the common contact angle measurements and also droplet impact test for advanced analysis.

3.1 Ultraprecision machining of microgrooves

In this research, ultraprecision machining is applied to fabricate microgroove and micropillar patterns on T2 copper. The ultra-precision machining experiments were conducted on a 4-axis ultra-precision machine Moore Nanotech 350FG, and the device and experimental setup is shown in Fig. 3.1. The fixture is

sucked on the spindle through vacuum chuck. There is a socket in the center of the fixture, where the copper substrate to be cut was fixed by Aron Alpha. The diamond tool was assembled facing the sample, with the rake face towards the Z+ direction.

The spindle performs translational movements in Z direction against the diamond tool to fabricate grooves. With multiple cuts along the sample surface and periodic move in X direction. Grooves of different geometric parameters can be fabricated on the whole surface. The spindle can turn 90° for similar moves and micropillar structures can thus be produced.

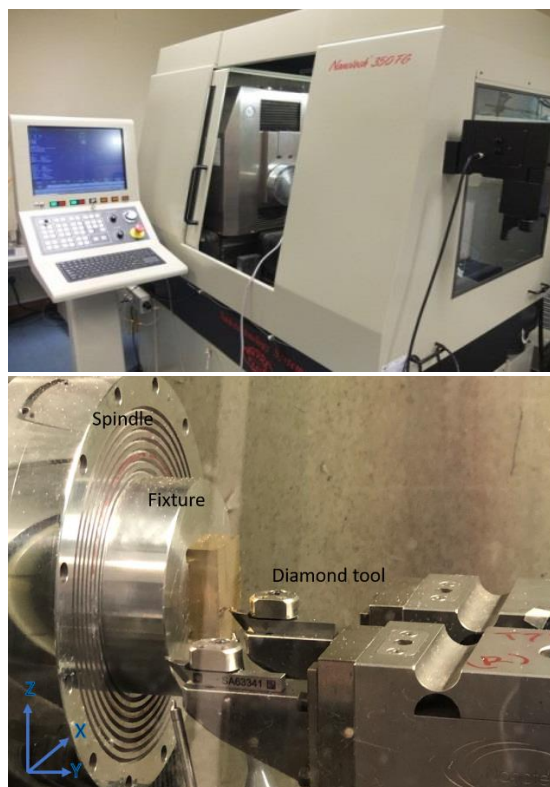


Fig. 3.1 Images of (a) Moore Nanotech 350FG and (b) experimental setup for machining

The cutting tool for the formation of the micropatterns is a facet diamond tool. Taking the microgroove structure as an example, the shape of the groove and the period is the key geometric parameters that should be considered. The period, depth and width of the grooves can be tuned through tool path, while the shape of the rake face of the tool determined a fixed slope of the trapezoidal cross-section. The selected diamond tool is shown in Fig. 3.2. The rake angle and the included angle are 0° and 30° , respectively. The tip of the tool is flat with a width of around $10\ \mu\text{m}$.

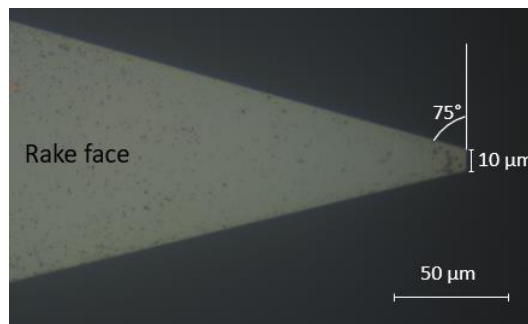


Fig. 3.2 The image of the tip of the facet diamond tool under an optical microscope

For all experiments, rough cut was performed to achieve a flat copper surface before prior to shaping of the target micropatterns. This ensures that the groove patterns on a large area of sample possess the same size and level. Considering the machinability of T2 copper, when the spindle moves along Z-direction against the diamond tool for groove shape fabrication, the depth of cut is $5\ \mu\text{m}$ and the feed rate is $200\ \text{mm}/\text{min}$. When the cutting process is finished, the fixture is immersed in acetone to remove Aron Alpha and to collect the sample.

The UPM fabricated surfaces could be observed under a Nexview three-dimension (3D) optical interferometer (Zygo). The 3D topographies of the machined surface acquired from the interferometer is analyzed in the software Vision 32 to yield the surface properties including roughness, cross-section profile, etc.

3.2 Hydrothermal synthesis of micro/nano-structures

Hydrothermal synthesis is among the most facile routes to prepare coating with rough structures on substrates. Usually this method yields metal oxide crystals with micro/nano structures possessing a rough topography. Meanwhile, a good coverage of metal oxide on metal-based substrates is relatively easy to achieve. Materials of low surface energy (fatty acid, siloxane, etc.) can be assembled on metal oxides. This makes hydrothermal synthesis a practical way to prepare hydrophobic coating on surfaces with micropatterns.

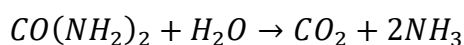
In this research, the substrates for all types of surfaces were T2 copper (Cu+Ag wt.% over 99.9) purchased from Quanfu Metal Co. (Shenzhen, China). The raw copper plates were firstly cut into intended dimensions through wire electrical discharge machining, which in most cases were 10 mm in length, 10 mm in width and 2 mm in thickness.

The hydrothermal synthesis of cuprous oxide in this research is based on the reaction of copper salt and urea in an aqueous medium with a heated and pressured circumstance. After some pretreatment to remove dirt and oxide layer from the surface, either the bare flat copper or UPM fabricated copper will be immersed in the hydrothermal bath and heated for reaction.

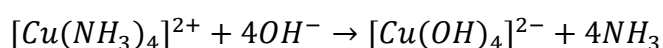
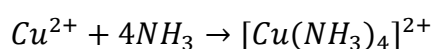


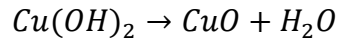
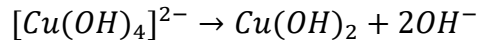
Fig. 3.3 The process of hydrothermal synthesis

The synthesis of cuprous oxide was carried out as follows. In a typical synthesis, 50 mL solution containing 0.25 g copper sulfate pentahydrate and 0.06 g urea were prepared and stirred uniformly. Then it was transferred to a Teflon-lined stainless-steel autoclave with the pretreated copper plate was immersed in it. The autoclave was sealed carefully and heated to 120°C for 6h in an oven. After the autoclave was cooled down to room temperature, the copper plate was collected from the solution and rinsed with copious distilled water to remove the free crystals. In this reaction, the hydrolysis of urea occurs when heated, as shown in the following equation.

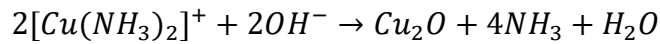
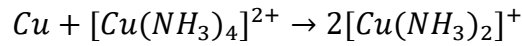


In aqueous solution, ammonia will provide hydroxide ions for formation of metal oxides. There are multiple possible reaction routes in this system. In the solution, the cupric ions will react as the following equations.





This is the common reactions in the solution where cupric oxide will be yielded from the corresponding salt, which would take place when heated in a sealed kettle. As copper is used as the substrate immersed in the hydrothermal bath, there will be different reactions on the copper surface given proper conditions. The possible reaction routes are presented as follows.



The CuO crystal yielded in the solution gradually subsides onto the sample surface and will be removed when the sample is washed with copious distilled water, as it is freely located instead of being deposited on the substrate. After dried in the oven at 80 °C for 2 h, the cuprous oxide coated sample was immersed in an ethanol solution (2.0 wt.%) of stearic acid (STA) for 2 h at room temperature, where spontaneous absorption of STA would occur. Finally, the acquired sample was rinsed with ethanol to remove the free STA and then dried in an oven.

Different metal oxide micro/nanostructures will be yielded in different hydrothermal baths. Nickel oxide among kinds of metal oxides is a typical material that can form nanostructures of different shapes and geometries through a facile hydrothermal method. As copper was chosen as the substrate to implement microgrooves fabrication by ultraprecision machining and would serve as the substrate to build a hierarchical superhydrophobic surface, measures should be taken to ensure the full coverage of nickel oxide crystals. Although copper itself

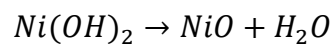
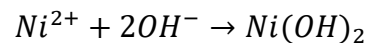
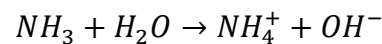
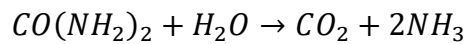
is a good substrate for hydrothermal synthesis compared with silicon or carbon-based materials, nickel has better affinity with nickel oxide. Therefore, electroless deposition (ELD) of a thin nickel layer onto the copper substrate was performed before it is coated with NiO layer.

Electroless deposition forms a uniform metallic layer on the sample surface through chemical reduction of the intended metal ions in an aqueous solution. The deposition of metal does not require electrical energy, thus reducing the requirement in the size and shape of the sample substrates to be coated. In most cases, surface modification for good adherence of the deposited layer is required prior to or simultaneously with the reduction process, as many target surfaces are fibers. In our case in this thesis, the modification step is unnecessary as nickel has good affinity with the copper substrate.

Electroless deposition of nickel on the copper substrate is carried out as follows. After polishing or UPM fabrication, the flat copper substrate or the micropatterned copper was immersed in diluted HCl solution to remove oxides and cleaned with ethanol and distilled water. It was then immersed in a nutrient solution for electroless deposition of nickel on the copper plate. The nutrient solution contained nickel sulfate hexahydrate ($\text{NiSO}_4 \cdot 6\text{H}_2\text{O}$), sodium citrate ($\text{C}_6\text{H}_5\text{Na}_3\text{O}_7$) and lactic acid ($\text{C}_3\text{H}_6\text{O}_3$). Nickel sulfate provides the source of nickel ions. Sodium citrate works as the complexing agent. Lactic acid is the buffer to keep the nutrient solution subacidic for Ni^{2+} storage. To start the deposition process, a proper amount of ammonium is added to adjust the pH of the solution to 7. Afterwards, borane dimethylamine (DMAB) aqueous solution is added to work as the reducing agent. After reaction for some time, a thin layer of nickel

with mirror-shine silver color is synthesized on the copper plate immersed in the solution.

Similarly, the nickel coated copper substrates will be immersed in a hydrothermal bath for the synthesis of NiO micro/nanostructures. The bath contains nickel nitrate hexahydrate ($\text{Ni}(\text{NO}_3)_2 \cdot 6\text{H}_2\text{O}$), sodium sulfate (Na_2SO_4) and urea. When sealed in an autoclave and heated in an oven, the following reactions occur and NiO is yielded.



After preparation, the morphology of Cu_2O and NiO film was examined under a Tescan Vega3 scanning electron microscopy. The phase composition of the crystalline structure of the products was analyzed by X-ray diffraction (XRD) on a Rigaku Smartlab diffractometer. The XRD test is especially essential to assist in determining the product of copper salt hydrothermal bath because of its multiple oxidation states.

3.3 Electrochemical characterization

Electrochemical testing is applied to evaluate the hydrophobic corrosion resistance properties of all the prepared samples. In all cases, the corrosion

resistance testes were carried out in a 3.5 wt.% aqueous NaCl solution as the electrolyte. A conventional three-electrode system was used with a saturated Ag/AgCl electrode as the reference electrode and carbon stick electrodes as the counter electrode. The working electrode is prepared by sealing the coated sample with silicone rubber, and electrically connected with the CHI660e electrochemical workstation (Shanghai Chenhua Instrument Co., China) through an embedded copper film. The area of exposed part of the sample surface is measured under an optical microscope and calculated using the software LAS X (Leica Microsystems).

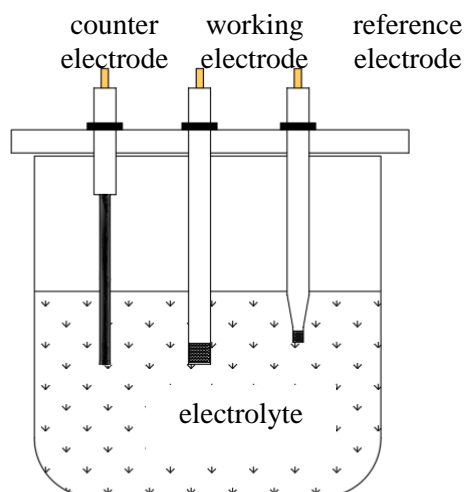


Fig. 3.4 The schematic of a three-electrode electrochemical cell

The electrochemical techniques utilized to test the corrosion resistance behaviors include time based open circuit potential (OCPT), electrochemical impedance spectroscopy (EIS) and Tafel polarization. The OPCT technique measures the open circuit potential of the working electrode with respect to the

reference electrode. It reflects the tendency of a material to be oxidized and is also used as a parameter in the EIS technique. The EIS technique obtains the electric impedance of a substance as a function of the frequency. It is well-established method for the evaluation of corrosion resistance performance. A large impedance at low frequencies indicates good anti-corrosion performance. The Tafel polarization is a procedure to experimentally evaluate the corrosion current, which reflects the corrosion rates if the reaction is performed on a unit area. A potential scan is performed to determine a linear section for a reasonably accurate extrapolation to gain the current value at the corrosion potential intersection.

3.4 Contact angle measurement

Contact angles including the static contact angle and the dynamic contact angle are measured to quantify the wettability of the prepared sample surfaces. The tests are performed on a contact angle goniometer Sindatek Model 100SB, which is conducted through the software MagicDroplet. Both static contact angles and dynamic contact angles are measured using this model.

The sessile drop method best suits the test conditions in this research and is applied for contact angle measurements. The water droplet is dispersed from the syringe and laid on the sample surface. The droplet and the sample are approaching very slowly to ensure that there is little droplet impact. The curvature between the interfaces is recorded to calculate the contact angle. The droplet sitting on the sample surface is captured by an optical subsystem of the goniometer where high-resolution cameras are used to analyze the profile of the liquid drop and the contact angle.

Dynamic contact angles are measured where superhydrophobic surfaces present good sliding properties and measurement of static contact angles is difficult to operate. Measures to experimentally evaluate the dynamic contact angles are categorized into three: tilted plate method, sessile drop method and the Wilhelmy method. Considering the existing experimental setup based on the goniometer, the Wilhelmy method would be eliminated. Owing to the extreme sliding properties of the prepared sample, the Sessile drop method is selected. The liquid is pumped into and out of an existing droplet, which is sitting on the sample surface with a changing volume. In this process, the advancing contact angle is achieved when the baseline is advancing and receding contact angle is achieved as the baseline is decreasing, respectively.

3.5 Water droplet bouncing experiments

There are other ways to evaluate the wettability of a surface other than the most commonly used CA and CAH measurement. The water bouncing experiment is believed to be effective to reflect surface wettability. The products of the experiment including the rebound height, the contact time, the spreading factor, etc. are used to quantify the hydrophobicity. While CAs and CAHs might be extremely close in some cases for different sample surfaces, these properties of droplet bouncing could provide evidence to distinguish the differences in wettability of hydrophobic surfaces.

Such experiments are conducted briefly as follows. The samples are placed on a horizontal sample stage, under a needle where water droplets would be dispensed. The process of droplet impacting the sample surface would be recorded

using a high-speed camera. The images would be analyzed to acquire the properties of the droplet impact process. Under controlled droplet volume and releasing height, the droplet bouncing behaviors will reflect the surface properties the drops impact on. Droplets do not bounce or present partial bounce on less hydrophobic surfaces. On superhydrophobic surfaces, the droplets will bounce for several times before deposited on the surface or slip off the surface. In general, the surfaces with better superhydrophobicity will present a larger rebound height, smaller water-surface contact time and a larger spreading factor. The properties can be calculated by measuring the deformation and displacement of the images of bouncing movement recorded by the high-speed camera in an open source software ImageJ.

Chapter 4 Investigation of micro/nano-structured surfaces fabricated by UPM and hydrothermal synthesis on surface wettability

4.1 Introduction

Controlling of wetting of surfaces is an important problem associated with technologies in many fields. Concretely speaking, the interest in superhydrophobic surfaces keeps rising due to the need for fabrication of such surfaces for vehicle outer-shells, energy devices, architectural glass and so on. In most cases, the superhydrophobic surfaces involve solid surfaces, although the concept comes from the leaves of plant and wings of insects.

Ultraprecision machining is an effective method to manufacture microstructures with geometries of high precision. Ultra-precision machining can work many types of materials including metals, hard-to-machine materials (hard alloy), and hard-brittle non-metal materials (ceramics and glass) (J. Yuan et al., 2017). Among them, copper is metal that has a number of industrial applications due to its good properties (Antonijevic & Petrovic, 2008). In this research it was chosen as the base to fabricate the superhydrophobic surfaces.

To fabricate structures in nanoscale on either flat copper surface or UPM machined microstructured surface, hydrothermal synthesis is believed to be an effective and facile method. This method usually produces metal oxides with micro/nano-structures. Copper oxides and nickel oxides are typical materials among the products of hydrothermal synthesis. They can be grown easily on metal-

based solid substrates and achieve good coverage given proper conditions. Subsequently, materials of low surface energy (most commonly used fatty acid and siloxane) would be modified on the prepared metal oxide layer through spontaneous reactions, which is a common strategy to form a superhydrophobic film.

In this research ultra-precision machining is applied in combination with hydrothermal synthesis used to fabricate superhydrophobic surfaces. Different micropatterns including microgrooves and micropillars will be fabricated on T2 copper through UPM acts as the base for the secondary metal oxide layer. Nickel oxide based nanosphere superhydrophobic coating were prepared. FAS-17 were modified on the oxides to achieve hydrophobicity. To enhance the adhesion between NiO and copper substrate, a nickel layer was deposited. Morphological characterization is performed under the optical microscope, the interferometer and the scanning electron microscopy. Contact angles, contact angle hysteresis and the sliding angle were measured to evaluate the wettability of the prepared surfaces using a goniometer. Both static and dynamic wetting properties will be discussed. As microgroove patterns will be fabricated, the anisotropy of the surfaces, before and after metal oxide coating, will also be discussed in terms of wettability.

4.2 Experimental details

4.2.1 Ultraprecision machining of microgroove surfaces

Ultraprecision machining was performed on commercially purchased T2 copper (Quanfu Metal Co., Shenzhen, China) to fabricate micropatterns including

microgrooves and micropillars. Basic setup of the machine tools is stated in Chapter 3 and additional details will be presented in this section.

The purchased T2 copper plate is first cut into pieces with a dimension of $10\text{ mm} \times 10\text{ mm} \times 2\text{ mm}$ by wire-cut electrical discharge machining. The sample was then assembled for the machining process, which can be divided into three phases. The first phase is rough cut. The blank sample was cut for up to several tens of microns to remove the defects and unevenness. A flat copper surface with a roughness of several nanometers can be acquired in this process. The second phase is the formation of target groove/pillar shape. To fabricate patterns with different geometries, different tool paths were designed according to the specific size of the shapes. A single groove was fabricated with a $5\text{ }\mu\text{m}$ depth of cut along one direction of the copper surface. The diamond tool was then moved to the same end with a slight shift for another cut. The target shape would be achieved after a few cuts. Then the diamond tool was shifted for a certain period to repeat the process to fabricate grooves on the whole surface. To fabricate the micropillar surface, a repeated cutting process of the microgroove fabrication could be performed after 90° rotation of the fixture. The combination of tool path for microgrooves in two directions perpendicular to each other will yield the pattern of square pillars array. In the third phase, the diamond tool is lifted up for a certain distance to cut the whole surface. This final cut is to remove the distorted parts at the upper line of the trapezoidal grooves.

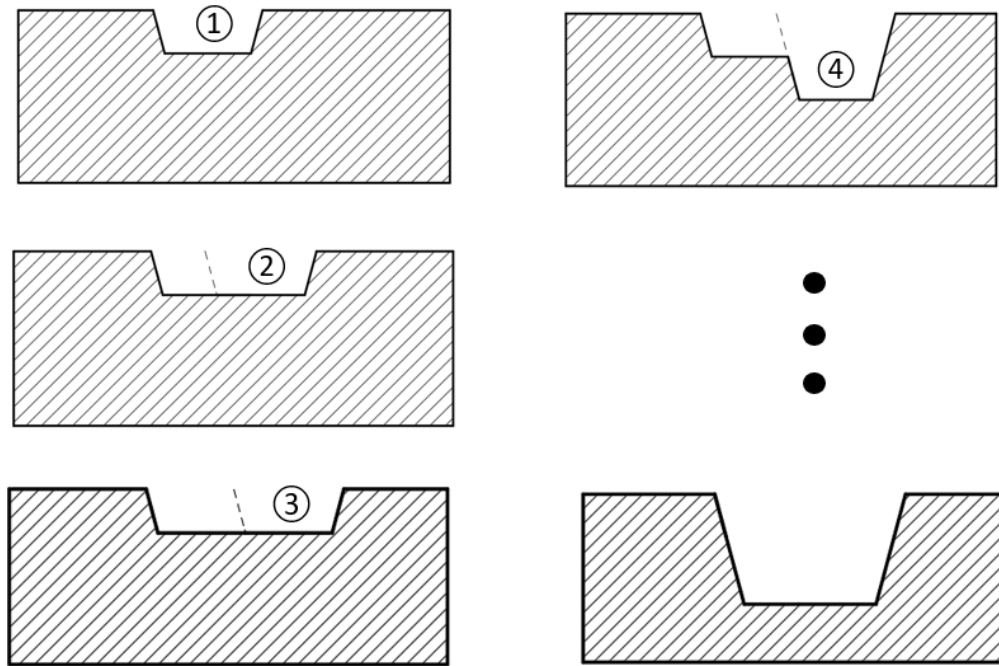


Fig. 4.1 The schematic diagram to show the sequence to fabricate a single microgroove

4.2.2 Hydrothermal synthesis of Cu_2O layer

The UPM fabricated copper plates acted as the substrates for the hydrothermal synthesis of cuprous oxide. Copper sulfate pentahydrate ($\text{CuSO}_4 \cdot 5\text{H}_2\text{O}$) and stearic acid ($\text{C}_{18}\text{H}_{36}\text{O}_2$) were obtained from Alfa Aesar. HCl, urea, ethanol and acetone were acquired from Sinopharm (Beijing, China). All the reagents were of analytical purity and did not need further purification.

The copper substrate was first immersed in 3 wt.% HCl for about 20 min to remove oxide layer from the surface. Then it was ultrasonically cleaned with acetone, ethanol and distilled water for 10 min each in sequence.

The detailed procedure of preparation of cuprous oxide has been described in Section 3.2 and will not be stated here. A dark layer could be observed by naked eye to have formed on the collected copper substrate after hydrothermal reaction. Cleaning, drying and treatment with STA were also performed. The heating time, temperature and concentration of the hydrothermal bath were tuned to see if changes in morphology of Cu_2O crystals would happen, which might have an effect on the wettability properties in subsequent tests.

4.2.3 Hydrothermal synthesis of NiO layer

Copper plates serving as the substrate for NiO layer preparation were the same T2 copper as that for Cu_2O . $\text{NiSO}_4 \cdot 6\text{H}_2\text{O}$ and Na_2SO_4 were obtained from Alfa Aesar. HCl, NaCl, urea, ethanol and acetone were acquired from Sinopharm (Beijing, China). 1H, 1H, 2H, 2H-perfluorodecyltriethoxysilane (FAS-17) was purchased from Sigma-Aldrich. All the reagents were of analytical purity and do not need further purification.

After similar pretreatment, the copper plates were immersed in the bath for the hydrothermal synthesis. A typical process was carried out as follows. The samples were immersed in 50 mL aqueous solution with 20 mM NiSO_4 and 20 mM urea and 20 mM Na_2SO_4 , sealed in a Teflon autoclave and heated at 150 °C for 2h. After cooled down, the samples were rinsed with distilled water and dried for 1h at 80°C. To form a layer of FAS-17 on the prepared oxides, the acquired sample was immersed in an ethanol solution (1.0% wt) of FAS-17 ethanol solution. Finally, the sample was washed with ethanol to remove free FAS-17 and then heated at 120°C for an hour.

The preparation of NiO could be directly performed on copper substrate, but it is better to deposit NiO on nickel, which presents better affinity than copper and thus strengthen the adhesion between the substrate and NiO nanocrystals. A layer of nickel could be formed on copper prior to the hydrothermal synthesis process through electroless deposition. The process was carried out as follows. The pretreated copper plate was immersed in 50 mL nutrient solution for electroless deposition of nickel on the copper plate. The nutrient solution contained 2 g nickel sulfate hexahydrate, 1g sodium citrate and 1 g lactic acid. Before the deposition process, about 2 mL ammonium was added to adjust the pH of the solution to 7. Afterwards, 10% wt. borane dimethylamine aqueous solution was added to start the reaction process. After about 20 minutes of the deposition process, a thin layer of nickel was synthesized on the copper plate.

4.2.4 Characterization methods

The profile of the UPM fabricated microgroove surfaces was observed using a white light interferometer Zygo Nexview. The cross-section view was also acquired to show the depths of the groove gaps on different samples. The morphology of Cu₂O and NiO layer was examined using a Tescan Vega 3 scanning electron microscopy. XRD (X-ray diffraction) was performed under a Rigaku Smartlab to confirm the composition of the metal oxide crystals. The wettability of the samples was tested using a contact angle goniometer Sindatek Model 100SB. The static contact angle and the dynamic contact angle were measured using Sessile drop method. The contact line for samples with small contact angles could be observed under an optical microscope.

4.3 Results and discussion

4.3.1 Topography of UPM fabricated microgrooves

Microgrooves with different geometries were fabricated on copper surface through ultraprecision machining. The acquired patterns were observed under the interferometer Zygo Nexview and the precise dimensions were measured, as presented in Table 4.1 and 4.2. Microgroove surfaces with 30 μm groove width were fabricated while the grate width and the groove depth are tuned. Different grate widths would result in different groove periods and the theoretical air faction ratio on the patterned surface could thus vary. According to the measured dimensions, the actual size of the geometries was very close to the designed values. The surface roughness also reaches very small values of several nanometers. This indicates a satisfactory output of the machining of the microgroove surfaces.

Table. 4.1 The geometric parameters of a microgroove surface with different groove depth

Designed depth of 30-30 microgrooves / μm	Groove depth / μm	Groove period / μm	Roughness /nm
9	8.9	59.0	2.51
18	18.6	59.6	4.07
27	27.3	59.4	7.23
36	36.1	59.8	5.04

Table. 4.2 The geometric parameters of the 18 μm -depth microgroove surfaces with different groove period

Designed period	Groove width / μm	Groove period / μm	Roughness /nm
35	26.1	34.9	4.25
45	27.4	43.4	7.65
60	29.8	60.6	3.56
90	28.8	89.7	3.22
130	29.6	131.6	3.53

As stated in section 4.2.1, the formation of the microgrooves ended up with a final cut. After formation of the groove shape on the copper surface, the diamond tool was lifted up for a certain distance to move on the whole sample surface, aiming at removing the distorted copper. The sample surface without executing this step was also observed under the interferometer, as shown in Fig. 4.2. The distorted part exists at the edge of a single groove and can be as high as 5 μm over the groove surface, which would significantly influence the form accuracy.

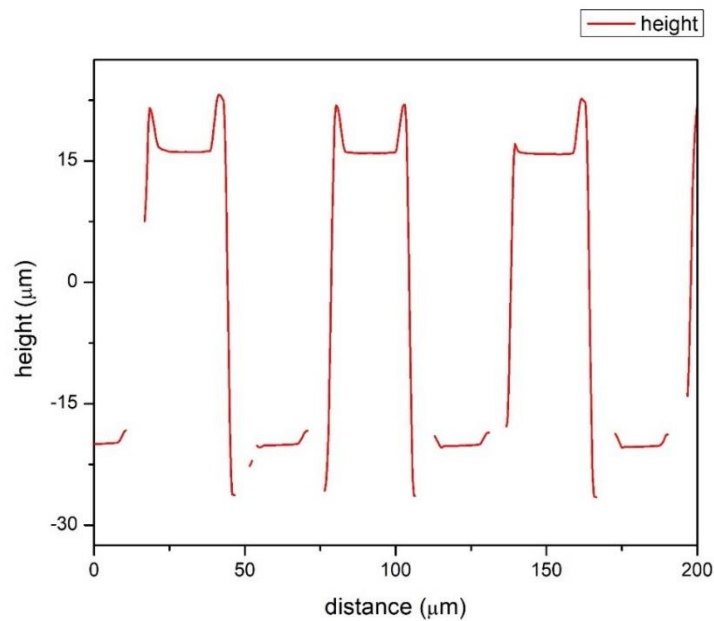
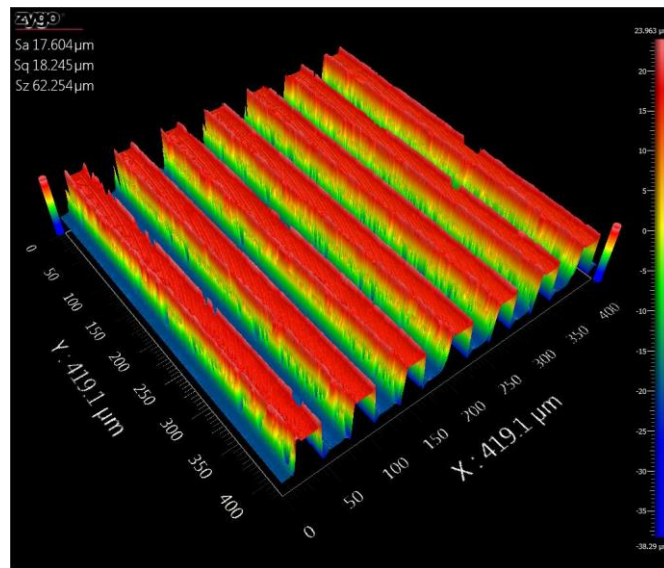
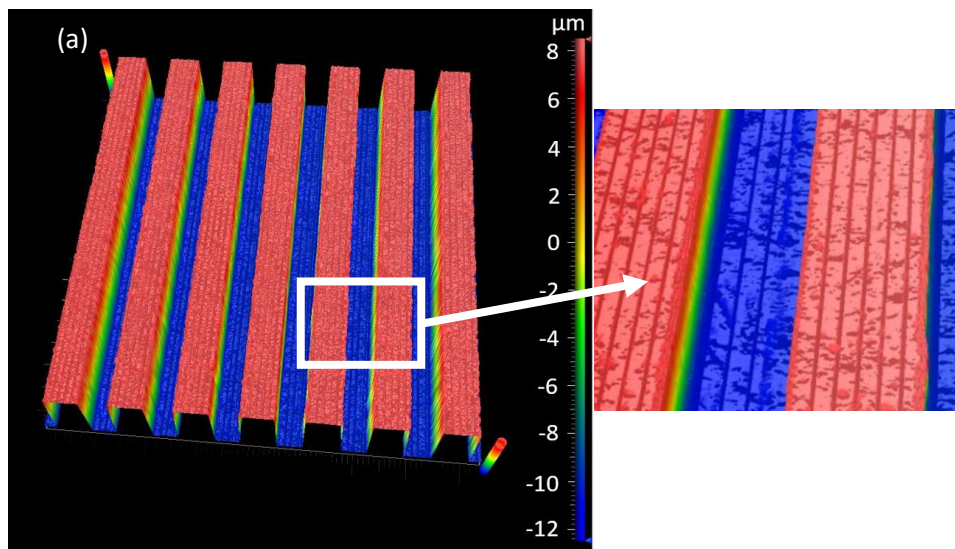


Fig. 4.2 The images of the machined surface exactly after groove shape formation. Distinct distorted parts could be seen at the edge of the grooves

The topography and cross-section measured using the interferometer were shown in Fig. 4.3. The displayed microgroove surface as a representative possesses a groove depth of 18 μm and a groove width of 30 μm. The period of

the groove structure is 60 μm . From the measured results showing the cross-section view perpendicular to the grooves in Fig. 3(b), the fabricated surface presented good form accuracy. The minor deviations resulted from vibration of the tool and material elastic recovery. Measuring the surface area within a single grate or groove, the machined surface was smooth with a satisfactory roughness no larger than 0.01 μm . In comparison, the microgrooves modified with Cu_2O -STA layer is shown in Fig. 4.3(c). The surface becomes distinctly rough after the modification. Meanwhile, the height of Cu_2O -STA groove remained almost the same with that before coating. This indicates that the fabrication of secondary structure has roughly retained the designed shape of the base microgrooves.



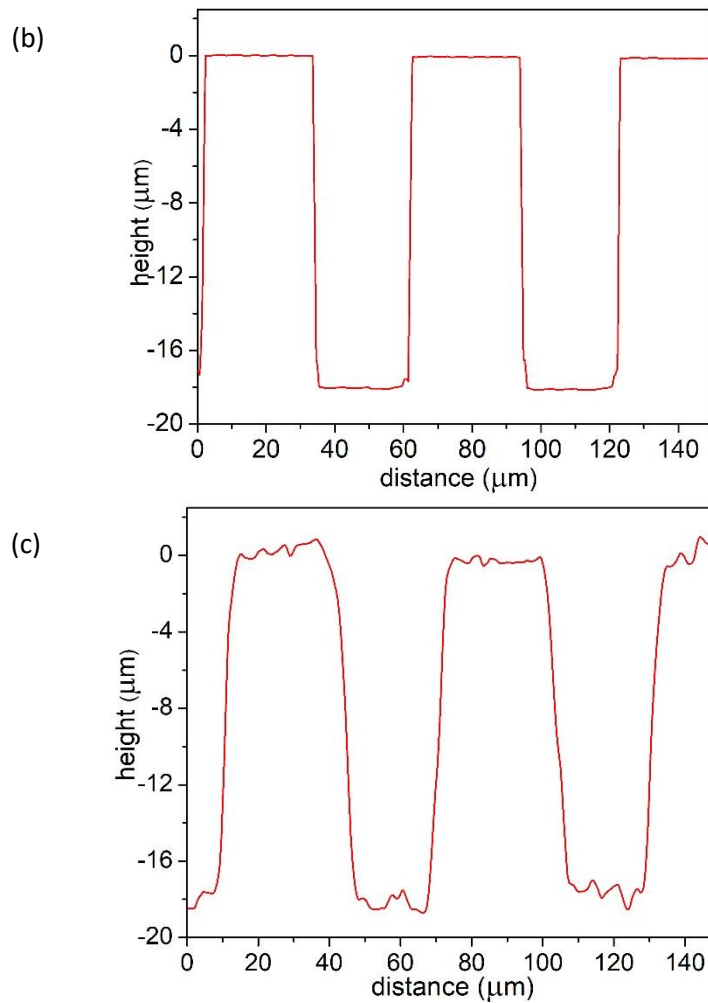


Fig. 4.3 Surface profile acquired by the interferometer. (a) the 3D plot of the copper microgrooves, (b) cross-section view perpendicular to the groove direction of copper microgrooves and (c) cross-section view of microgrooves after coated with cuprous oxide.

4.3.2 Morphology of micro/nano crystals acquired by hydrothermal synthesis

Parameters of hydrothermal preparation of the Cu_2O layer were tuned to find the different outcomes of the morphology. The parameters included the concentration of the deposition bath, the temperature, and the time length. In this work the concentration was tuned without changing the proportion of each component of the bath. In general, the product of the $\text{CuSO}_4 + \text{CO}(\text{NH}_2)_2$ bath was

rectangular shaped cuprous oxide crystals while the amount and coverage varied under different parameters. Lower temperature, smaller bath concentration and shorter heating time would result in poor coverage and thinner layer of cuprous oxide. Temperature and bath concentration are two dominant factors on the amount of the formation of the cuprous oxide layer. As presented in Fig 4.4 and 4.5, the amount of cuprous oxide crystals is accumulated as the temperature and concentration increases. When the two parameters are smaller, the Cu_2O layer was thin and bare copper substrate could be seen. This is natural because the growing speed of the crystals increasing is affected by the temperature and the salt concentration. The needle-like CuO_x could be observed in some areas of the samples. It is originally produced in the solution falls onto the substrate and can be washed away with distilled water and mild ultrasonic vibration, and thus could not be considered as part of a robust film. Although small difference in morphology was discovered between individual batch of synthesis, good coverage of Cu_2O layer could be repeatedly observed when the temperature is no lower than 120°C and bath concentration no smaller than 20 mM concentration. Considering a long reaction heating time to ensure full coverage, 20 mM concentration, 120°C and 6 h heating time were chosen as the parameters for the hydrothermal synthesis of a satisfactory cuprous oxide layer.

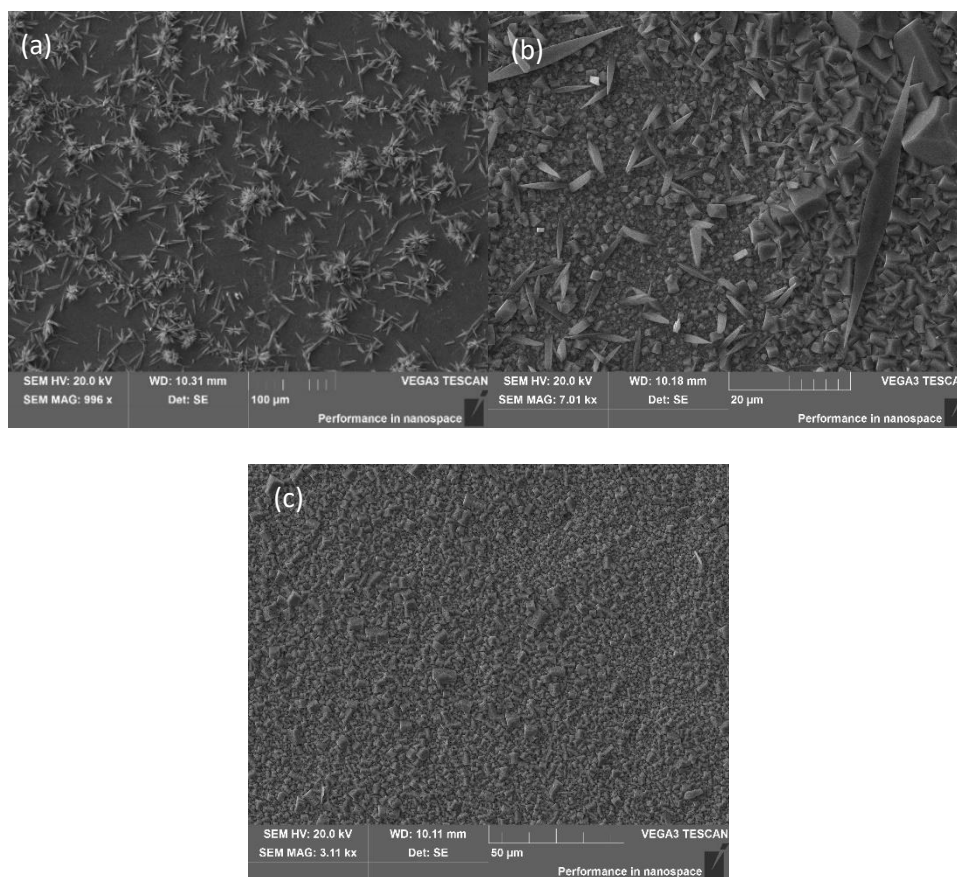


Fig. 4.4 SEM images of cuprous oxide on copper substrate prepared under different heating temperature (a) 90°C(b)110°C and (c)130°. The bath concentration is 20mM and the heating time is 2h. In some images the larges needles are free oxide sediments that are not washed away.

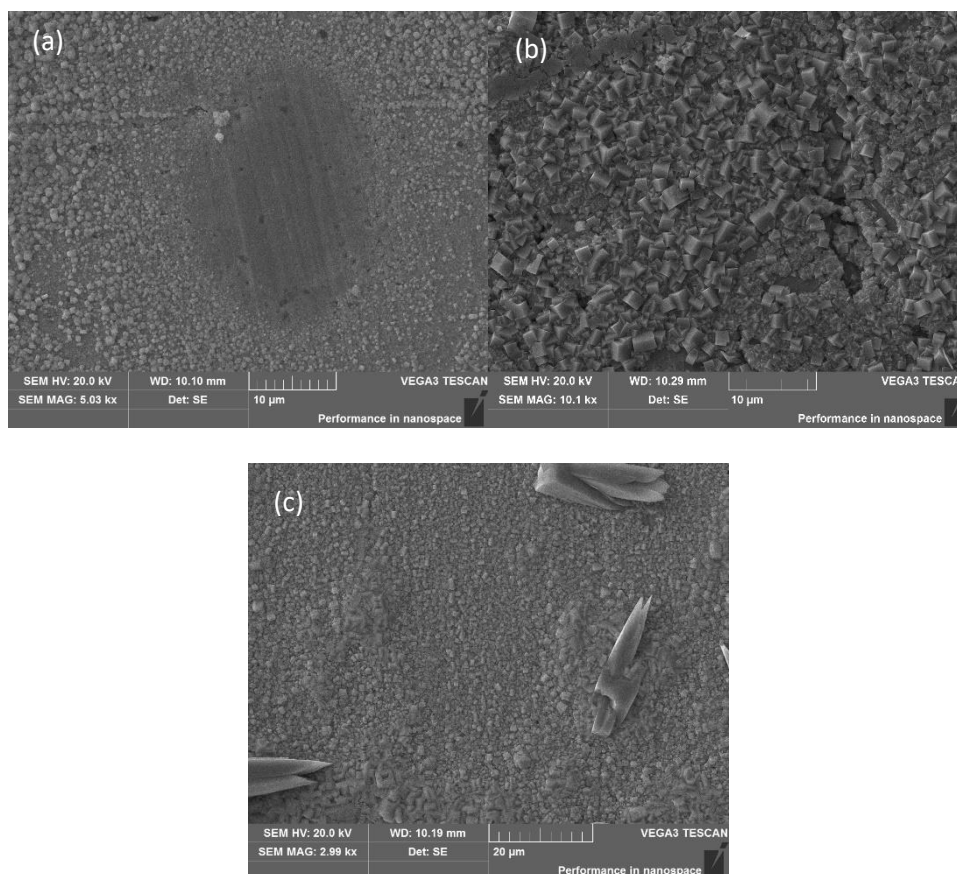


Fig. 4.5 SEM images of cuprous oxide on copper substrate prepared under different bath concentrations (a)5mM (b) 10mM and (c) 20mM. The temperature is 90°C and the heating time is 6h. In some images the larges needles are free oxide sediments that are not washed away.

To verify the phase and composition of the acquired oxide through hydrothermal synthesis, XRD analysis was performed on the prepared sample. The XRD pattern was shown in Fig. 4.6. Sharp diffraction peaks around 29°, 37°, 43° and 62° are corresponding to planes (110), (111), (200), (220) of Cu_2O , which provide a clear evidence for the formation of cuprous oxide. The peaks around 44° and 51° are corresponding to planes (111) and (200) of copper, respectively. The

large intensity of Cu peaks is owing to copper as the sample substrate. No side products such as CuO and Cu(OH)₂ were detected.

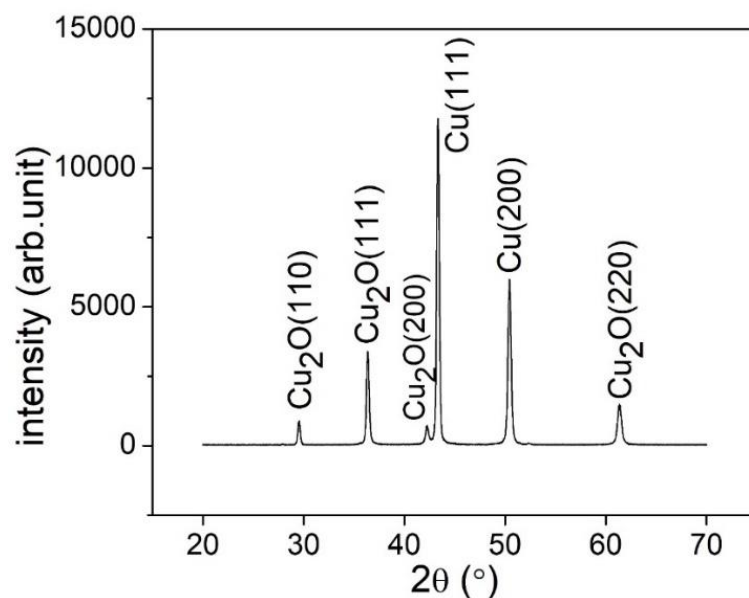


Fig. 4.6 XRD of prepared Cu₂O film on copper substrate

The nickel oxide is another metal oxide that receives extensive studies on its fabrication through hydrothermal methods. Compared to cuprous oxide, NiO tends to form flake or rod structures with a smaller scale instead of rectangular-shaped or octahedra crystals in a dimension of several microns. Therefore NiO was studied and fabricated in addition to Cu₂O in this work. The acquired NiO layer covered the nickel coating, which was a dark layer the silver nickel surface at visual inspection. The samples were examined by SEM and displayed as in Fig. 4.7. NiO nanoflakes were evenly deposited with some microspheres scattered on the surface. A detailed image of the surface is shown in a zoom-in view of the nickel oxide surface showing that the sphere-like structures are aggregation of the nanoflakes. The bottom layer is also nanoflakes that was vertically distributed. The

nanoflakes had an edge length of 1 – 2 μm and the thickness was no more than 100 nm. The size of the spheres is from 3 to 6 μm in diameter.

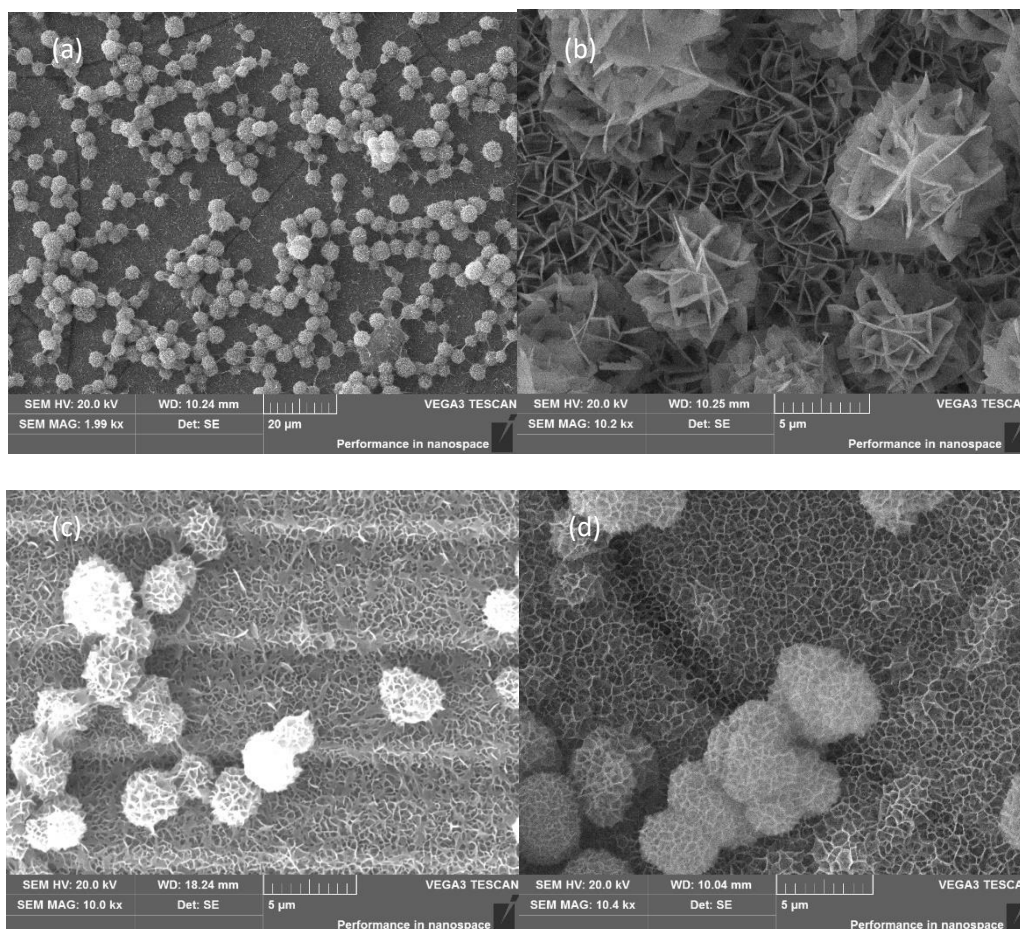


Fig. 4.7 The NiO nanoflake layer observed under the SEM. The magnified ($\times 1000$) view of sample from (a) 20 mM hydrothermal bath, the zoom-in ($\times 10000$) view of sample from (b) 4 mM hydrothermal bath, (c) 20 mM hydrothermal bath and (d) 100 mM hydrothermal bath.

Among the three main parameters for hydrothermal synthesis, the temperature and the heating time length were set as the empirical value of 150 $^{\circ}\text{C}$ and 2 h, respectively. The concentration of the hydrothermal bath was studied with the fixed proportion of the contents ($\text{Ni}(\text{NO}_3)_2$, $\text{CO}(\text{NH}_2)_2$ and Na_2SO_4). The SEM

images of the nickel oxide layer prepared at hydrothermal bath solution concentrations of 4 mM, 20 mM and 100 mM are displayed in Fig. 4.7. It can be observed that the resulting samples possess similar morphology with nanoflakes at the bottom and microspheres formed by gathered nanoflakes on the top. There is no significant difference in the density of the microspheres. The main difference is in the size and amount of nanoflakes. When the concentration of the hydrothermal bath is higher, the growth of flakes is denser, and the microspheres are smaller and have a more regular shape.

4.3.3 Surface wettability and anisotropy

The static contact angle is the most common feature to characterize the wettability of a surface. It can be predicted based on the two well-known models, the Wenzel model and the Cassie & Baxter model. The Wenzel model describes a droplet that completely wets the structured surface. The static contact angle under the Wenzel regime can be presented as:

$$\cos \theta_w = r \cos \theta_0$$

The terms in the equation have been stated in previous chapters and will not be stated here. In this work, for the microgroove surface fabricated using UPM, the roughness ratio r can be calculated according to the picture showing the geometry of the structures. The roughness ratio r of the microgroove surface is:

$$r = \frac{s + w + 2h(\csc \beta - \cot \beta)}{s + w}$$

where s is the width of the grates, i.e., the spacing of the grooves, w is the width of the grooves, h is the depth of the grooves and β is the angle of the slope of the

grates (75° in this research), which is determined by the shape of the faucet diamond tool. The Wenzel model is supposed to be applied on the copper microgroove surface and nickel coated copper microgroove surface, where the water repellency is relatively low that the droplet may penetrate the grooves.

The Cassie & Baxter model described a droplet with air occupying the gaps of the surface structures. The static contact angle was expressed as

$$\cos \theta_c = R_f f \cos \theta_0 + f - 1$$

As the contact is different in these two models, the area fraction of wet area for microgroove surface is calculated to be

$$f = \frac{s}{s + w}$$

where s is the width of the grates and w is the width of the grooves. In this research, for UPM fabricated surfaces, the roughness ratio was assumed to be 1 because the UPM machined surface reached a very small surface roughness. The equations above could help predict the static contact angles of droplets on different structured surfaces.

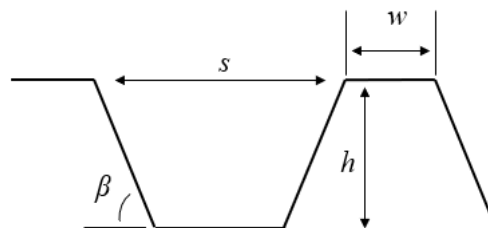
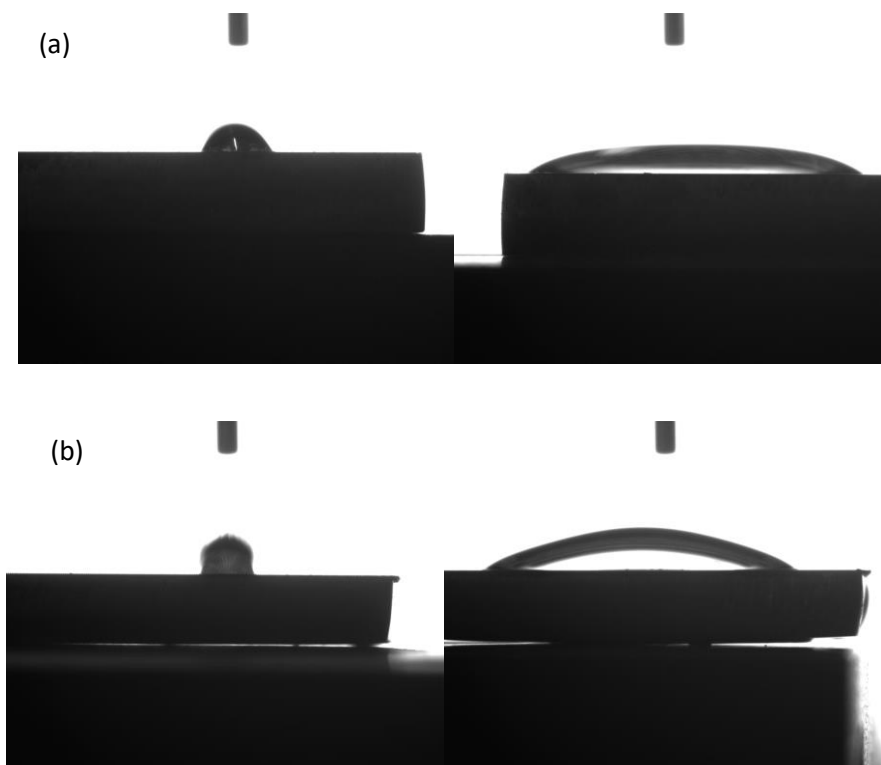


Fig. 4.8 The schematic showing the geometric terms of the microgrooves

Prior to the coating process where superhydrophobic surfaces are prepared, the UPM fabricated copper surfaces as the substrate were tested to evaluate the wettability and anisotropy. A water droplet of 5 μL volume was dispensed onto the copper surfaces with different geometries on the goniometer sample stage. The tested plates possess a fixed groove width of 30 μm , a fixed groove depth of 18 μm and increasing groove period of 35 μm , 45 μm , 60 μm , 90 μm and 130 μm , which were denoted as 5-30, 15-30, 30-30, 60-30 and 100-30 microgrooves correspondingly. The anisotropy in geometry would result in anisotropy in terms of wettability. Accordingly, the water droplets deposited on the microgroove surfaces were viewed from two directions parallel to the grooves (denoted as parallel) and perpendicular to the grooves (denoted as orthogonal). A series of images taken on the goniometer were shown in Fig. 4.9.



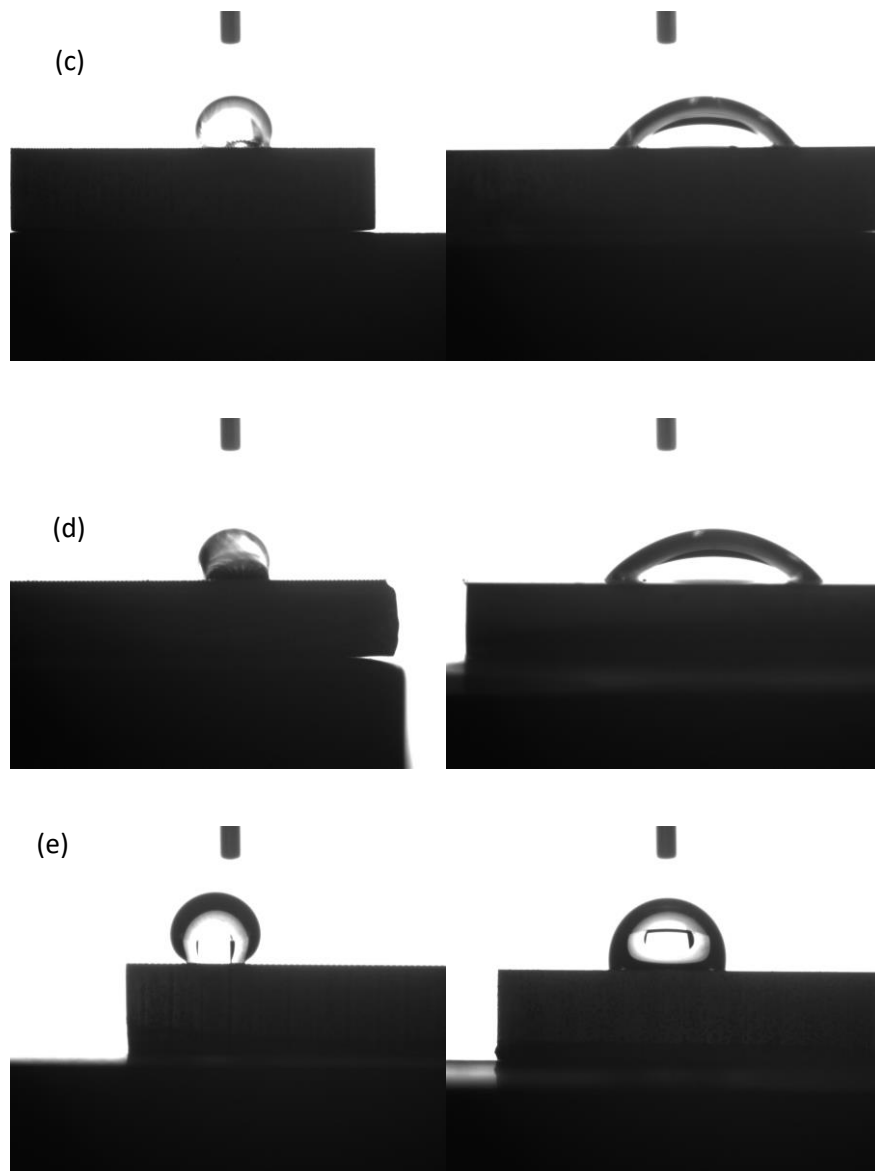


Fig. 4.9 The droplets on microgroove surfaces viewed from different directions under a goniometer (a) 5-30 microgroove surface (b) 15-30 microgroove surface (c) 30-30 microgroove (d) 60-30 microgroove (e) 100-30 microgroove.

Judging from the static droplet contour on the copper surface from the two different directions, the wetting behaviors varied depending on the period of the microgrooves. The drop stretches along the grooves, and therefore presents a

hemisphere in the parallel direction and a minor arc in the orthogonal direction. The change in radius reflected that the sparsely distributed grooves would better support the water droplet while on the close-packed groove the droplet tended to spread. This is due to the penetration of water into the copper microgrooves.

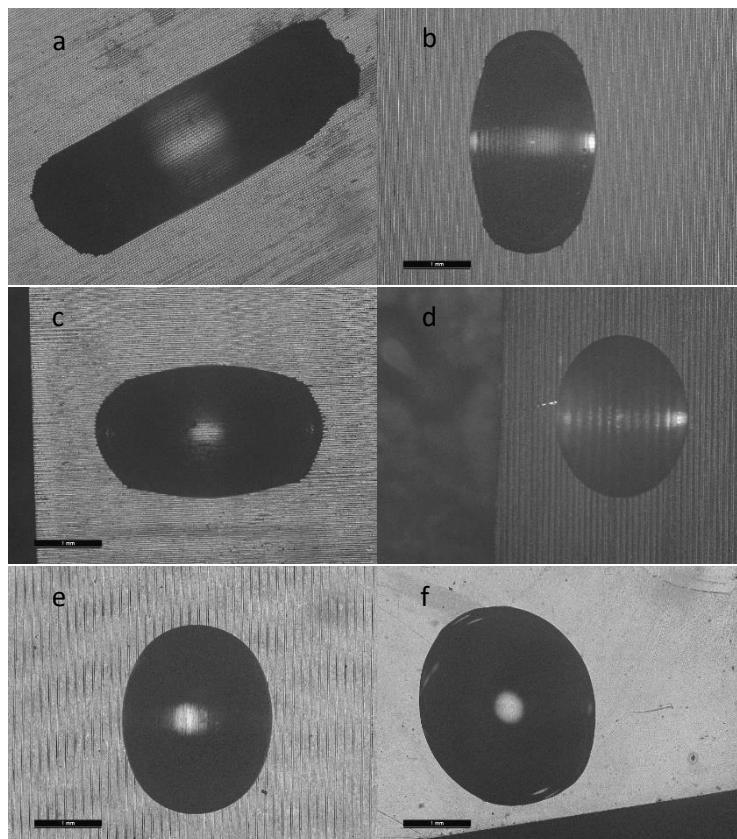


Fig. 4.10 The images of 5 μL droplets deposited on varied microgroove copper surfaces (a) 5-30, (b) 15-30, (c) 30-30, (d) 60-30, (e) 100-30 and (f) flat under the optical microscope.

The samples with droplets landing on the surfaces were observed under an optical microscope to gain a better view. The droplet was dispensed from a pipettor and placed on the sample surface from a distance as close as possible. The shape of the droplet stretching on the surface could be viewed from the top, as displayed in Fig. 4.10. The shape of the droplet on the flat copper surface is circular, which

is a natural result as it is initially dispersed from a syringe. On the grooved surface, the droplet extends along the groove direction and forms an ellipsoid. As the groove period increases, in other words, the solid fraction ratio increases, the extension of droplet along the groove direction was enhanced. This confirms that the surface becomes anisotropic in terms of wettability due to the directional groove geometries.

The zoom-in view of the copper surfaces was displayed in Fig 4.11. The way water contacts the copper micropatterns could be observed. The contact line was partially shadowed under the deformed water droplet due to the different contact angle from different directions of the groove surface. The water droplet could still be found to have penetrated the micropatterns where water was stretched by the copper surface and formed a thin film along the grooves. The penetration of water drop can also be viewed on the micropillar surface, as the gaps formed in the pillar array drew the initially round drop into a rectangular one.

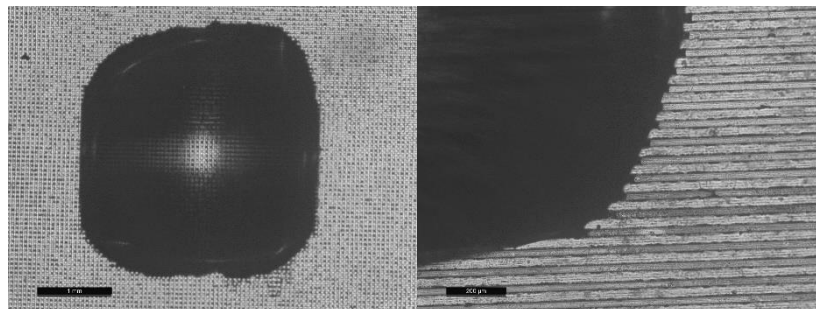


Fig. 4.11 The images of 5 μL droplets deposited on the micropillar copper surface and the 30-30 microgroove copper surface. The droplet shape changes with the distribution of micropatterns as water penetrates into the patterns.

Static contact angles were experimentally measured on the bare copper surfaces, copper microgrooves and coated copper surfaces to quantify the surface wettability, using sessile drop method on the goniometer. Each reported data is the average of three to five independent measurements in randomly selected areas. The dispersed droplet was deionized water of approximately 5 μ l.

The bare copper surface presented a contact angle of $86.0 \pm 1.0^\circ$ due to its intrinsic properties. This measured value is consistent with some previous reports (Y. Chen et al., 2009; T. Liu et al., 2007). According to the Wenzel mode, the copper microgroove surface presented in Fig. 4.10 possess roughness ratios ranging from 1.21 to 1.79. Theoretically calculated contact angles are from 82.8° to 85.1° regardless of the direction of the groove structure, while in practice the contact angles are far from the calculated values. The contact differs a lot from different directions. This indicates that the Wenzel mode describing the contact angle based on the air fraction ratio is not applicable on anisotropic surfaces with regular micropatterns, as the water adhesion to the copper structures would largely affect the droplet deformation.

The flat copper surfaces and the copper microgrooves were coated with Cu_2O and modified with stearic acid to gain hydrophobicity. The Cu_2O -STA coated flat copper surface presented a static contact angle of $142.2 \pm 1.2^\circ$. The Cu_2O -STA modified 15-30, 30-30, 60-30 and 100-30 microgroove surfaces presented the static contact angle of $143.5 \pm 3.6^\circ$, $143.2 \pm 1.6^\circ$, $143.6 \pm 1.5^\circ$, $147.2 \pm 1.2^\circ$ and $138.3 \pm 3.2^\circ$, respectively. The images showing the static contact angles are displayed in Fig. 4.12. The Cu_2O -STA coating showed significant increase in hydrophobicity compared with bare copper surface. This confirms the effect of the rough structures and low surface energy materials on the improvement of

hydrophobicity. Meanwhile, it is noted that there is no distinct difference in static contact angle among the Cu₂O-STA coated samples with different groove period of the base micropatterns. If the Cu₂O-STA follows the Cassie & Baxter model, according to a measured contact angle of 142.2° on the coated flat surface, the Cu₂O-STA coated microgroove surfaces would present static contact angles ranging from 146.8° to 165.8° based on the different air fraction resulting from the varied groove periods. This misfit indicates that the air layer formed at the interface of a droplet and the rough surface could not be tuned by the microgrooves in the dimension of tens of micrometers. Hydrophobicity of the prepared surfaces might be limited by the nature of Cu₂O-STA coating.

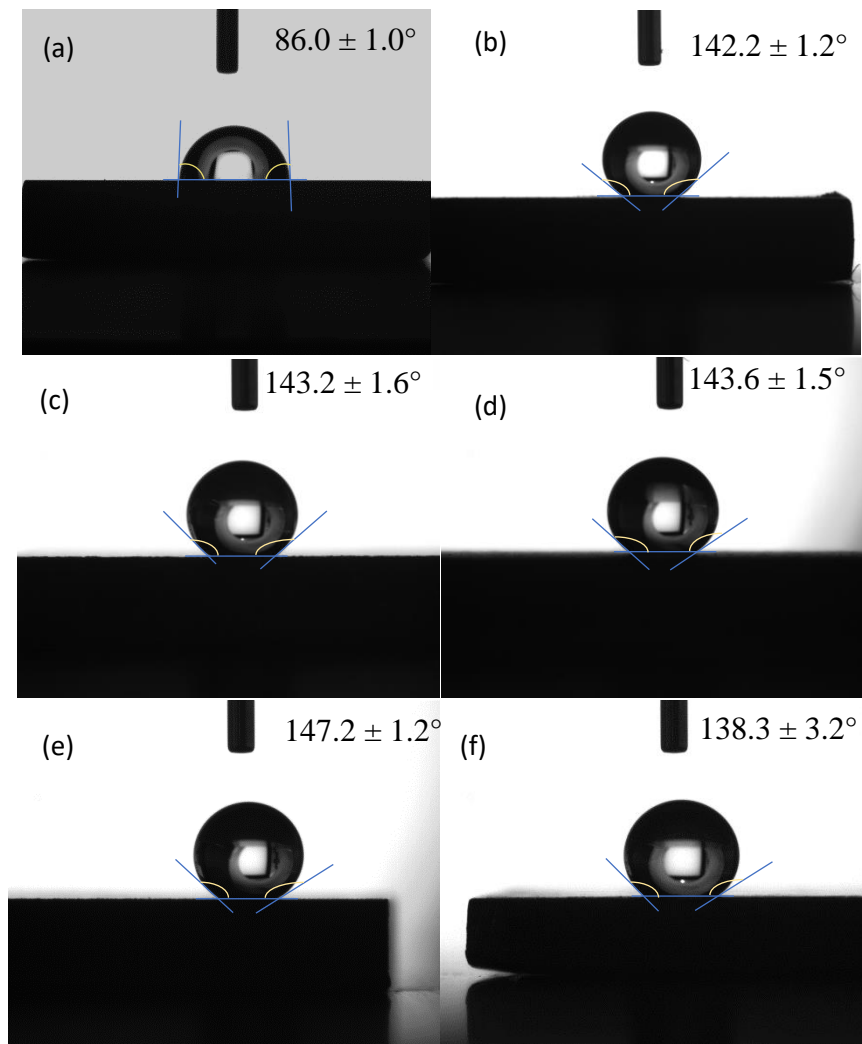


Fig. 4.12 Images of the static contact angle of (a) bare copper, Cu_2O -STA coated (b) flat copper plate, (c) 15-30 microgrooves, (d) 30-30 microgrooves, (e) 60-30 microgrooves and (f) 100-30 microgrooves.

To fabricate surfaces with better hydrophobicity and find the dependence of solid fraction ratio on the hierarchical structures, the NiO microspheres as the secondary structures were prepared and tested. Prior to NiO preparation, electroless deposition of Ni on copper substrate was carried out and a smooth nickel layer that fully covers the copper substrate was yielded. The reaction time was carefully controlled to ensure it is long enough for full coverage of the copper substrate. Moreover, long reaction time may result in rough, cracked and thick Ni

layer which would change the geometric properties of the originally smooth machined copper surface. Tested with the interferometer, this well-deposited nickel layer deposited on UPM fabricated copper surface presented a relatively low surface roughness of around 37 nm, as shown in Figure 4.13, while in comparison the hydrothermally prepared oxide coating would increase the surface roughness to 300-500 nm. The nickel coating presented a static contact angle of $99.7^\circ \pm 2.6^\circ$, as shown in Fig. 4.14, which was determined by the nature of the metal Ni rather than the influence of roughness.

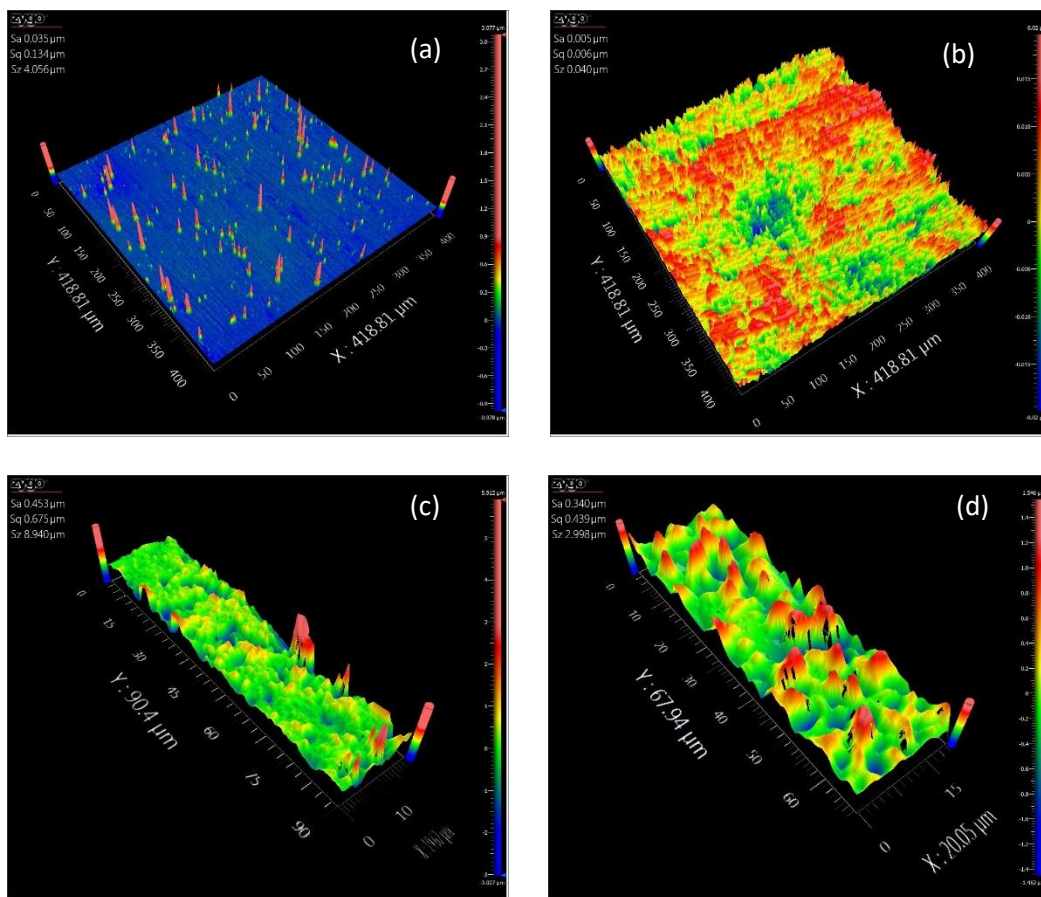


Fig. 4.13 The surface profile of (a) ELD prepared nickel layer on polished copper surface, (b) polished T2 copper, (c) Cu₂O coating and (d) NiO coating

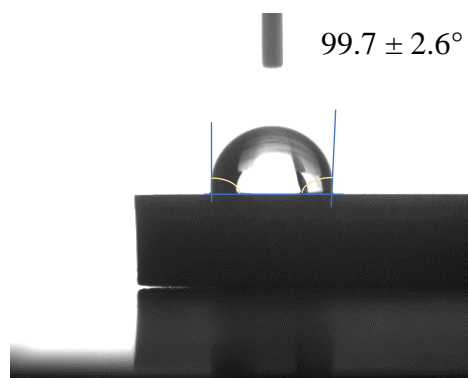


Fig. 4.14 Snapshots of the static contact angle of ELD prepared nickel coated flat copper surface

As nickel could be directly modified with FAS-17 and displays hydrophobicity, probably because of a thin oxide layer reacting with the siloxane, according to a previous report by Kang (Kang et al., 2012), such FAS-17 hydrophobic layer with low surface roughness could be prepared and meanwhile possess the same chemical composition on the surface as the NiO-FAS-17 microspheres. This would help study the individual effect of FAS-17 and the surface roughness on surface wettability.

The coating where FAS-17 was directly assembled onto the ELD prepared nickel layer was denoted as Ni-FAS-17. The Ni-FAS-17 coated flat copper presented a contact angle of $121.1^{\circ} \pm 1.6^{\circ}$, which was quite close to the theoretical value $-CF_3$ group can achieve. The static contact angle of the Ni-FAS-17 coated copper microgrooves was also evaluated. The anisotropic groove structure changed the shape of the water droplet and different contact angles can be observed from directions parallel to the grooves and orthogonal to the grooves. Ni-FAS-17 coated copper microgrooves presented a static contact angle of $144.9^{\circ} \pm$

0.3° viewed from the parallel direction. In the orthogonal direction the contact angle was only $127.0^\circ \pm 1.3^\circ$.

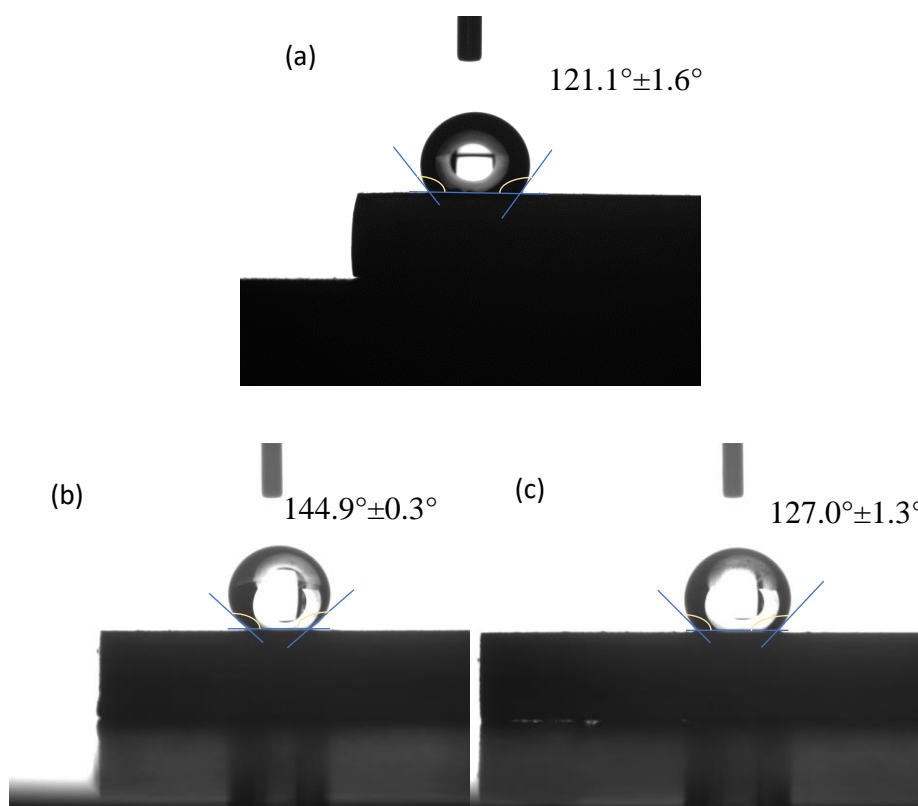


Fig. 4.15 Snapshots of the contact angle of Ni-FAS-17 coated (a) flat copper surface and grooved surface from (b) parallel direction and (c) orthogonal direction

In addition to static contact angle measurement, the dynamic wetting properties were tested to better study the prepared surfaces. The sliding angle and the advancing and receding angles were measured on the goniometer, and the contact angle hysteresis was calculated accordingly. For the bare copper, nickel coated copper and Cu_2O -STA coated surfaces, water droplets cannot slide or slide only when the sample stage is tilted at a very large angle. This reflects that the surfaces possess poor hydrophobicity in terms of dynamic properties. On the Ni-

FAS-17 coated flat surface, the droplet slide when tilted to about 27.3°. If the Ni-FAS-17 coating is formed on microgrooves, the surface would present different sliding angles in the parallel and orthogonal direction. The droplet slides parallel to the grooves at 13.4° and perpendicular to the grooves at 34.3°. The sliding angle in the orthogonal direction was even higher than on the flat surface. This indicates that the gaps formed by the grooves diminishes the adhesion by reducing the contact area. In the orthogonal direction, the grooves impede the movement of the water droplet.

Table 4.3 Wetting properties of different Ni coated surfaces

	Static contact angle, theoretical	Static contact angle, measured	Sliding properties
Nickel coated copper	-	99.7°±2.6°	Does not slide
Flat, Ni-FAS-17	-	121.1°±1.6°	Slides at 27.3°
Microgrooves, Ni-FAS-17, parallel	137°	141.0°±0.3°	Slides at 13.4°
Microgrooves, Ni-FAS-17, orthogonal		127.4°±1.3°	Slides at 34.3°

The NiO layer was prepared on Ni deposited flat copper surface and copper microgrooves. The NiO coating was intrinsically hydrophilic before it is modified with FAS-17. When a water droplet contacted the surface, it spread flat instantaneously. After modification of FAS-17, the acquired superhydrophobic layer was denoted as NiO-FAS-17 in this research. Its static contact angle was found very difficult to measure on the current setup. The NiO-FAS-17 coating was very water-repellent that its absorbance of the water droplet cannot overcome the drag force from the needle. When the droplet was large enough to automatically

fall from the needle, it would also slide off the NiO-FAS-17 coated surface immediately after its impact, even if it is released from very close to the sample surface, as the sample surface could not be tuned to perfectly spirit level. Therefore, measuring either the static contact angle or the sliding angle became unfeasible.

Table 4.4 Dynamic wetting properties of NiO-FAS-17 coated surfaces

	Advancing contact angle	Receding contact angle	Contact angle hysteresis
NiO-FAS-17, flat	$163.2 \pm 2.3^\circ$	$158.5 \pm 1.3^\circ$	$4.7 \pm 2.8^\circ$
NiO-FAS-17, microgrooves, parallel	$161.7 \pm 3.3^\circ$	$158.0 \pm 2.2^\circ$	$3.7 \pm 1.2^\circ$
NiO-FAS-17, microgrooves, orthogonal	$162.3 \pm 1.9^\circ$	$159.0 \pm 1.3^\circ$	$3.3 \pm 1.7^\circ$

The advancing and receding contact angles were measured in place of the static contact angle to evaluate the wetting properties of the NiO-FAS-17 coated superhydrophobic surfaces. In this process, the droplets were dispensed and withdrawn from a needle by a syringe on the sample surface. The tested results are presented in Table 4.4. The snapshots of the droplet expanding or shrinking on the surfaces were presented in Fig. 4.16.

The advancing and receding CAs of the NiO-FAS-17 coated flat copper surface are $163.2^\circ \pm 2.3^\circ$ and $158.5^\circ \pm 1.3^\circ$, respectively. The CAH was calculated to be $4.7^\circ \pm 2.8^\circ$ accordingly. For the NiO-FAS-17 coated microgroove surface, the three values are $161.7^\circ \pm 3.3^\circ$, $158.0^\circ \pm 2.2^\circ$ and $3.7^\circ \pm 1.2^\circ$ when observed from the parallel direction. Observed from the orthogonal direction the advancing

and receding angles were $162.3^\circ \pm 1.9^\circ$ and $159.0^\circ \pm 1.3^\circ$ and the CAH was $3.3^\circ \pm 1.7^\circ$. We can conclude from the tested results that the microgroove structure is beneficial for improving the hydrophobicity of the surface, as the CA is significantly larger compared with the Ni-FAS-17 modified microgrooves and flat surfaces.

The effect of introduction of rough NiO nanostructure is also reflected on the anisotropy. The Ni-FAS-17 modified microgrooves also displayed clear anisotropy as the droplet was deformed along the groove direction, which was similar to the cases on bare copper microgrooves. However, the anisotropy in terms of contact angles were diminished on NiO-FAS-17 coated surfaces despite the anisotropy in surface geometry of the coated microgrooves. The droplets were in good circular shape and the CA values viewed from different directions are very close to each other. This is probably due to good water repellency of the nanostructured surfaces. The adhesion of water was minimized to a small value that the difference from different directions became very small.

The results also showed that the dynamic wetting properties of the NiO-FAS-17 coated flat surfaces are approximately the same as the grooved surfaces. This indicates that the introduction of microgroove structures did not play an important role in improving hydrophobicity. The case in NiO-FAS-17 coating is the same as the Cu₂O-STA coating as in both cases the secondary micro-nano structures were deposited to form a hierarchical structure and no distinct difference was discovered in the static and dynamic contact angles. The secondary micro-nano structures of Cu₂O-STA or NiO-FAS-17 were dominant in increasing the CA to around 140° and 160° , respectively. The NiO micro-nanostructured layer provided more vertically aligned morphology than the rectangular-shaped Cu₂O

crystals, which explains why the NiO based surfaces achieved better hydrophobicity.

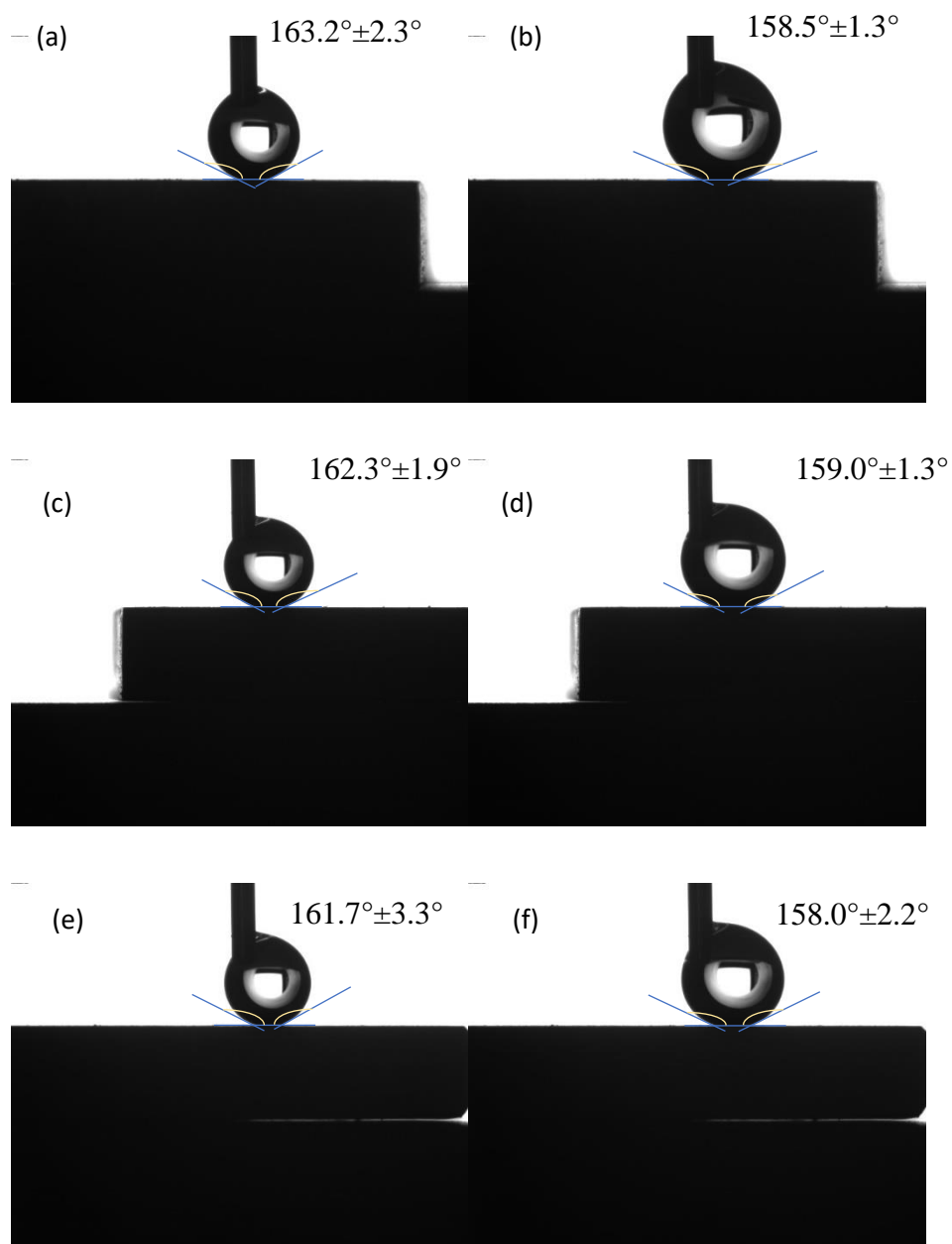


Fig. 4.16 Snapshots of the advancing contact angle of NiO-FAS-17 coated (a) flat surface, (c) grooved surface from the orthogonal direction and (e) the parallel direction, and the receding angle of NiO-

FAS-17 coated (b) flat surface, (d) grooved surface from the orthogonal direction and (f) the parallel direction

4.4 Concluding remarks

In this chapter, the superhydrophobic micro/nano-structured surfaces were fabricated by integrating UPM of microgrooves and hydrothermal synthesis of Cu_2O and NiO micro/nanostructures. The topography of the prepared surfaces was examined and the surface wettability was evaluated. Hierarchical structured surface based on modified copper microgrooves with good superhydrophobicity were acquired.

Rectangular shaped Cu_2O crystals were prepared on copper substrates, followed by the spontaneous absorption of stearic acid to form a hydrophobic surface. The Cu_2O -STA coating improved the hydrophobicity considering the intrinsic poor water repellency of copper, while no distinct differences in wettability were revealed among flat base samples and groove base samples of different groove period.

NiO nanoflakes were prepared to acquire the morphology which was comparatively favored for building a hydrophobic layer. The NiO -FAS-17 modified copper microgrooves presented superhydrophobicity with large contact angles and small contact angle hysteresis, which is a lot better than the hydrophobic Cu_2O -STA coated surfaces. In terms of contact angles and contact angle hysteresis, still no distinct differences could be discovered among the NiO -FAS-17 coated surfaces with copper substrates of varied surface geometry.

The anisotropy of the microgroove surfaces in terms of surface wettability was also investigated. As the copper microgrooves as the base of the hierarchical superhydrophobic surfaces possess anisotropy in terms of geometry, bare copper microgrooves presented clear anisotropy in terms of wettability. The water droplet deposited on the groove surfaces stretched along the groove direction, and the extent it stretched increase as the air fraction ratio of the groove surface became larger.

When coated with either Cu_2O -STA or NiO-FAS-17 layer, the surface became hydrophobic. The NiO based superhydrophobic surface performed better hydrophobicity than the Cu_2O based samples. The superior hydrophobicity of NiO-FAS-17 coated surfaces was reflected not only in the contact angle but also in the small CAH, compared with a water-adhesive surface of Cu_2O -STA samples.

The introduction of microgrooves into the Cu_2O -STA or NiO-FAS-17 coated samples does not increase the CA or CAH of the hydrophobic surfaces, indicating a dominant influence of the rough oxide coating on the surface wettability. The difference induced by the UPM fabricated micropatterns might be reflected in other applications of superhydrophobic surfaces and would be studied in next few chapters.

Chapter 5 Hydrophobic corrosion resistance of micro/nano-structured surfaces

5.1 Introduction

Copper is one of the most important fundamental materials and widely utilized in many industrial fields such as electronics, aviation, automobile and ship building, owing to its superior electrical and thermal conductivity, mechanical workability and malleability (T. Liu et al., 2007; Yan Liu et al., 2015). However, copper is prone to corrosion especially in an aggressive medium, which causes a compromised service lifespan (Sinapi et al., 2008). This poses a threat to the industry economy and has been attracting researchers' interest to work on strategies for an inhibition of corrosion.

As corrosion reactions are triggered by the contact of solid surface and water with aggressive anions, the reduction of the contact area is effective on retarding the corrosion rate. Hydrophobic surfaces were believed to be effective on corrosion resistance for engineering materials (Y. Huang, Sarkar, Gallant, & Chen, 2013; P. Wang, Zhang, & Qiu, 2012). Many techniques are applied to prepare such surfaces, as well as the varied methods for characterization and analysis (Emelyanenko et al., 2018; Fan, Chen, Liang, Wang, & Chen, 2014; Trdan et al., 2017; Wan et al., 2018; Zhaozhu Zhang, Ge, Men, & Li, 2016).

It is noted that most of the fabricated hydrophobic surfaces thus far were based on irregular coatings resulting in roughness and do not possess precise control on dimensions and shapes. Only limited works reported that regularly shaped hydrophobic microstructure were fabricated using milling technique, but it

did not provide adequate results to study the underlying mechanism of corrosion resistance associated with surface topography (Zhu & Hu, 2018). Hierarchical structures could be fabricated through machining of controlled microstructures followed by modifications with secondary structures and were effective in increasing hydrophobicity, which is a promising way to hence improve the corrosion resistance properties (C. Lee, Choi, & Kim, 2016).

Ultraprecision machining (UPM) is a method that provides a feasible solution to the precise fabrication of micro-patterned surfaces (Z. Zhang et al., 2019). In a UPM process, a diamond tool could incorporate up to five controlled axes, which provides more degrees of freedom than other mechanical and chemical processes (Davies et al., 2003; S. Zhang et al., 2019). Therefore, it is applicable for machining a variety of geometries and replicating them into microarrays. There are some typical structures such as micropylamids (Ge et al., 2018), microgrooves (C. T. Cheng et al., 2016), freeform compound-eye microlens array (Lei Li & Allen, 2012), rotational microridges (Likai Li & Allen, 2011) and micro conical array (Ang et al., 2019), which are utilized in fields including optics, energy and resources. On the other hand, hydrothermal synthesis is an efficient method in creating thin films with micro-nanostructured topography (Mali, Betty, Bhosale, Patil, & Hong, 2014; Q. Zhang et al., 2014). It is a chemical process performed in an aqueous solution in a sealed vessel above ambient pressure and temperature. The high pressure and temperature facilitates the interactions of the reactants and single crystalline products are obtained (Nikam, Prasad, & Kulkarni, 2018). Depending on the precursors and additives, varied micro-nanostructures could be prepared such as nanorods (Ridhuan, Razak, & Lockman, 2018), nanospheres (P. Ou et al., 2019) and nanoflakes (Thirumalai, Shanthi, &

Swaminathan, 2019). To achieve a hydrophobic surface, the fabrication of metal oxides through hydrothermal synthesis is always followed by treatment of chemicals with low surface energy groups. This procedure produces a thin layer of organics with low surface energy onto the oxides while retaining the prepared micro-nanostructures (Chantal, Thierry, Mireille, & Daniel, 2007; Fan et al., 2014; Xiao et al., 2015).

The study described in this chapter aims at enhancing the corrosion resistance of copper by applying a new method that integrates UPM with hydrothermal synthesis to fabricate rectangular shaped cuprous oxide on copper plates with machined microgrooves. The shape of the groove gaps could be precisely controlled in the UPM process. The prepared Cu_2O surface was modified with stearic acid (STA) to achieve a low surface energy. The Cu_2O -STA modified with grooved copper was measured through morphological characterization and electrochemical characterization for displaying the corrosion resistance behavior.

5.2 Experimental details

The samples prepared for investigation on corrosion resistance were fabricated by coating on small copper plates. The copper plates were T2 copper purchased from Quanfu Metal Co. (Shenzhen, China). The whole fabrication process for the hierarchical Cu_2O -STA modified copper microgrooves and the fabrication parameters were the same as stated in Chapter 3 & 4. The plates were firstly cut into the dimensions of 10 mm in length, 10 mm in width and 2 mm in thickness. Then ultraprecision machining was carried out to obtain the microgroove copper surface on a Moore Nanotech 350FG machine. The UPM

fabricated microgroove surface was subsequently coated with rectangular shaped cuprous oxide crystals through a hydrothermal process. The schematic diagram to show the process is displayed in Fig. 5.1.

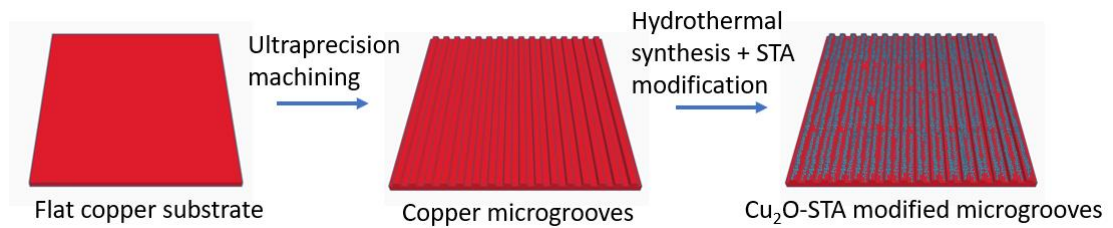


Fig. 5.1 The schematic diagram of the fabrication of the hierarchical Cu_2O -STA modified microgroove surface

The geometry of the fabricated copper microgrooves was shown in Fig. 5.2. A single crystal diamond cutting tool with specific included angle and width of tool tip was selected to fabricate the microgrooves. The target groove shape was presented in the schematic diagram Fig.1(a) and (b). Trapezoidal grooves with $30\ \mu\text{m}$ in width and $18\ \mu\text{m}$ in depth were fabricated. The angle of the slope was 75° , determined by the included angle of the diamond tool tip. The step of the workpiece along x axis was $60\ \mu\text{m}$, producing grates of $30\ \mu\text{m}$ in width.

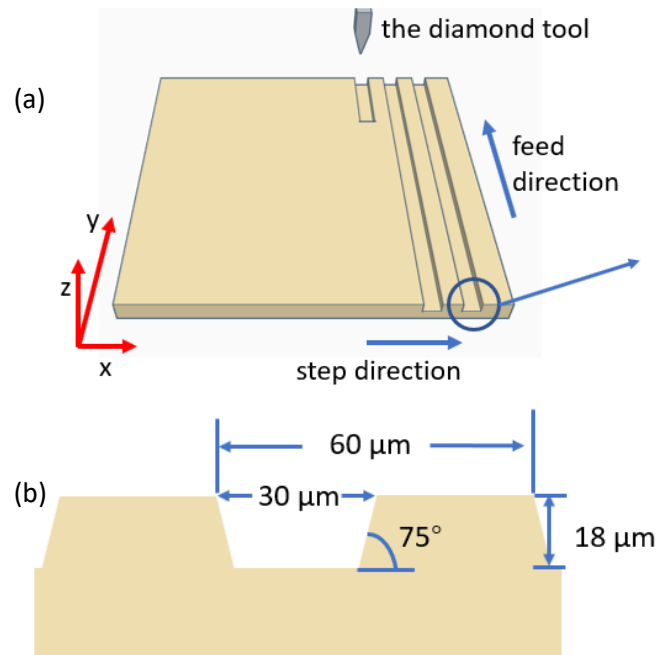


Fig. 5.2 (a) the schematic diagram of microgrooves surface generation and (b) the cross-section view of the trapezoidal grooves

The examination of the profile of the microgrooves, the morphology and composition of the Cu_2O layer has been introduced in Chapter 4 and will not be further stated here. The corrosion experiments were performed using CHI660e electrochemical workstation (Shanghai Chenhua Instrument Co., China) with the electrolyte of 3.5 wt.% aqueous NaCl solution in all cases. The anticorrosion behavior of the Cu_2O -STA modified copper microgrooves was investigated by the measurements of electrochemical impedance spectra (EIS) and Tafel polarization. A conventional three-electrode system was used with a saturated Ag/AgCl electrode as the reference electrode and two symmetrically distributed carbon stick electrodes as the counter electrode. The EIS curves were obtained at the open circuit potential using a 10 mV amplitude sinusoidal signal in the frequency range

of 10^5 to 10^{-2} Hz. The Tafel curves were obtained at a scan rate of 0.5 mV/s in the range of about ± 300 mV vs. open circuit potential.

5.3 Results and discussion

5.3.1 Characterization of the Cu₂O-STA microgrooves

The fabricated microgrooves in this research were the 30-30 copper microgrooves, which has been described in Chapter 4. The depth of the grooves is designed to be 18 μm and the top width of grooves is 30 μm . The period of the groove structure is 60 μm . The surface becomes rough after the modification with Cu₂O-STA, as shown in Fig. 5.3.

The morphologies of the fabricated Cu₂O were examined by SEM, as shown in Fig. 5.3. In Fig. 5.3(a), the copper microgrooves fabricated by UPM were displayed. The surface is quite smooth and there are no large defects in groove shape. In Fig. 5.3(b) and (c), rectangular-shaped Cu₂O particles were formed with an average grain size of about 1 μm . The oxide crystals were distributed uniformly and covered almost the whole surface. The groove shape fully covered with cuprous oxide could also be clearly viewed. The shape of the Cu₂O particles is associated with the concentration of the copper salt in the hydrothermal bath. As the oxide layer cannot be so thick that the original shape of the groove base might be changed, a relatively small concentration was applied. It was corresponding to a rectangular shape rather than an octahedra, with an empirical criterion of 50 mM (Al-Ghamdi, Al-Hazmi, Al-Hartomy, El-Tantawy, & Yakuphanoglu, 2012; Xu, Wang, & Zhu, 2006).

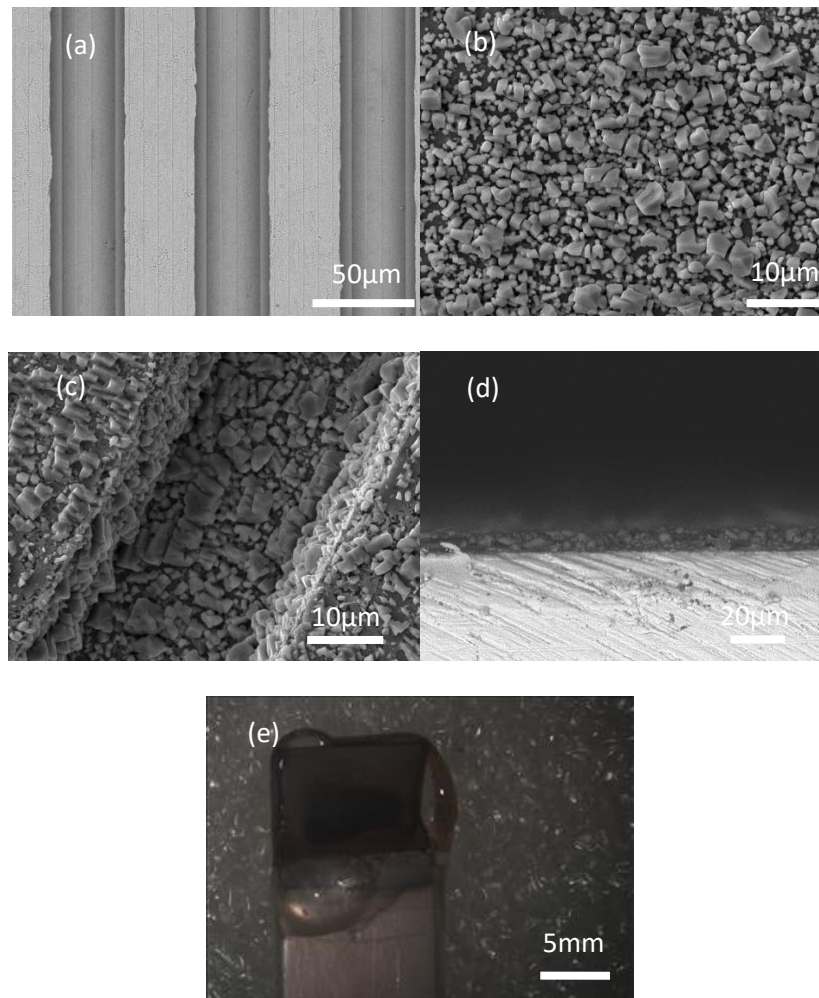


Fig. 5.3 SEM images of (a) copper microgrooves fabricated by UPM, Cu₂O-STA film on (b) flat copper plate and (c) copper microgrooves, cross-section view of Cu₂O-STA film and (e) a photo of a sealed sample

The Cu₂O film was chemically modified with stearic acid to improve the hydrophobicity. Wettability of the surface was measured by testing the contact angle of water droplets (5 μL). The obtained value is an average measured at 3~5 different positions on the same sample. The contact angle of carefully polished

care copper was around 86° . For the Cu_2O -STA modified copper microgrooves, the contact angle increased to 144° . This reflected the hydrophobicity of the fabricated hierarchical structured surface. When immersed in water, hydrophobic surfaces were exceptionally bright when viewed in an oblique angle. The width of a single groove of the hierarchical Cu_2O -STA modified microgroove hydrophobic surface was about $30\ \mu\text{m}$, and therefore it was enabled to be observed through an optical microscope when it was immersed in water, as displayed in Fig. 5.4(c). The periodically distributed bright lines were air trapped in microgrooves. According to the Laplace-Young equation, a small groove width and a large groove depth are effective on maintaining the air layer (C.-H. Choi et al., 2006). Cu_2O -STA coatings were tested on flat copper plates and copper microgrooves. On flat surfaces the contact angle was measured to be $142.2 \pm 1.2^\circ$. On grooved samples the contact angles observed from two directions did not differ a lot and presented a value of $143.6 \pm 1.5^\circ$.

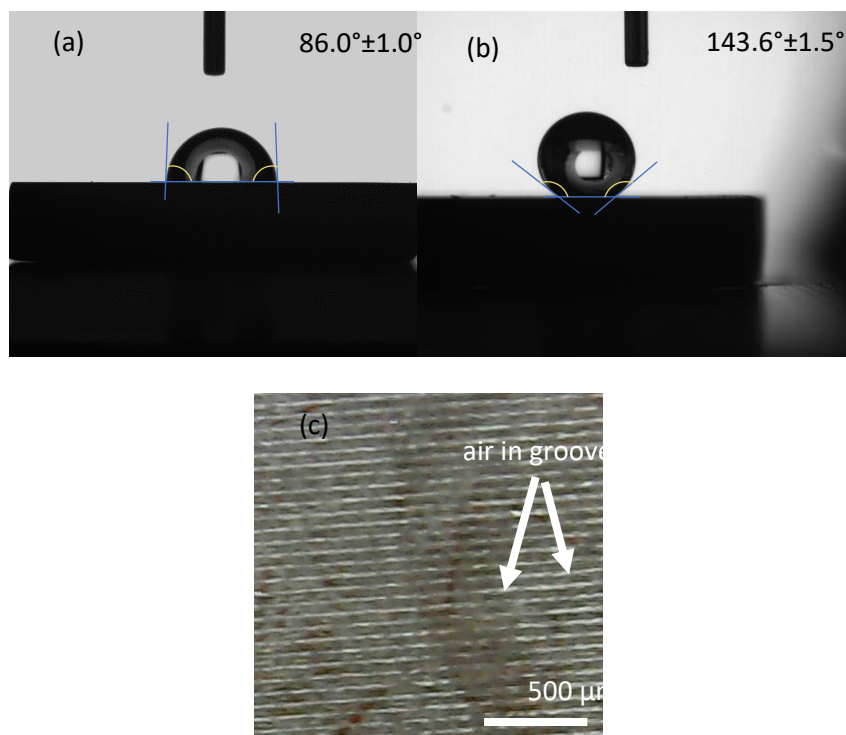


Fig. 5.4 The contact angles of (a) flat copper plate and (b) Cu₂O-STA film on copper microgrooves and (c) the air layer of Cu₂O-STA film on copper microgrooves immersed in water

5.3.2 Corrosion behaviors of the Cu₂O-STA microgrooves

EIS is a nondestructive technique to characterize the electrochemical reactions and subprocesses occurring at electrode-electrolyte interfaces. It could provide important information regarding the corrosion reaction mechanisms (Fan et al., 2014). Fig.7 shows Nyquist plots and Bode modulus plots of the bare copper, bare copper grooves and the surface modified Cu samples. The EIS data could be analyzed by the ZView2 program with an appropriate equivalent electrical circuit (EEC). As bare metal and metal with a hydrophobic coating were physicochemically different, two circuit models were applied to fit the EIS spectra. The two EEC models are displayed in Fig.8. In the circuits, R_s was equivalent to

the solution resistance and R_{ct} was the charge transfer resistance. R_{ct} was indicative of total corrosion resistance performance. CPE was often used as a substitute for the capacitor in an equivalent circuit to better fit the behavior of electrical double layer. In Fig. 8(b), R_c was introduced due to the existence of the hydrophobic layer. The R_{ct}/C_{dl} elements showed the interface reaction on the Cu_2O -STA film.

The corrosion resistance could be judged qualitatively from the diameter of the Nyquist semicircles, as shown in Fig. 7(a). In general, an increase of the diameter implies a rise of corrosion resistance. The diameter of the Nyquist loop for Cu_2O -STA modified samples was significantly larger than that of a bare copper. For the Cu_2O -STA modified grooved copper, it was also larger than that of the modified flat copper. The results indicate that the presented Cu_2O -STA layer contributes to good corrosion resistance and that the Cu_2O -STA layer on microgrooves presented even better corrosion resistance. This was owing to the hydrophobic oxide layer as the corrosion inhibitor, and the air trapped in the microgrooves further improved the performance, which reduced the contact of the sample and the electrolyte (Mohamed, Abdullah, & Younan, 2015). Bare copper microgrooves were more prone to corrosion according to the EIS spectra as the corrosive medium would penetrate the grooves instead of forming an air layer, which enlarged the contact area of the copper surface and the electrolyte. The fitted data by using ZView2 program are presented in Table 1. The R_{ct} of Cu_2O -STA modified flat copper was remarkably larger than bare copper, and it became approximately double the value when Cu_2O -STA was coated on the microgrooves to form a hierarchical structure. The Bode modulus at the lowest frequency was also used to estimate the corrosion activity. A large impedance modulus was indicative of good anticorrosion capability. As in Fig.7(b), the Bode plots showed

an increase of corrosion resistance from the bare copper microgrooves to Cu_2O -STA coated on grooved copper.

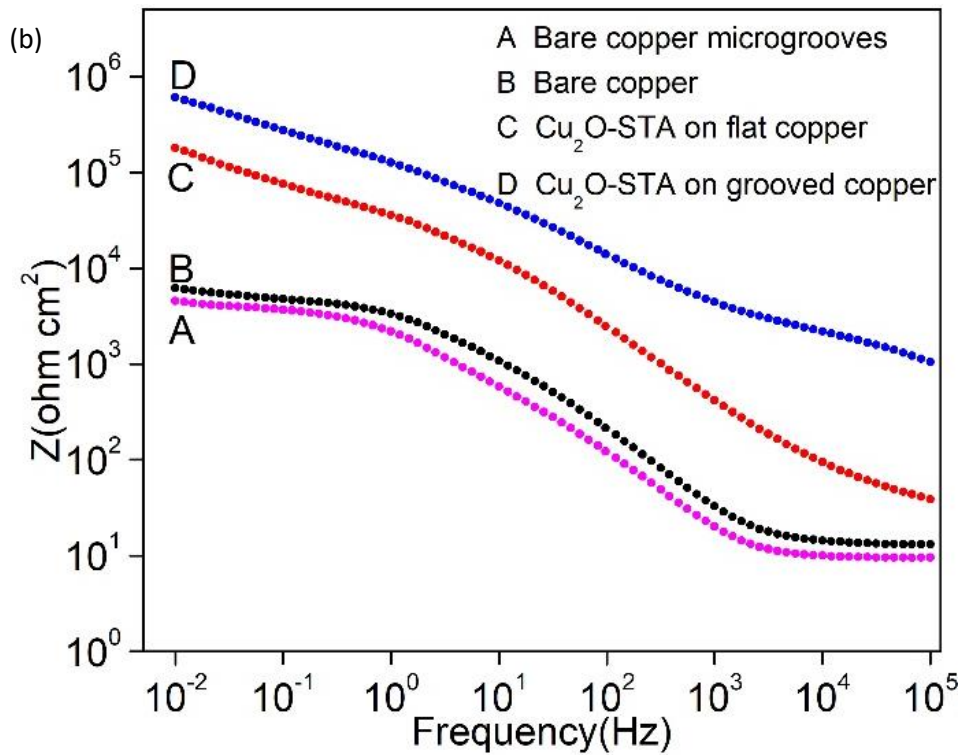
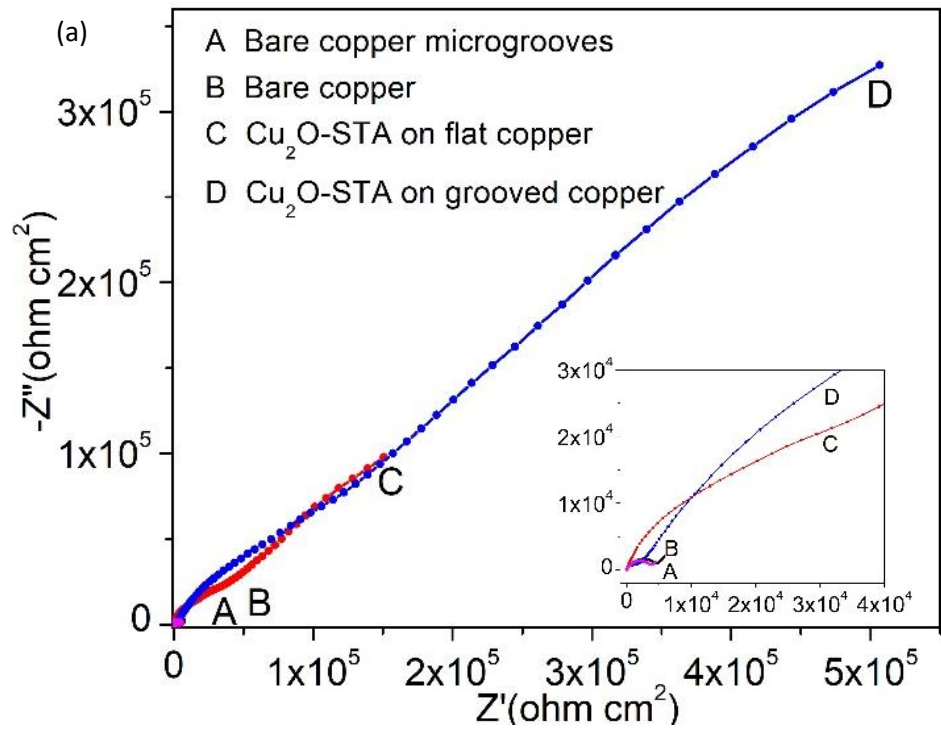


Fig. 5.5 Nyquist (a) and Bode (b) plots of the bare Cu, Cu₂O-STA modified flat copper and Cu₂O-STA modified grooved copper. The inset of Nyquist plots is the amplification of the high frequency part

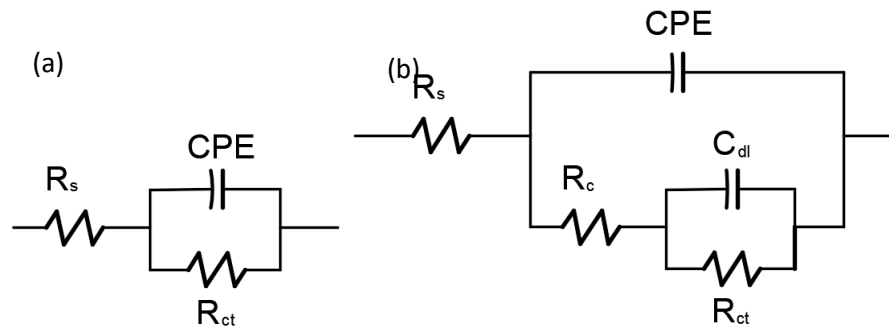


Fig. 5.6 The equivalent electric circuits for modeling the EIS spectra of (a) bare copper, bare copper microgrooves, (b) the Cu₂O-STA modified flat copper and grooved copper with 3.5 wt.% NaCl solution as the electrolyte

Table 5.1 Fitted parameters of EIS spectra

Samples	R_s ($\Omega \cdot \text{cm}^2$)	CPE ($\mu\text{F} \cdot \text{cm}^{-2}$)	R_c ($\Omega \cdot \text{cm}^2$)	C_{dl} ($\mu\text{F} \cdot \text{cm}^{-2}$)	R_{ct} ($\Omega \cdot \text{cm}^2$)
Bare copper	8.32	26.2	-	-	5.79×10^3
Bare copper microgrooves	9.35	0.91	-	-	4.30×10^3
Cu ₂ O-STA on flat copper	40.4	1.06	3.14×10^4	1.05	6.89×10^5
Cu ₂ O-STA on grooved copper	605	1.13	3.78×10^5	1.81	1.56×10^6

Tafel plots have been widely used to monitor the instantaneous corrosion rate of metals, alloys and surfaces with coatings, inhibitors or bacteria (Shumakovich et al., 2014). In this study, the bare copper and surface-modified

copper samples were tested using this technique to evaluate the anticorrosion behaviors. Fig. 9 shows the Tafel plots of the bare copper, bare copper microgrooves, Cu₂O-STA modified flat copper and Cu₂O-STA modified grooved copper. The Tafel plots were analyzed by extrapolating the linear anodic and cathodic branches to their intersection to obtain some featuring indexes including corrosion current densities and corrosion potentials. The corrosion current density directly reflected the speed of corrosion reaction. As stated in Table 2, for the Cu₂O-STA modified flat sample, the corrosion current density was 0.569 $\mu\text{A}\cdot\text{cm}^{-2}$, showing a decrease from 1.69 $\mu\text{A}\cdot\text{cm}^{-2}$ for the bare Cu. This confirmed the anticorrosion property of the Cu₂O-STA modification layer. The Cu₂O-STA modified microgrooves showed an even smaller corrosion current of 0.239 $\mu\text{A}\cdot\text{cm}^{-2}$, which was reduced more than half of the modified flat sample. The results were in good consistence with the EIS spectra, showing good corrosion resistance of the Cu₂O-STA layer and the enhancement of the hierarchical structure. The air trapped in grooves reduced the electroactive area of the samples and thus the corrosion current. Considering that the Cu₂O-STA samples possess same chemical composition, the introduction of microgrooves plays the key role in the enhancement on corrosion resistance of the hierarchical structures, which was reflected in the aforementioned electrochemical tests for the impedance and the corrosion rate.

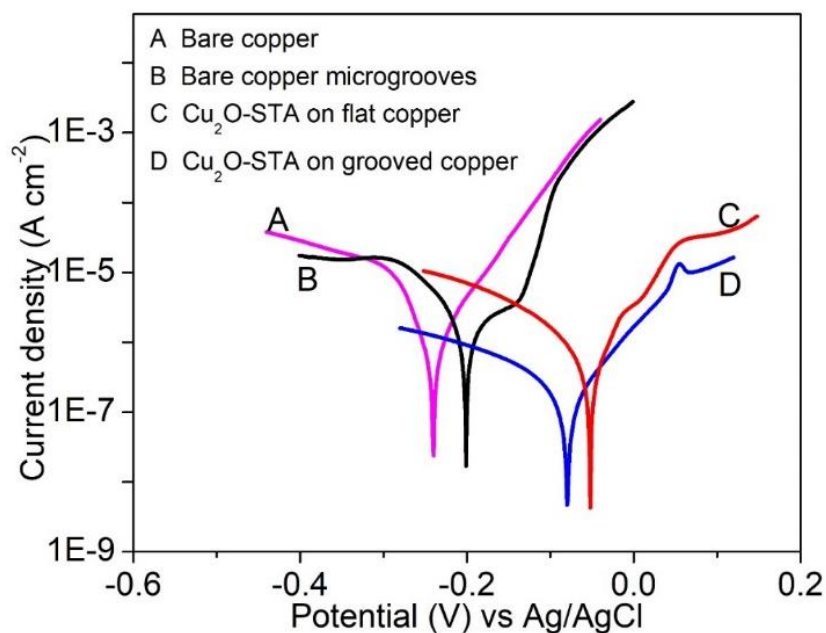


Fig. 5.7 Potentiodynamic polarization curves in 3.5 wt.% NaCl solution.

Table 5.2 Electrochemical parameters from polarization curves of different samples

Samples	E_{corr}/V	$I_{\text{corr}}/\mu\text{A}\cdot\text{cm}^{-2}$
Bare copper	-0.215	1.85
Bare copper microgrooves	-0.195	4.33
Cu_2O -STA on flat copper	-0.048	0.629
Cu_2O -STA on grooved copper	-0.073	0.176

To investigate the long-term durability of the corrosion resistance coating, Tafel polarization measurements were carried out after immersion in 3.5 wt.% NaCl solution at room temperature for 7 days and 14 days. The curves are presented in Fig. 5.9 and the calculated results of corrosion potential and corrosion current density are presented in Table 5.3. The corrosion current of all the four samples are lower than the freshly prepared samples, indicating a decrease of the

corrosion resistance of the samples after long-time immersion. The same situation goes for the samples immersed for 14 days compared with the samples immersed for 7 days, indicating a worse anticorrosion property as the immersion was lengthened. This is natural as the hydrophobic coating was corroded by the solution as time passed. The samples still showed some corrosion resistance as the current density values are significantly smaller than bare samples, reflecting that the hydrophobic coating did not become completely invalid after 14-day immersion.

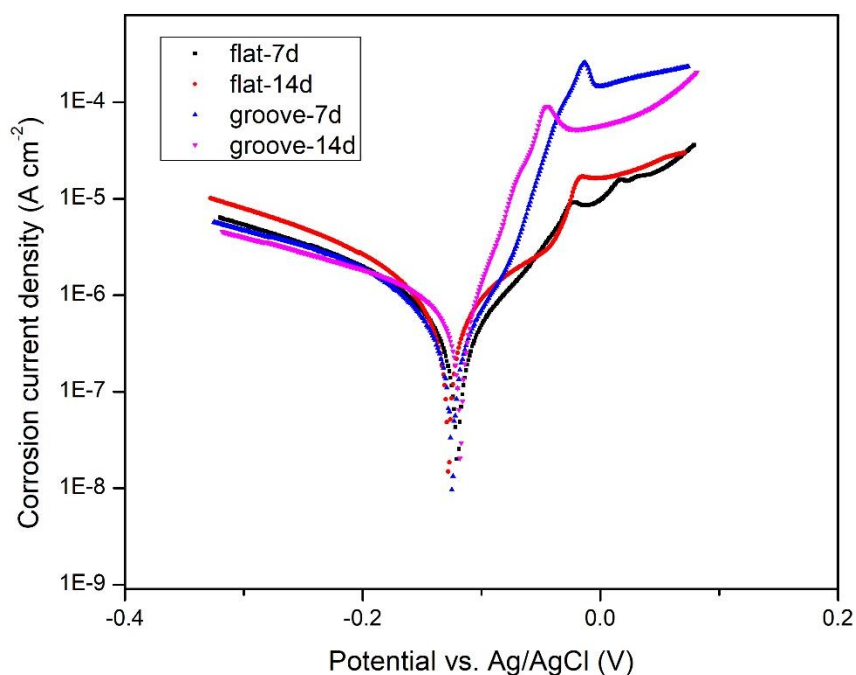


Fig. 5.8 Potentiodynamic polarization curves in 3.5 wt.% NaCl solution of samples after 7 days or 14 days immersion in 3.5% NaCl aqueous solution.

Table 5.3 Electrochemical parameters from polarization curves of different samples

Samples	E_{corr}/V	$I_{\text{corr}}/\mu\text{A}\cdot\text{cm}^{-2}$
Flat-7d	-0.12	0.693
Flat-14d	-0.128	1.001
Groove-7d	-0.125	0.768
Groove-14d	-0.118	0.863

5.4 Concluding remarks

Cu_2O -STA modified hierarchical hydrophobic structures were fabricated on copper by combining UPM with hydrothermal synthesis for its corrosion resistance. Rectangular shaped cuprous oxide crystals were hydrothermally prepared on UPM fabricated microgrooves. According to the electrochemical measurements, the hydrophobic Cu_2O -STA film showed good corrosion resistance. When microgrooves were introduced, the performance was further improved with the corrosion rate reduced by half. The geometries could be controlled through the UPM process to better form an air layer as the corrosion inhibitor, and simultaneously, the rough cuprous oxide layer is successfully formed on the microgroove surface. Long-term stability of the Cu_2O -STA coated samples were also tested for the corrosion resistance. A decrease in corrosion resistance performance was recorded while there is still some anticorrosion effect after 14 days immersion in NaCl solution, according to the calculated results of current corrosion density. The method proposed in this study provides a feasible option to fabricate hydrophobic anticorrosion surface and systematically investigate the topography influence on corrosion resistance. The corrosion-resistant surface could meet the need in industry fields such as automobile, ship

building and electronics. It could be applied on critical components on a wide variety of mechanical devices.

Chapter 6 Water droplet bouncing behaviors on superhydrophobic micro/nano-structured surfaces

6.1 Introduction

The method based on the ability to bounce of a water droplet is applied to evaluate the wettability of the prepared superhydrophobic micro/nano-structured surfaces. A water droplet will bounce back instead of getting stuck when it falls onto the surface with good hydrophobicity. The bouncing characteristics are believed to be related to the surface wettability qualitatively and quantitatively. Water droplet bouncing experiments provide information on the movement of droplets under tunable droplet size and dropping height, yielding properties including the number of bouncing, the height of bouncing, the spreading factor, etc. to describe the wettability of the sample surfaces.

The static CA and CAH are essential properties for a superhydrophobic surface as stated in previous chapters (B.-B. Wang et al., 2011). Studies on water droplet impact, or in other words, the droplet bouncing behaviors have also drawn much attention as it is an important way to characterize the hydrophobicity for extremely water repellent surfaces. The tests of water droplet bouncing behaviors were proposed to be an indication of the hydrophobicity of the substrate surface where the droplets impact in the beginning of the decade. This way to evaluate surface hydrophobicity could incorporate the fundamental hydrophobicity (indication of contact angle), ability to prevent penetration of surface protrusions

(wetting mechanism, advancing and receding angle) and dynamic interaction with the surface (water pinning and self-cleaning) (C. R. Crick & Parkin, 2011).

The bouncing behaviours are associated with the original kinetic properties of the water droplet. The Weber number is a dimensionless number that indicates the ratio of drag force to cohesion force. The expression of the Weber number is

$$We = \frac{\rho v^2 l}{\sigma}$$

In this equation, ρ is the water density and v is the droplet velocity. The character length l is typically the droplet diameter. The surface tension σ is the value of water against air $\gamma_{LV} = 72$ mN/m. Weber number is used as the governing parameter to analyse the water droplet bouncing behaviours.

In this research we perform drop impact experiments on the NiO-FAS-17 based superhydrophobic substrates. The NiO-FAS-17 coating was prepared on different base structures including flat copper surface and microgroove surfaces. Bare copper with microstructures and hydrophobic Ni-FAS-17 coating without rough oxides are also tested and serve as reference. The bouncing procedure of the droplets was recorded against the governing parameter We , which can be tuned through the releasing height and the volume of the droplet. By measuring the properties of the bouncing droplets including rebound height and deformation and discussing from the perspective of energy dissipation, the hydrophobicity of different substrates can be concluded, and the effect of the micro-nano structures can be analysed.

6.2 Experimental details

In this section the apparatus for the recording of the dynamic behaviours of the water droplets were described. The hydrophobic samples where the droplets rebound were NiO-FAS-17 coated UPM fabricated microstructured surfaces. They were fabricated the same way as stated in Chapter 4 and will not be described again here.

The schematic diagram of the apparatus for recording the droplet bouncing movement is shown in Fig. 6.1. Hydrophobic samples are placed on a displacement instrument on an optical platform to ensure a spirit level. The displacement instrument can be tuned up and down to reach the designed dropping height. The needle to be placed above the sample was held using an iron stand and carefully adjusted upright. The needle was connected to a 1mL syringe, which was driven by an NE-4000 two channel syringe pump. The parameters of the pump were set accordingly and pumped out droplets with volumes of 6.2, 7.7 and 9.6 μL , which were corresponding to the needle diameter of 0.3, 0.4 and 0.5 mm. The images were captured at 4000 frames per second. The equipment used to record the droplets is a high-speed camera Fastcam Mini (Photron Shanghai) with wide zoom lens (Tokina AT-X Pro Macro 100 mm F2.8D). The images were captured at 4000 frames per second.

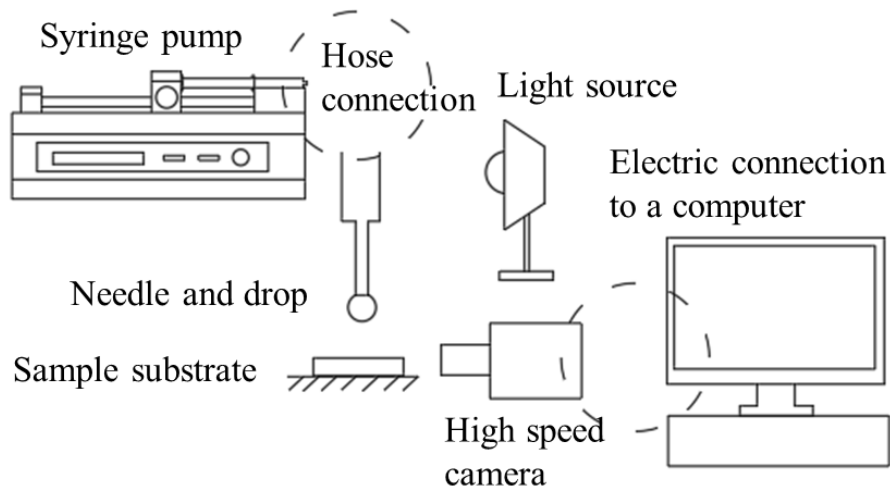


Fig. 6.1 The schematic of impact of water droplets

6.3 Theoretical analysis for droplet impact

6.3.1 The mass-spring system of the bouncing process

Through observing the bouncing behaviors of the water droplets, a mass-spring system was proposed and believed to be able to model the bouncing process (Biance, Chevy, Clanet, Lagubeau, & Quéré, 2006; Okumura, Chevy, Richard, Quéré, & Clanet, 2003). The system is a spring (initial length l_0 and stiffness k) connecting two masses (equal in weight $m/2$) at each end. The bounce can be roughly divided into two phases. First the water droplet impinges the surface and spreads so that the kinetic energy is partially stored as surface energy, which is corresponding to the compressed spring storing elastic energy. The droplet then recoils and starts to detach from the surface. In this phase, the surface energy is transferred to translational kinetic energy and oscillatory kinetic energy. The schematic diagram to show the process is displayed in Fig. 6.2.

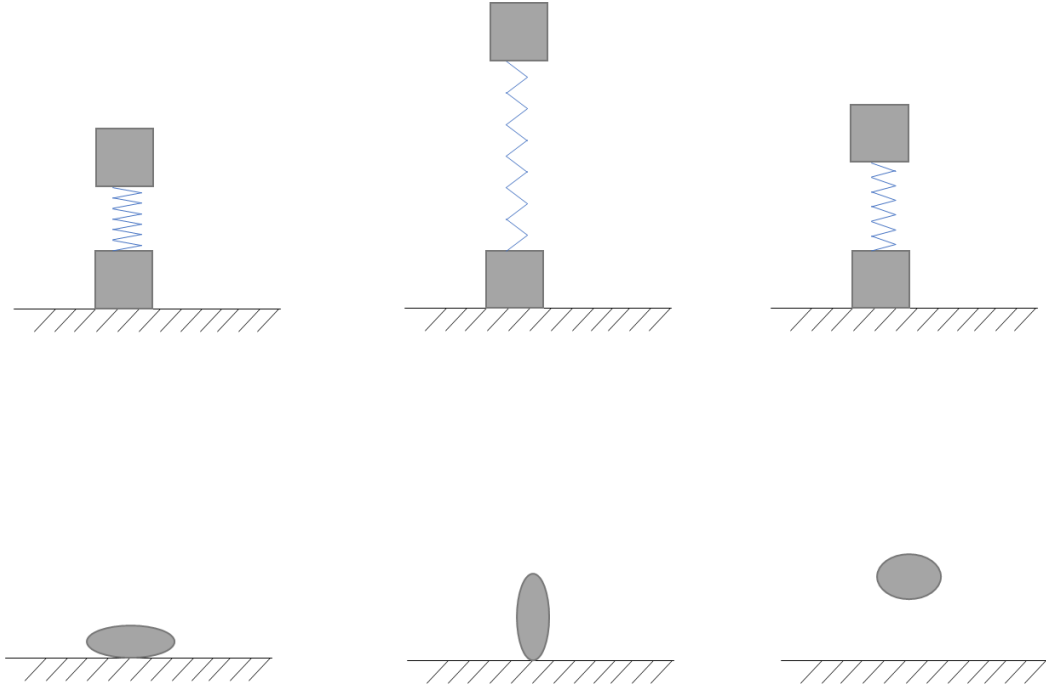


Fig. 6.2 The schematic diagram showing comparison between the mass-spring system and the bouncing droplet.

The Newton's equation of motion could be used to describe the spring-mass system. The position of the top mass is denoted as x_1 and the bottom mass denoted as x_2 . The reaction force from the solid surface is denoted as F_{re} .

$$0.5m \frac{d^2 x_1}{dt^2} = -0.5mg - k(x_1 - x_2 - l_0)$$

$$0.5m \frac{d^2 x_2}{dt^2} = -0.5mg - k(x_2 - x_1 + l_0) + F_{re}$$

When the bottom mass contacts the substrate, $x_2 = 0$ and the force acting on the mass might be negative. The position of the top mass can be expressed as

$$x_1(t) = l_0 - \frac{mg}{2k} + \left(\delta - l_0 + \frac{mg}{2k} \right) \cos\left(\sqrt{\frac{2k}{m}} t \right)$$

where δ is the minimum length of the spring and $\sqrt{\frac{2k}{m}}$ comes from the natural pulsation of the mass. The adhesion force generated from the surface tension fluctuates during the bouncing process and is therefore difficult to yield an expression. Nonetheless the energy consumed by the adhesion can be expressed according to literature (Öner & McCarthy, 2000)

$$W = A\Delta\gamma = A(\gamma_{LV} + \gamma_{SV} - \gamma_{LS})$$

When the droplet was about to leave the sample surface, the force from the sample acting on the bottom mass becomes zero and the system suffered a loss of energy consumed by adhesion. The time t_0 when the bottom mass is about to take off can be found in the implicit expression

$$-\frac{mg}{k} + \left(\delta - l_0 + \frac{mg}{2k}\right) \cos\left(\sqrt{\frac{2k}{m}}t_0\right) = 0$$

The equation admits a solution when the spring is fully compressed, and we can thus find $\delta < l_0 - \frac{mg}{k}$. Denoting the center position of the spring-mass system as the mass center of the droplet, the velocity of rebound V' can be expressed as:

$$V' = \sqrt{\frac{kl_0^2}{2m} \left(1 - \frac{mg}{2kl_0}\right) \left(1 + \frac{3mg}{2kl_0}\right) - \frac{2W}{m}}$$

If the water droplet is very small, the expression can be simplified as

$$V' = \sqrt{\frac{kl_0^2}{2m} - \frac{2W}{m}}$$

If the surface substrate is very repellent to water, the energy consumed by adhesion W will be almost zero, a simpler expression can be obtained

$$V' = l_0 \sqrt{\frac{k}{2m}}$$

The water droplet falls from various heights and is compressed when it hits the substrate surface. When the droplet $We \gg 1$, it will turn into a thin pancake shape at the lowest point. Despite the different heights, the deformed droplet reaches a maximum contact area with the substrate of around $d_0 We^{0.25}$ (D. Richard & Quéré, 2000). Associating the contact area A with the energy consumed by adhesion W , the velocity could be expressed as

$$V' = \sqrt{\frac{kl_0^2}{2m} \left(1 - \frac{mg}{2kl_0}\right) \left(1 + \frac{3mg}{2kl_0}\right) - \frac{\pi\Delta d_0^2}{2m} We^{0.5}}$$

where d_0 is the initial diameter of the droplet. To find the constants of the spring-mass system, we can take the stiffness k as γ_{LV} , and the length l_0 as the diameter of the droplet d_0 .

According to this mass-spring model, the take-off speed of the rebounding droplet is surprisingly not directly affected by the impact velocity. The impact would influence the oscillation of the droplet, which is also an important factor of the rebounding height. This model explains why the increase of rebound height would become minute as the impact velocity increases. On the other hand, the droplet oscillation will become severe. As in practical cases the mass of the liquid will take off in a continuous manner rather than a rigid body, the rebound height will still present a small increase with the impact velocity and can be regarded as an indicator for the water repellence of the substrate.

6.3.2 Energy dissipation

Generally, when a droplet lands on a surface, it first spreads and forms an ellipsoid or a pancake. Then it possibly retracts or not, depending on its impact velocity and the condition of the surface it lands on. During this process, because of the finite energy losses in the bouncing process, the rebound height for each impact gets slightly lower than the previous bounce. Naturally, energy loss becomes an essential topic to study.

The kinetic energy of the droplet could be transformed into translational kinetic energy, oscillating kinetic energy and also dissipated. The energy of the water droplet could be dissipated in several ways excepting air resistance. The viscosity of the liquid is one of the reasons for energy dissipation. The surface tension is the other way energy is dissipated, the extent of which was reflected in CAH.

During the spreading and retracting process of the droplet on the impacted surface, part of the total energy is dissipated by surface tension. The droplet spreads and with its shape following the advancing contact angle in the spreading process. The resultant force in horizontal direction does positive work. While the droplet retracts, the droplet shape follows the receding CA and the resultant force also does positive work for the same reason.

For the spreading process, the resultant force per unit length in horizontal direction is

$$\sum \gamma_1 = \gamma_{SV} - \gamma_{LV} \cos \theta - \gamma_{SL}$$

When combined with Young's equation, the previous expression becomes

$$\sum \gamma_1 = \gamma_{SV} - \gamma_{LV} \cos \theta - \gamma_{SL} = \gamma_{LV}(\cos \theta - \cos \theta_A)$$

There is a similar expression for the force per unit length during the retracting process is

$$\sum \gamma_2 = -\gamma_{SV} + \gamma_{LV} \cos \theta + \gamma_{SL} = -\gamma_{LV}(\cos \theta - \cos \theta_R)$$

The energy dissipated by surface tension could then be expressed as

$$W = 2A\gamma_{LV}(\cos \theta_R - \cos \theta_A)$$

Here the adhesion number Na is introduced as a term concerning of the extent of adhesion. It is related to the dynamic contact angles and directly reflects the metastable states of the liquid meniscus at the interface of the three phases. It can be expressed as (Mittal, 2003)

$$Na = \frac{F_a}{RK\gamma_{LV}} = \cos \theta_R - \cos \theta_A$$

where F_a is the adhesion force, R is the radius of liquid-solid contact area, K is a proportionality constant.

And for this number Na , there is also

$$Na = \cos \theta_R - \cos \theta_A \approx 2 \sin \theta \sin \frac{\theta_A - \theta_R}{2}$$

Here the apparent contact angle θ is precisely $(\theta_A + \theta_R)/2$. The two values are close to each other for superhydrophobic surfaces which have a small CAH.

The viscous dissipation of a droplet mainly occurred in droplet deformation during the spreading and retracting process. The work against

viscosity could be approximately expressed as $W = \int_0^t \int_{\Omega} \Psi d\Omega dt \approx \Psi \Omega t$ (Pasandideh-Fard, Qiao, Chandra, & Mostaghimi, 1996), where Ω is the droplet volume, Ψ is a function of viscosity and t is the contact time. The magnitude of Ψ is given by

$$\Psi = \mu(V_0/\delta)^2$$

where μ is the dynamic viscosity and δ is the boundary layer thickness. The flow of a droplet impacting on the solid surface is approximated as stagnation point flow. Therefore the boundary layer is $\delta = 2.4\sqrt{\mu D_0/(\rho V_0)}$. The expressions indicate that the energy dissipation is mainly dependent on the droplet deformation and the contact time. Substituted with some basic parameters, the work against viscosity is assumed to be

$$W = 2\pi\mu D_0 D_{max}^2 V_0^2 / 3\delta$$

where D_0 is the unperturbed droplet diameter, D_{max} is the maximum diameter during the bouncing process and V_0 is the impact velocity.

6.3.3 Droplet shape analysis

Temporal evolution of the shape of the bouncing droplet is an important aspect in the analysis of the kinetic characteristics. The spreading factor β of the droplet is defined as the ratio of spreading diameter to original diameter. It's a key parameter describing the deformation of the impinging droplet. It is correlated Weber number, Reynolds number or their combination in varied scaling laws for prediction in the possible application fields (Clanet, Béguin, Richard, & Quéré, 2004; Ukiwe & Kwok, 2005). The contact time refers to the time during which the

droplet is in contact with the solid surface. The contact time of the first bounce is also critical for analyzing the bouncing behaviors. It has an effect in applications including anti-icing and dropwise condensation (Bird, Dhiman, Kwon, & Varanasi, 2013; Y. Liu et al., 2014).

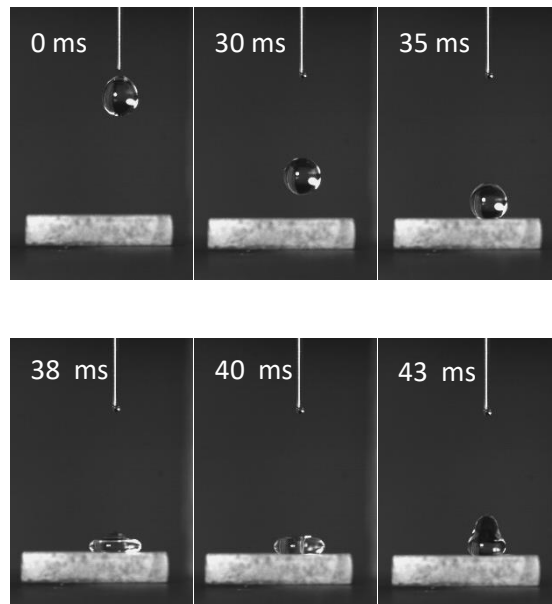
The spreading factor reaches a maximum value as the droplet is compressed, which is denoted as β_{\max} . This value increases as the water droplet impacts onto the surface with an ascended velocity. For superhydrophobic surfaces where viscous dissipation is relatively minimal, the maximum spreading factor roughly satisfies a scaling law of $\beta_{\max} \sim We^{0.5}$ (Laan, de Bruin, Bartolo, Josserand, & Bonn, 2014). On the contrary when viscosity becomes a major term, the spreading factor is yielded as a balance between the kinetic energy and viscous dissipation, satisfying a scaling law of $\beta_{\max} \sim Re^{0.2}$ (Fedorchenko, Wang, & Wang, 2005).

The contact time scales with the inertial-capillary timescale equation $\tau = \pi\sqrt{\rho R_0^3/2\gamma}$. In this equation ρ refers to the liquid density, R_0 the droplet original radius and γ the surface tension (Abolghasemibizaki & Mohammadi, 2018). To enable comparison, a dimensionless time t_c/τ_w is always proposed.

6.4 Results and discussion

Apart from the traditional contact angle measurement, water droplet bouncing experiments were conducted on the NiO-FAS-17 coated superhydrophobic surfaces to investigate the wetting properties. Ni-FAS-17 coated surfaces and bare copper surfaces with UPM fabricated surfaces possessing poorer

hydrophobicity were also tested for comparison. Samples were placed on the stage and tuned to proper heights from very close to the droplet and about 30 mm. The unperturbed diameter of the droplet is from 2.28 mm to 2.64 mm. The impact velocity varied based on different releasing heights. This yields a Weber number ranging from 1.98 to 19.80. When the droplet fell from a certain height and impacted on the superhydrophobic substrate, it was compressed and deformed in the localized region and spread to a maximum lateral extension. The shape of the droplet did not change a lot before colliding with the surface. It kept changing throughout the rebounding process as the transfer of translational energy to oscillational energy occurred and conversely as well. The droplet would continue bouncing for about 6-9 times before it finally detached from the sample. Each time the rebound height declined as energy was dissipated on the substrate and in the droplet deformation. The general process is presented in Fig. 6.3, where the first two bounces in a case were included.



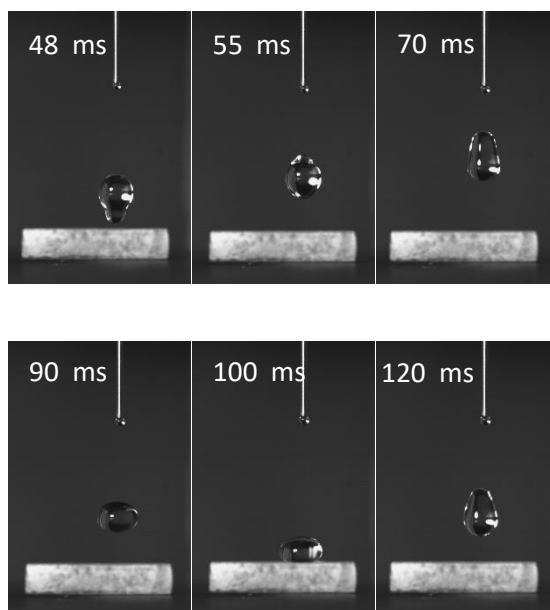


Fig. 6.3 Images of a typical case of the water droplet bouncing movement on the NiO-FAS-17 coated superhydrophobic surface.

As the sample surface was not perfectly horizontal, lateral movement of the droplet existed throughout the bouncing process. The displacement became distinct as it was accumulated with time. The droplet would finally fall out of the sample area with a finite dimension of 10 mm × 10 mm. This is an indication of the good water repellence of the sample. In this experiment the number of the bounces to some degree depends on the distance from the landing position to the sample edge. The number of bounces is therefore not applicable for quantitatively describing the hydrophobicity of the sample surfaces.

6.4.1 Droplet bouncing behaviors on less hydrophobic surfaces

The water droplet is believed to get stuck or perform fewer bounces on hydrophilic or less hydrophobic surfaces. The droplet trajectories were recorded

on the copper micropillar surface and the Ni-FAS-17 coated flat surface to study their water repellency. The two cases were performed with droplet volume around 7.7 μL and releasing height of around 18 mm. The serial images in Fig. 6.4 indicates the droplet impact behaviors on Cu micropillar surfaces. The droplet impacted the surface and was compressed to a pancake shape. When it began retracting, the droplet ascended with the lower part contacting the substrate reducing. The lower part kept reducing till it formed a small drop separated from the main part and was left on the substrate. The main part recovered to a sphere and performed a short bounce before it fell back. Then the two parts merged and oscillated on the substrate. No more bounces occurred, and the droplet finally maintained still on the substrate.

The serial images in Fig. 6.5 show the droplet impact behaviors on the Ni-FAS-17 coated flat copper surface. The surface is flat without any geometries, which can reach a roughness of around 50 nm according to the measurements stated in Chapter 4. The droplet got stuck when it impacted on the sample surface and then oscillated for a few microseconds without performing any bounces.

The water droplets did not show good bouncing behaviors on these two types of surfaces. According to the test results stated in Chapter 4, both the surfaces did not reach the criteria that the CA is over 150° and the CAH does not exceed 10° (Crick, C., Parkin, & I., 2011). The energy was dissipated in the spreading and retracting process against surface tension. Nevertheless, the experiments still to some degree show the individual effect of the hydrophobic coating on the water droplet bouncing behaviors. The droplet performed a short bounce on the micropillars while it could only recover to a hemisphere shape on the Ni-FAS-17 surface under approximately the same conditions. This indicates that in certain

circumstances the micropatterns would make the surfaces less adhesive to impacting water droplets than modification of low surface energy materials on flat surfaces with neutral wettability.

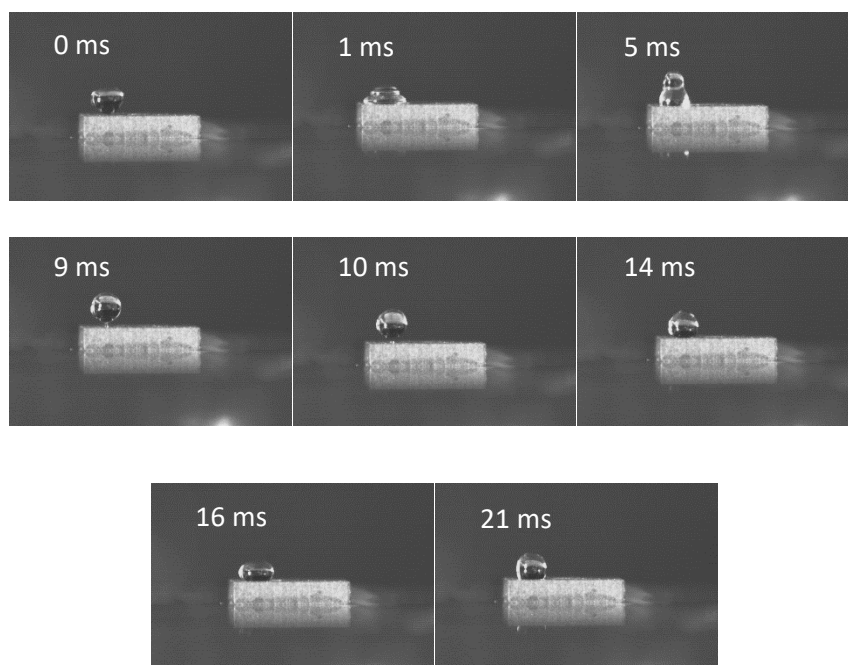


Fig. 6.4 Images of a water droplet performing one rebound and the subsequent oscillating on the copper micropillar surface.

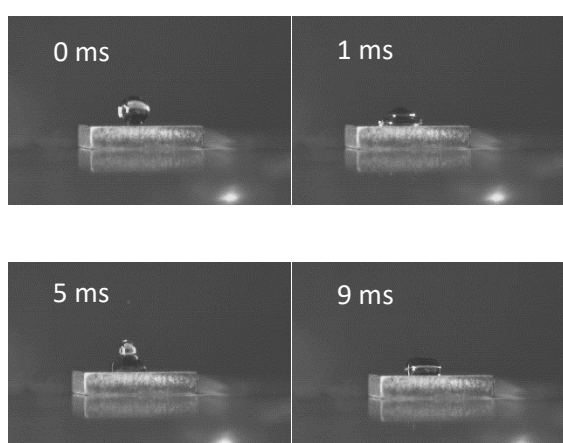


Fig. 6.5 Images of a water droplet oscillating on the Ni-FAS-17 coated flat copper surface.

6.4.2 Droplet bouncing behaviors on the NiO-FAS-17 microgroove surfaces

The NiO-FAS-17 coated samples presented good superhydrophobicity as stated in previous chapters. The wetting properties with CAs around 160° and CAHs smaller than 10° , which fulfils the criterion for a full rebound proposed in a previous report (C. R. Crick & Parkin, 2011). Multiple bounces were recorded while the first rebound of the whole process would be the focus in this section. This is because the lateral displacement is not distinct in the first rebound. Analysis on the first rebound is suitable and enough for evaluating the wettability of the prepared samples. The analysis only on the first bounce also indicates that the evaporation resulting from the illuminating source for the high-speed camera could be neglected, considering the timescale (within 100 ms) and the droplet volume (6~10 μL). Different types of superhydrophobic surfaces were tested in the water droplet bouncing tests to study and compare their wettability. The tests were conducted under different Weber number, which was achieved through tuning the releasing height and the droplet size.

According to the recorded dynamic behaviours of the water droplets, the droplet movement concerning the compression of water drops and fragmentation in the retracting process varied with the rising We . The different bouncing behaviours could be roughly divided into three types dependent on the fragmentation of the bouncing droplet. The representatives of the three types are displayed in Fig. 6.6. When We was small (roughly from 3.6 to 5.2), the droplet was not strongly compressed and rebounded to a height relatively close to the initial releasing height. This was denoted as bouncing type I. The spreading factors

were relatively small. The oscillation of the droplet was not fierce during the rebounding period judging from the droplet deformation. The droplet kept its integrity throughout the process and fragmentation could not be observed. The energy of the whole system is relatively small while the loss of energy is also modest. When We was increased to an intermediate value (roughly from 6.7 to 11.1), the droplet was compressed evidently to a thin pancake shape. This was denoted as bouncing type II. The inertia of the droplet became dominant, and the droplet deformation was thus severe. The oscillation of the droplet after the take-off from the sample surface was also stronger than in type I. At the starting period of retracting, small drops were separated from the main drop and rebound in a high velocity. The droplets were small and sometimes difficult to observe at smaller We . Such phenomenon reflects the increase of We , which is caused by stronger kinetic energy compared to surface tension. When We was further enlarged exceeding 11.1 and reaching around 13.2, the bouncing type III was presented. Remarkable droplet deformation and fragmentation could be observed driven by a stronger influence of inertia. The difference from type II is that fragmentation from the upper side of the droplet showed an abrupt increase in the droplet size. This occurred when the main drop oscillated and recovered from the pancake shape to a hemisphere. The separated drop left from the main drop in a relatively low velocity, indicating its large size and inertia.

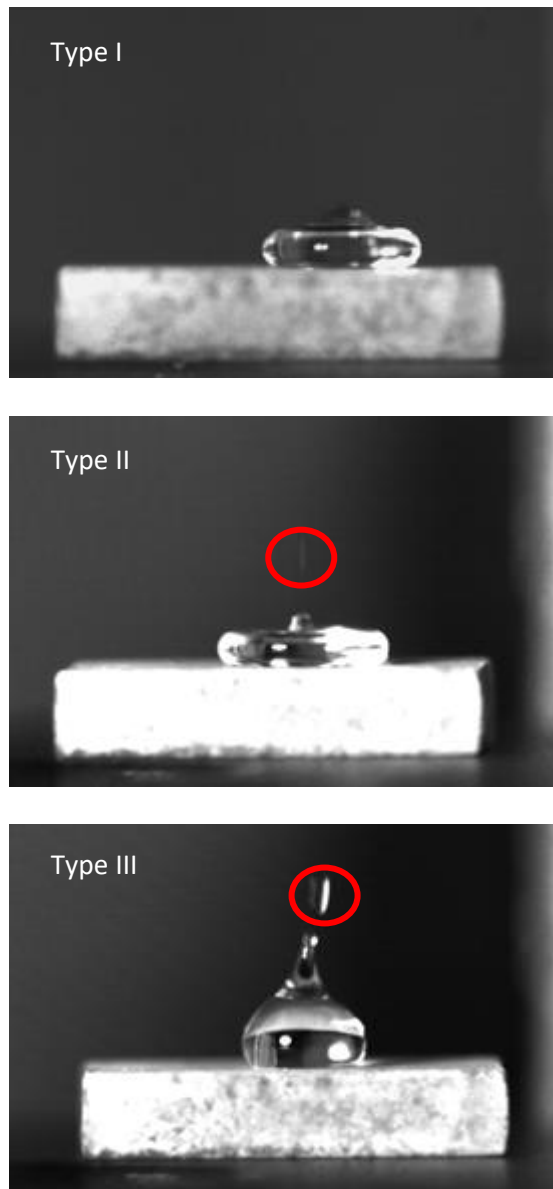


Fig. 6.6 Images of three droplet bouncing types. The fragmented water drops are circled in red.

To quantitatively describe the kinetic performance of the bouncing droplet, the time evolution of the spreading factor is presented in Fig. 6.7. The experiments were conducted under relatively small Weber numbers where droplets would not splash and scatter. The spreading factor starts from zero with the moment the droplet became in contact with the sample surface set as the origin of the

coordinate. The spreading factor first rises with the bouncing process and the maximum values mostly appear at relatively fixed time (time = 2.5 ms). It gradually declined until zero, indicating complete detach from the surface. The spreading factor becomes larger when the Weber number ascends, as the inertia becomes dominant, and the surface tension is not enough to keep the spherical shape of a droplet. The trends of the curvatures are almost the same with a single arc. There are small fluctuations observed when $We = 1.98$ and 5.1 . This is probably reflection of minute vibration resulting from the dispensing of the droplet. The interference is covered under larger We as the total energy of the impinging droplet becomes large.

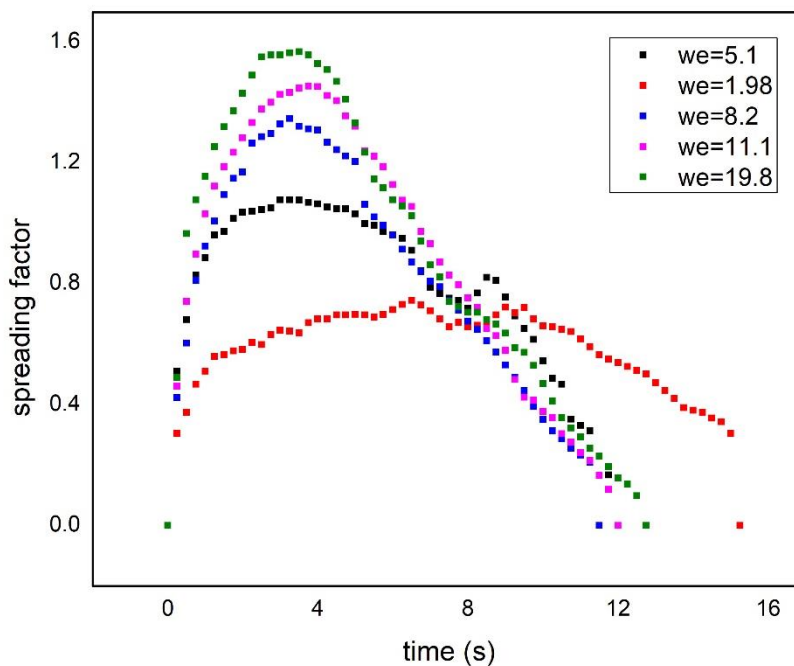


Fig. 6.7 Temporal evolution of the spreading factor for impinging water droplets on NiO-FAS-17 coated flat copper surfaces at different Weber numbers

The spreading factor curves of different sample substrates are also calculated and compared. Here the time evolution of water droplets at $We = 10.1$

impacting on three different types of superhydrophobic surfaces was presented in Fig. 6.8. The NiO-FAS-17 coatings on either the groove surfaces or the flat surface do not differ a lot. Considering error resulting from measurement of droplet shape and Weber number, while a larger spreading factor indicates better water repellency, the values presented here are not sufficient to distinguish the hydrophobicity of the three types of surfaces. Some other properties need to be investigated for surface wettability evaluation.

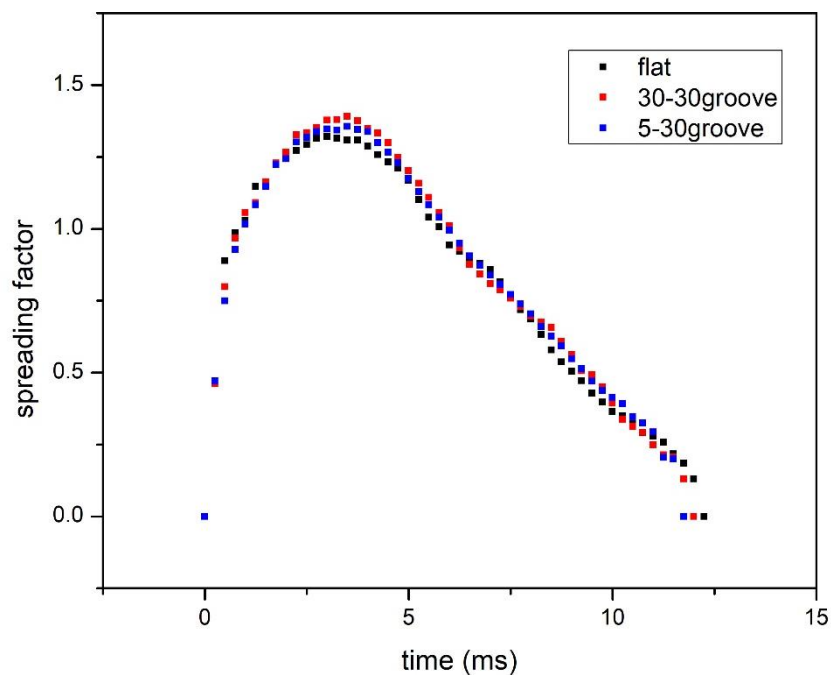


Fig. 6.8 Temporal evolution of the spreading factor for impinging water droplets on different NiO-FAS-17 coated superhydrophobic surfaces

The surface-liquid contact time could also be acquired through the calculation. As it is correlated with the exchange of mass, momentum and energy between the sample surface and the droplet, a minimized contact time is

advantageous for a superhydrophobic surface (Bird et al., 2013; Y Shen et al., 2015; Yizhou Shen et al., 2015).

Through observation of high-speed photography of the bouncing drops, the contact time was found to be independent of We over a wide range although the amplitude of the droplet deformation varied with it. This is similar to the oscillation of a harmonic spring despite the fact that the droplet oscillations are far from being linear. The result is also consistent with a representative result in a previous report (Denis Richard et al., 2002). Results of contact time tested using the same droplet size of 7.7 μL were displayed in Fig. 6.9. As the volume of the water droplet is not altered, this means the contact time in a certain range is independent of impact velocity. The horizontal axis is the Weber number and the vertical axis is the contact time. While the contact time of the first bounce on the three types of surfaces are around 12 ms, the contact time on grooved surfaces is slightly smaller than on the flat surfaces, especially under greater We . As it is independent of impact velocity, an average of the contact time can be calculated to see the effect of the three samples with different geometries. The NiO-FAS-17 coated flat surface, 30-30 microgroove surface and 5-30 microgroove surface presented contact time of 12.4 ± 0.2 ms, 11.8 ± 0.4 ms and 11.6 ± 0.3 ms, respectively. This was most close to the theoretical equation $\tau_w = \pi\sqrt{\rho R_0^3/2\gamma}$ (Wachters & Westerling, 1966), presenting errors no larger than 10%. The error is due to the factors including characteristics of the surface, the gravity acceleration and atmospheric pressure that are not taken into account (H. Hu, Chen, Huang, & Song, 2013).

The NiO-FAS-17 coated flat surface presented slightly larger contact time than the coated microgroove surfaces. The differences are seven smaller within the hierarchical samples with different groove periods. This is probably because the current testing conditions are not enough to differentiate the hydrophobicity of the samples. The lack of methods for more precise measurement is also an obstacle to find solid results supporting the superior hydrophobicity of hierarchical surfaces over the flat surfaces in the perspective of contact time.

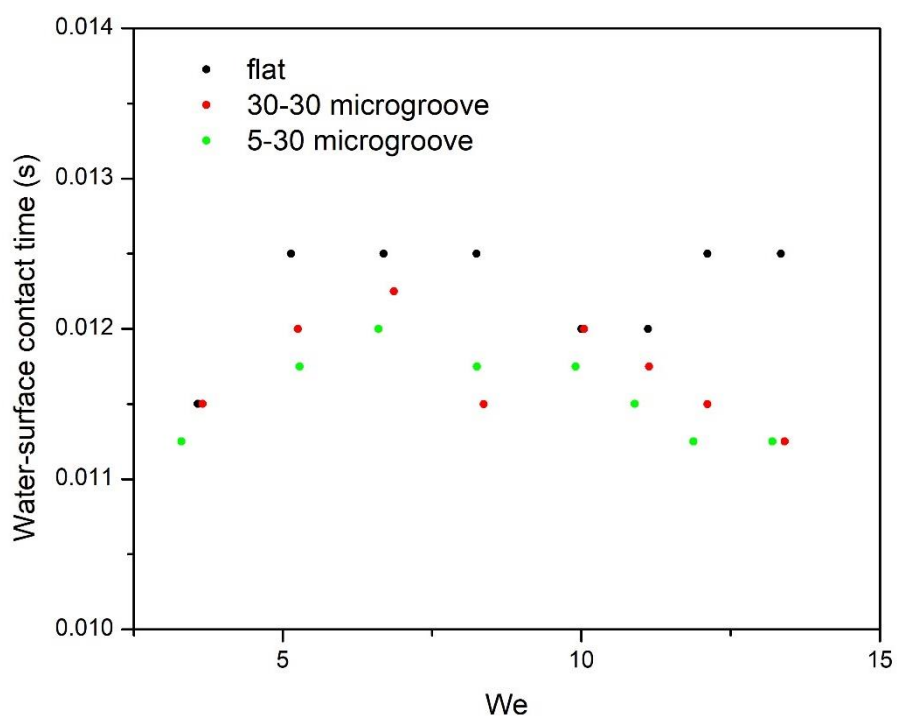


Fig. 6.9 The contact time of the first bounce of the 7.7 μL droplet on the NiO-FAS-17 coated 30-30 microgroove surface

The height of the first rebound was another intuitive property that can be used to quantify surface hydrophobicity. The first rebound height of the 7.7 μL -volume water droplet impacting on a NiO-FAS-17 modified flat copper surface

was displayed in Fig 6.10. The horizontal axis is the We number of a droplet when it is approaching the sample surface. The vertical axis is the first rebound height, which is defined as the highest position the droplet reach at the first bounce of the whole process. The restitution coefficient $\varepsilon = v'/v$ is also calculated accordingly, listed in the right vertical axis. The experiment was repeated at least 3 times for each case and the error bar was calculated and presented accordingly. The restitution refers to the ratio of the velocity after impact v' over the velocity just before the impact v . In our cases the impacting or bouncing velocity is determined as

$$v = (2gh)^{0.5}$$

under the assumption of ignoring air resistance, where h stands for the droplet releasing height or maximum rebound height.

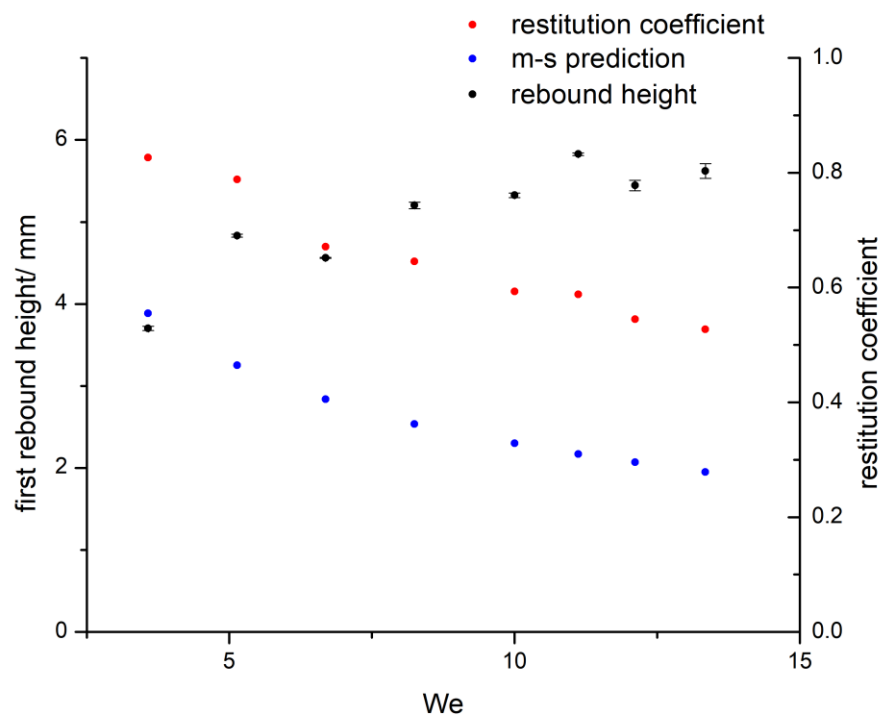


Fig. 6.10 Diagram of the first rebound height (black dots), the restitution coefficient (red dots) and the restitution coefficient predicted from the mass-spring model (blue dots) against We of water droplets impacting on the NiO-FAS-17 coated flat copper surface

According to the testing results, the restitution coefficient could reach 0.8 when the droplet is released from small heights (5 mm and 8 mm case), corresponding to We smaller than 5.2. This is an indication for surfaces with good hydrophobicity. The rebound height generally increased with the rising We , while the restitution coefficient decreased. The first rebound height increased with the rising impact velocity of the droplet, as compression of the droplet at first rebound became severe and the rebound height naturally ascended. The energy of the whole system is relatively small while the loss of energy is also modest under a small We . Therefore the restitution coefficient remains a high value. The loss of energy from viscosity, surface adhesion and oscillation become distinct under large We and causes the decrease of restitution coefficient. This trend was basically consistent with the theoretical predictions in the mass-spring system. The rebound velocity does not increase a lot with the ascended releasing height as much of the total energy was transformed into oscillation. This is reflected in the decline of restitution coefficient with the Weber number, as the energy dissipation makes up a relatively small part. While the actual rebound velocity slightly increases with the impact velocity, the discrepancies with the mass-spring model occurred mainly because the interaction of the droplets with the superhydrophobic surfaces and the internal force of water is not included in the model and there are errors in the complicated experimental and data processing process as well. Fragmentation of

droplets became severe as We increases and reduces the energy of the main drop. This also contributes a lot to the dramatic decrease of restitution coefficient as it is calculated from the height of the main drop. On the other hand, two fallbacks in the first rebound height series were recorded. The fallbacks occurred when We is around 6.7 and 12.0, which was found to be corresponding to the change of bouncing type. When We is small, the droplet could keep its integrity throughout the process. The droplet presented increasing rebound height when We is within this range. When We exceeds 6.7, it is large enough to encounter fragmentation of the water droplets. The first fallback would be recorded with the sudden loss of energy from the separated drops. The deformation of the droplet became more severe under when We is further enlarged. The change to bouncing type III featuring a distinct droplet break-up is recorded when We was around 12.0. This also brings about an abrupt increase in energy loss and is corresponding to the second fallback in the first rebound height.

The experiments were also performed on the hierarchical surfaces based on the NiO-FAS-17 coated 30-30 microgrooves and 5-30 microgrooves. The first rebound heights of NiO-FAS-17 coated 30-30-microgroove surface and NiO-FAS-17 coated 5-30-microgroove surface were displayed in Fig. 6.11 and 6.12. There are also small turns in the curves of the two types of samples, which are growths of rebound heights smaller than the expected trends of the curves. The turns are matched with the change of bouncing type. While in gross the bouncing behaviors on the hierarchical superhydrophobic sample surfaces were the same as on the NiO-FAS-17 coated flat samples, there are some quantitative differences concerning the first rebound height and the bouncing type. As the droplet properties are the same for different sample surfaces where they landed, the

properties including first rebound height and restitution coefficient could represent the energy remained in a single water droplet after bouncing and reflect the hydrophobicity of the impacted surfaces. According to the experiment results, the rebound heights of the hierarchal surfaces were always no smaller than the NiO-FAS-17 coated flat surface and evidently larger in most of the cases especially at We which was corresponding to bouncing types I and III.

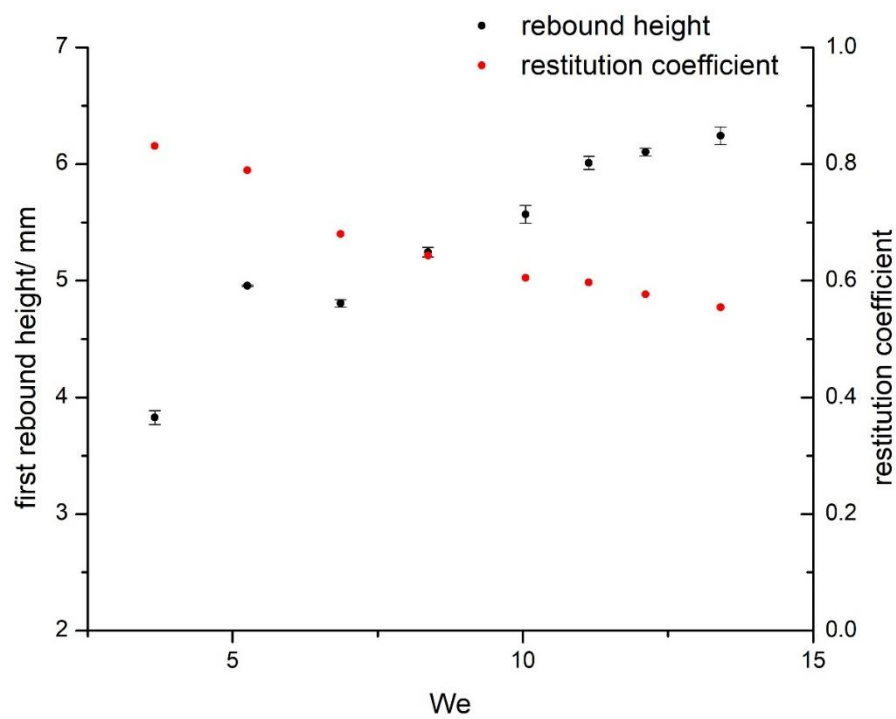


Fig. 6.11 Diagram of first rebound height against We of the water droplet impacting on NiO-FAS-17 coated 30-30 microgroove copper surface

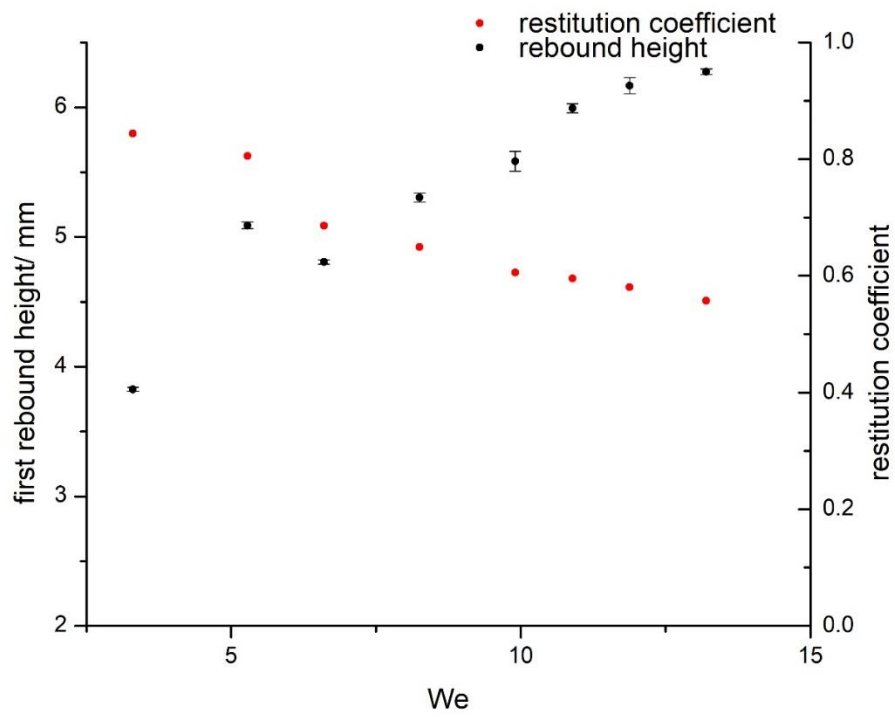


Fig. 6.12 Diagram of first rebound height against We of the water droplet impacting on NiO-FAS-17 coated 5-30 microgroove copper surface

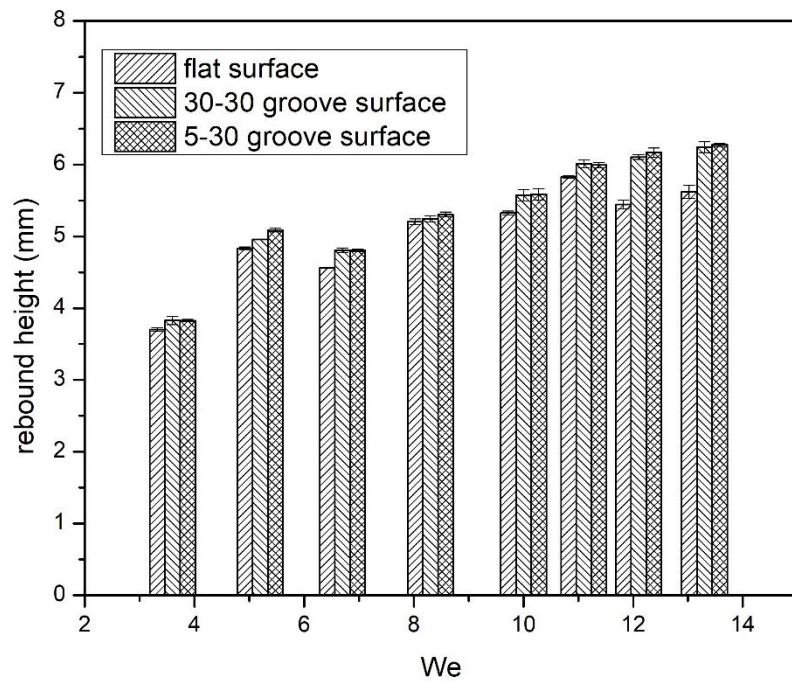


Fig. 6.13 Column chart of first rebound height against We for comparison of different types of surfaces

The details of the bouncing drops were also observed and the change from bouncing type II to type III is found to occur at smaller We on the NiO-FAS-17 microgroove surface than on the flat surface. As presented in Fig. 6.14, for the NiO-FAS-17 flat copper surface, the bouncing type III starts from $We = 12.0$ while for the NiO-FAS-17 coated 30-30 microgroove copper surface the type III starts from $We = 11.1$. The difference could be clearly viewed in Fig .10. Under approximately the same $We = 11.1$ (corresponding to the releasing height of 16.5 mm), the fragmented drops rebounding from the hierarchical surface are significantly larger than the drops rebounding from the modified flat surface. In other words, the water droplet tends to present break-up on the hierarchical surface rather than the modified flat surfaces. As hydrophobicity results in more energy for the droplet break-up, the threshold for the more hydrophobic surface would be smaller in We (Aboud & Kietzig, 2015; J.-P. Zhang et al., 2019). The difference in bouncing type change could therefore also indicate that the hierarchical surface possesses better hydrophobicity than the modified flat surface, which is consistent with the results of the first rebound height.

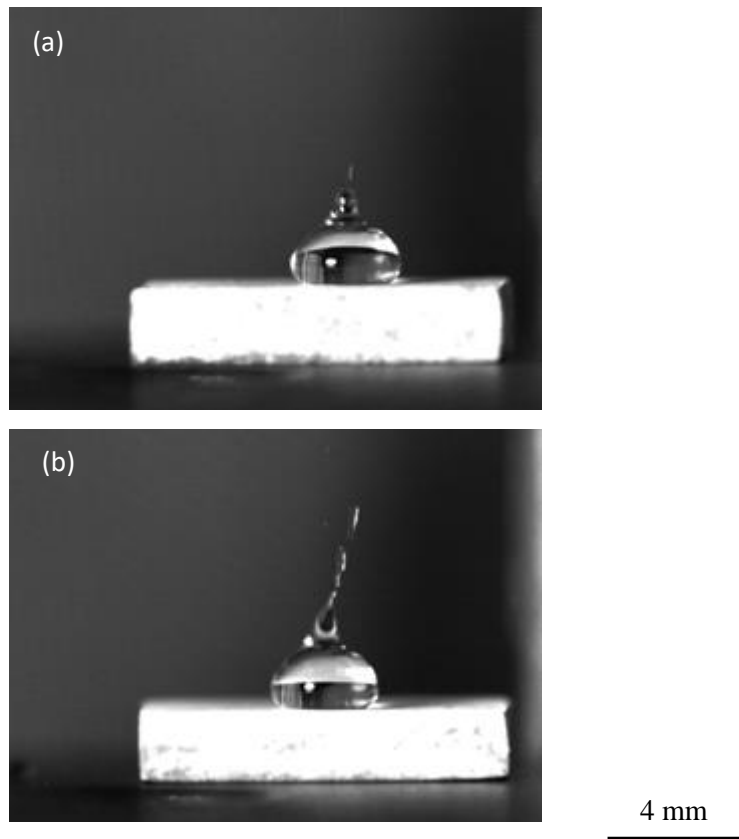


Fig. 6.14 Comparison of the fragmentation of bouncing drops on (a) the NiO-FAS-17 coated flat copper surface and (b) the NiO-FAS-17 coated 30-30 microgroove copper surface under $We = 11.1$.

Meanwhile the dynamic behaviors of the NiO-FAS-17 coated 30-30-microgroove surface and the 5-30-microgroove surface do not differ a lot. The difference in the first rebound height is very limited, which is much smaller than the difference between the 30-30-microgroove and the flat surface. The changes from bouncing type I to II and II to III also occurred at the same We range. This indicates that the existence of the base microstructures plays a more important role than the specific geometries when the dimensions are of several tens of micrometers. The differences of the hierarchical superhydrophobic surfaces with

varied micropattern geometries would probably be discovered unless experiments were performed under some extreme conditions.

6.4.3 Anisotropy of the NiO-FAS-17 microgroove surfaces

The microgroove structure on the copper surfaces induces anisotropy in terms of the geometries. After coated with NiO-FAS-17 superhydrophobic layer, the anisotropy in geometry does not yield any anisotropy in terms of CAs and CAHs, as presented in Chapter 4. In the water droplet bouncing tests, the anisotropy of the microgroove structure could be further studied. The situations are different when the droplet collides the surface with a momentum from a quasi-static process where water is slowly dispensed from near the sample surface. The impacting droplet spread on the superhydrophobic surface and performed a complete recoil when retracting. In this process the maximum diameter of the droplets was recorded as the key property characterizing the droplet deformation. It is the largest diameter of the droplet reaches during its compression of the first impact to the sample surface. Analyzing the radius would contribute to finding the effect of the microgrooves on the spreading process.

NiO-FAS-17 flat surfaces and microgroove surfaces were tested with 7.7 μL -volume droplets released from about 15 mm and 18 mm height, corresponding to We 9.9 and 12.0. The measured largest diameter of the droplets was displayed as in Table. 7.1 and compared with each other. The maximum radius of the droplets on different sample surfaces remained almost the same with a deviation no larger than 1.1%. This indicates that the NiO-FAS-17 nanostructured coating diminishes the anisotropy resulting from the geometry of the microgroove base.

Table. 6.1 The maximum diameter of the droplets impacting on different sample surfaces

	Maximum diameter (mm) release from 15 mm	Maximum diameter (mm) released from 18mm
flat	3.71 ± 0.01	3.95 ± 0.01
30-30 groove orthogonal	3.72 ± 0.02	3.96 ± 0.01
30-30 groove parallel	3.75 ± 0.01	3.97 ± 0.01
5-30 groove orthogonal	3.74 ± 0.02	3.95 ± 0.02
5-30 groove parallel	3.73 ± 0.01	3.93 ± 0.01

6.4.4 Energy dissipation in the bouncing process

Comparing the rebounding drop with the original drop, the energy is transformed in three ways. The viscosity of the liquid is one of the reasons for energy dissipation. The surface tension is another way energy is dissipated, the extent of which was reflected in CAH. The third part of energy goes to the oscillation of the water droplet.

Viscous dissipation is associated with the deformation of the droplet, which occurs in the spreading-retracting process and the oscillation period when the droplet takes off. There is barely any deformation during the free fall, so the viscous dissipation in this period is neglected. To study the viscous dissipation during the first rebound, the contact time, the spreading factor, the maximum diameter and the maximum contact diameter of the water droplets were recorded

as indicators of the droplet deformation. The contact diameter means the diameter of the area where the droplet and the sample surface are in contact. The maximum diameter reflects the extent the droplet deforms. It indicates the balance of the droplet kinetic energy, the surface tension, and the viscous dissipation (J. B. Lee & Lee, 2011). Inertia drives the droplet to spread while the surface tends to pull back the expanding droplet. Viscosity dissipates part of the energy, limiting the expanding velocity and the shape of the sphere.

The maximum diameter and the maximum diameter of the contact area are recorded to feature the shape deformation of the droplet, as displayed in Fig. 6.15 and 6.16. The diameters increased with the rising We according to the diagrams. This is natural as the droplet was compressed more severely when the impact velocity rose. A greater We value would lead to larger droplet deformations. The water droplet was compressed to an ellipsoidal at the lowest point when We was small, and to a pancake shape when We was past 5.2. According to the time evolution curve of spreading factors, the diameter and the contact diameter reached the maximum value at the approximately the same time.

The diameters of droplets impacting on different samples are close to each other, indicating that the deformation of the droplet before retracting is not dependent on the geometries of the surfaces in the tested We range. The introduction of microgroove structure does not result in a distinct difference in droplet deformation. The energy dissipated by viscosity in this process therefore does not differ a lot.

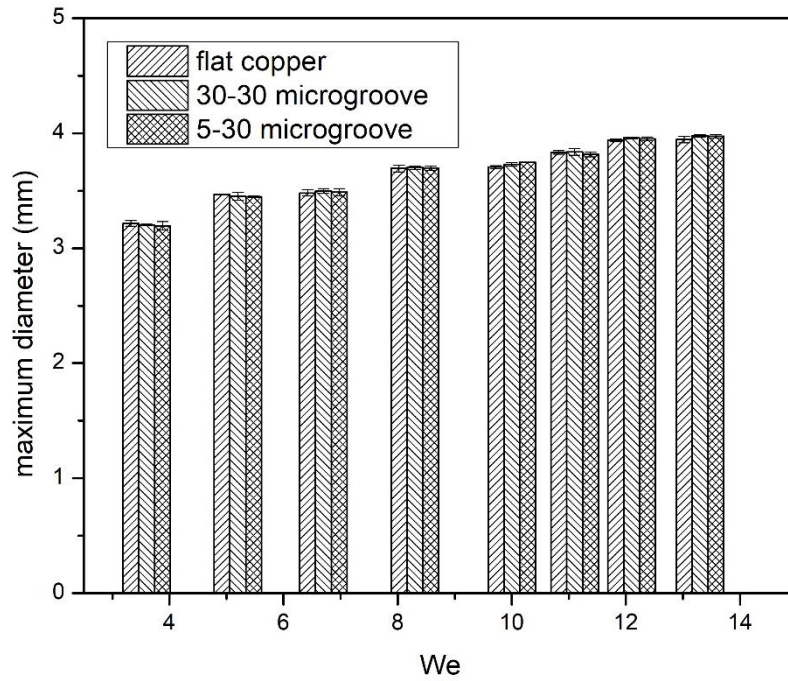


Fig. 6.15 The maximum diameter versus We of the water droplet impacting on NiO-FAS-17 coated flat copper surface

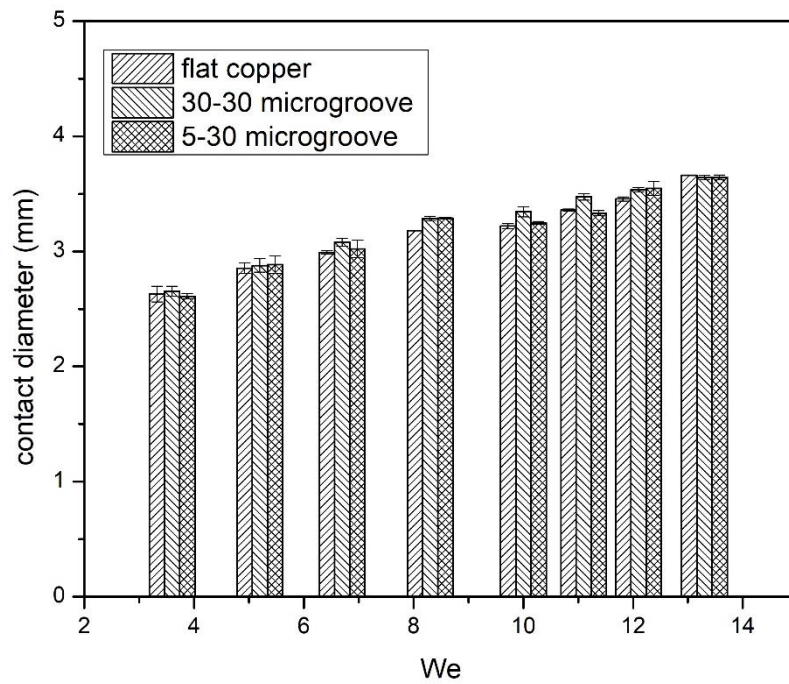


Fig. 6.16 The maximum diameter and the maximum contact diameter versus We of the water droplet impacting on NiO-FAS-17 coated 30-30 microgroove copper surface

Contact angle hysteresis as the second source of energy dissipation is well worth studying. It is reflected as adhesion, which was used to elucidate the rebound quantitatively. To calculate the work of adhesion, the diameter of the contact area was measured through the recorded droplet movement. This could only yield the apparent liquid-solid contact area as the air fraction cannot be validated. As stated in Chapter 4, the advancing and receding CAs of the NiO-FAS-17 coated flat substrate are 163.2° and 158.5° , respectively. The energy dissipated by surface tension in the spreading-retracting process can thus be calculated.

Using the equations stated in section 6.3.2, the energy transformation including viscous dissipation and surface energy can be calculated. The total energy of the droplet could be considered as the gravitational potential. It can be derived through the droplet releasing height. The rebound translational energy can be derived from the rebound height. The results of droplet impacting on NiO-FAS-17 coated flat copper surface are displayed in Fig. 6.17. The surface tension dissipation is not significant compared with the total energy. This reflects that energy is largely dissipated by the other processes, which consists of viscosity, collision and oscillation. On NiO-FAS-17 microgroove surfaces, the contact area is no larger than on the flat surfaces. Energy dissipated by surface tension would also be smaller. The small absolute value of surface tension dissipation could explain the small quantitative difference in rebound height on the three types of superhydrophobic surfaces. However, a lack of measurement method to determine the actual contact area on microgroove surfaces prevents further quantitative analysis of energy transformation.

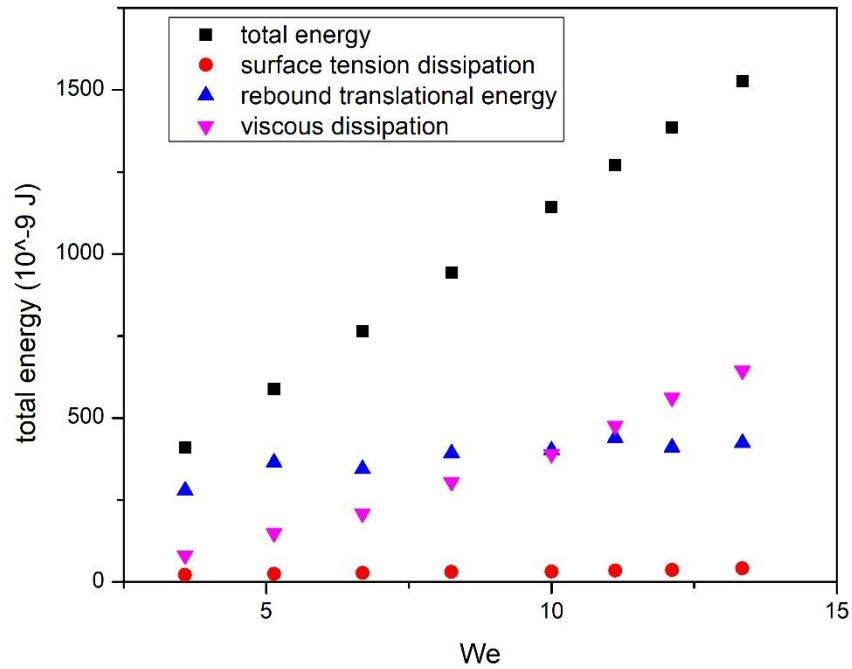


Fig. 6.17 Comparison of total energy and several ways of energy dissipation during the first rebound versus We

The droplet oscillates after it takes off the sample surface. This causes the transformation of total energy into oscillational energy. The energy dissipated by viscosity and surface tension would decline if We decreases, resulting from less disordered flow field and smaller solid-liquid contact. When We is very small, energy dissipation from water viscosity and CAH could be neglected. The restitution coefficient is still significantly lower than 1 due to droplet oscillation.

6.5 Concluding remarks

In this chapter, water droplet bouncing experiments were performed on superhydrophobic micro/nano-structured surfaces based on NiO-FAS-17 coated UPM fabricated microgroove surfaces. Properties including first rebound height, contact time, restitution coefficient, spreading diameters were measured to analyze the dynamic behaviors of the water droplets and to further evaluate the wettability of different superhydrophobic surfaces.

The water droplet could perform multiple bounces on NiO-FAS-17 modified superhydrophobic surfaces rather than the less hydrophobic surface. The dynamic behaviors of the water droplets changed with the governing parameter Weber number. The restitution coefficient of the droplet bouncing on the NiO-FAS-17 coated surfaces remained a high value around 0.8 when We is no larger than 6.7, which indicates good superhydrophobicity.

Three different bouncing types of the water droplets on superhydrophobic surfaces dependent on We were studied, corresponding to different types of droplet fragmentation. The increase of We indicates a dominant role of droplet inertia and causes different types of deformation and fragmentation. When We is small, the droplet would not be fragmented as the total energy is not enough for small drops to break apart. As We increased, the tiny drops broke apart and the main drop was compressed severely. When We is further increased, more distinct break-up of the droplet featured with a large fragmented drop would occur. The threshold We value is around 6.7 and 11.1 for the transition of the bouncing types, which would slightly change due to the wettability of the surfaces.

To compare the hydrophobicity of the NiO-FAS-17 coated surfaces with a flat base and a microgroove base, the first rebound height was recorded and the

restitution coefficient was calculated. The hierarchical NiO-FAS-17 microgroove surfaces presented larger rebound height and restitution coefficient than the coated flat surface. The hierarchical surface also presented droplet fragmentation under smaller We , which means a stronger tendency for the droplet to break up. These could reflect better hydrophobicity of hierarchical surfaces than the coated flat surfaces.

The anisotropy of the microgroove surface was also studied by measuring droplet deformation from the parallel direction and the orthogonal direction. The droplet diameters viewed from two directions are very close, indicating that the adhesion on different directions of the surface is approximately the same. The anisotropy of the microgroove structure in terms of wettability was diminished by the nanostructured NiO-FAS-17 coating.

The fabrication method proposed in this chapter presents an option to fabricate superhydrophobic surfaces could be generalized to other substrates that are compatible with UPM and hydrothermal methods. According to the dynamic wetting behaviors recorded in the chapter, the NiO-FAS-17 layer could present good water-repellent and dust-free properties and could thus be applied on components on a wide variety of mechanical devices.

Chapter 7 Conclusions and suggested future work

7.1 Overall conclusions

The superior properties of micro/nano-structured superhydrophobic surfaces have been increasingly attracting researchers' interest owing to the applications in self-cleaning, corrosion resistance, anti-fogging, drag reduction, *etc.* in a wide variety of industries including aerospace, automotive, shipping and transportation. One of the key factors to increase the hydrophobicity of the functional surfaces is the morphology. Though researchers have studied a lot on both regularly patterned microstructures and randomly shaped nanostructures, investigation on the hierarchical hydrophobic structures are still in progress. Many underlying mechanisms of the effects of the micro/nanostructures on superhydrophobicity and some concerning phenomena are still unclear. Hence, ultraprecision machining as a shaping method through material removal combined with hydrothermal synthesis is a good option to build hierarchical surfaces. Ultraprecision machining provides an efficient approach to fabrication of high precision components with surfaces of patterns in a dimension of microns and surface roughness of nanometers, while hydrothermal synthesis is a facile route to fabricate rough metal oxide micro/nanostructures.

It is generally accepted that compared with individual micropatterns or nanostructures, hierarchical structures might present better hydrophobicity and better performance in its applications, despite the fact that in some cases nanostructured surfaces and hierarchical surfaces with the same chemical

composition present nearly the same performance in the basic properties to characterize wettability (CA and CAH). To study the hydrophobicity of hierarchical micro/nano-structured surfaces and the related applications in corrosion resistance and self-cleaning, fabrication of the hierarchical structures based on cuprous oxide, nickel oxide and UPM fabricated microgrooves were performed. Related characterization methods including morphological observation and electrochemical tests on corrosion resistance were carried out. Water CAs and CAHs were measured to evaluate the surface wettability, and water droplet bouncing experiments were performed for a better understanding of the self-cleaning effect. According to a series of theoretical and experimental investigation and discussion, primary conclusions could be drawn as in the following paragraphs.

A novel method integrating ultraprecision machining and hydrothermal synthesis to fabricate hierarchical micro/nano structured surfaces was proposed. The ultraprecision cutting was performed on the copper surface to form a microgroove structure, followed by hydrothermal synthesis of cuprous oxide rectangular shaped particles or nickel oxide nanoflakes as the secondary structure. After modification with stearic acid or FAS-17, the prepared hierarchical structures presented good hydrophobicity. The Cu_2O -STA coated surfaces presented static contact angles exceeding 140° . The NiO-FAS-17 coated surfaces presented superhydrophobicity with static contact angles exceeding 160° and contact angle hysteresis no larger than 5° . The NiO-FAS-17 microgroove surface possessed good superhydrophobicity amongst all the prepared samples probably resulting from the relatively vertically aligned morphology. The novel fabrication route for superhydrophobic surfaces is not restricted to copper substrates as either

UPM or hydrothermal synthesis can be performed on different metal substrates. It can be generalized to many other nonferrous metals such as Al, Mg and their alloys, which have strong need for hydrophobic anticorrosion coatings.

The Cu₂O-STA based hydrophobic surfaces were investigated for its corrosion resistance properties. According to the electrochemical measurements, the hydrophobic Cu₂O-STA film showed good corrosion resistance. When microgrooves were introduced, the performance was further improved with the corrosion rate reduced approximately by half. The hierarchical structures enhanced the corrosion resistance performance because of the existence of microgrooves to form air pockets and reduce the solid-liquid contact. The microgroove geometries could enlarge the air layer as the corrosion inhibitor, compared with the air layer existing on the rough cuprous oxide film. The method proposed in this study provides an option to fabricate hydrophobic anticorrosion surface and systematically investigate the topography influence on corrosion resistance.

Water droplet bouncing experiments were conducted on NiO-FAS-17 coated superhydrophobic surfaces. Properties including first rebound height, water-surface contact time, restitution coefficient, spreading factors were measured and calculated to analyze the dynamic behaviors of the water droplets on the various surfaces. Three different bouncing types featuring different types of droplet fragmentation were recorded with the rise of the governing parameter We . The droplet would keep its integrity under small We . As We increased, there were tiny drops splashing apart when the main drop started to retract from the sample surface. When We was further increased, distinct fragmentation would be observed with an abrupt increase in the size of fragmented drops.

The restitution coefficient and the first rebound height for NiO-FAS-17 coated microgrooves were larger than that of NiO-FAS-17 coated flat copper surfaces. This indicates a better hydrophobicity of the hierarchical structure than the individual nanostructure modified surfaces. The bouncing droplet also tends to perform break-up under smaller We on the hierarchical surfaces, which indicates smaller energy dissipation and is consistent with the results concerning the rebound height.

The spreading of the water droplet on NiO-FAS-17 coated microgrooves were recorded from parallel and orthogonal directions to study the anisotropy. The compressed drops showed close diameter from either direction, indicating that the hierarchical surfaces were isotropic in terms of wettability, despite an anisotropic groove structure as the base. Moreover, there are no distinct differences in the CAs and the CAHs measured from the two directions. The results could reflect that coating of NiO-FAS-17 has diminished the anisotropy resulting from the groove geometry.

7.2 Suggested future work

Some preliminary outcomes have been achieved in studying the wettability of the hierarchical structured superhydrophobic surfaces and the applications in self-cleaning and corrosion resistance. On one hand, the introduction of UPM fabricated micropatterns would enhance the hydrophobicity of the metal oxide-based micro/nano-structures in certain conditions or application fields. On the other hand, the underlying mechanism still needs further investigation both theoretically and experimentally. Some work has been tried out through

fabricating micropatterns with different geometric factors and tuning synthesis parameters to prepared nanostructured coatings with different morphology. There are still lots of work to be done to reveal the detailed properties and mechanism of the superhydrophobic hierarchical surfaces. The suggested work is proposed here for possible future studies.

Improving durability and fatigue of the superhydrophobic surfaces or coatings is an important task that attracts researchers' attention recently. As the superhydrophobic components would be used for some extreme conditions, the long-term performance in water repelling ability or self-cleaning by rain drops is critical. Coating of hard metals or modification with chemicals with strong bonds to the surface is a feasible route to improve the abrasion resistance of the superhydrophobic surfaces. The durability can also be improved by proper design of microstructures where minor abrasion or damage would not significantly decrease the surface hydrophobicity.

To study the individual effect of micropatterns on hydrophobic corrosion resistance is a useful part to investigate the mechanism of hydrophobic anticorrosion. Different micropatterns can be acquired by many methods including laser texturing and ultraprecision machining. The advantages of ultraprecision machining lie in its precision in the dimension of tens of microns and the low surface roughness of its product. After some treatment to gain a hydrophobic surface on the fabricated patterns, electrochemical measurement can be carried out to evaluate the corrosion resistance behaviors. The absence of nanostructured coatings that would bring about some random influence makes it more convenient to directly evaluate the effect of regular micropatterns in quantity. This would provide solid references for studying hierarchical structures integrating randomly

distributed nanostructures with the micropatterns. The difficulty to realize this research is the fabrication method. As anticorrosion treatment is always performed on metals or alloys that are originally prone to corrosion, preparing a thin layer with good hydrophobicity and stability on such materials without significant changes in surface topography requires quite complicated processing techniques.

Finding a way to observe the solid-liquid interface of a hierarchical surface is also meaningful work that contributes to the understanding of surface wettability. Researchers have proposed many assumptions to describe the contact of water and hydrophobic surfaces, while the transition between Wenzel mode and Cassie & Baxter mode is difficult to figure out as the dynamics of the water drops or flows and the nanoscaled solid surface is very complicated. Microlens equipped with a high-speed camera can be set from side view to capture the water droplet bouncing process on a hierarchical superhydrophobic surface. The lens can be installed from a tilted angle to observe the contact line. In this way the interference with experiment setup can be avoided. The aim of the setup is to observe the movement of water droplets against the profile of the micropattern base of a hierarchical structure.

Appendices

Appendix I Matlab codes for droplet diameter calculation

```
clear all
close all
clc
DataFolder = ['D:\graphs\hs camera\0808\groove2h-7.7-16.5-1_C001H001S0001\'];
FileNum_1 = numel(dir([DataFolder]));
cd(DataFolder)
a=1;
FileNum = numel(dir([DataFolder, '*.tif']));
for a = 276:321
    pickname = ['groove2h-7.7-16.5-1_C001H001S0001', num2str(a, '%06d'), '.tif'];
    myimg = imread(pickname);
    m=size(myimg);

    myimg=im2bw(myimg,0.015);
    myimg=edge(myimg,'canny');
    myimg(1:700,1:m(2))=0;% upper
    myimg(840:m(1),1:m(2))=0;%bottom
    myimg(1:m(1),1:400)=0;
    myimg(1:m(1),600:m(2))=0;
    imshow(myimg, []);
    [m0,n0]=find(myimg==1);
    M=min(m0);
    N=max(m0);% find the rows where 1 exists
    P=min(n0);
    Q=max(n0);

    for i=M:N
        ring=myimg(i,:);
        if ismember(1,ring)==0
            B(i)=0;
        else
            [m1,n1]=find(ring==1);
            B(i)=max(n1)-min(n1);
        end
    end
    D0=0.5*max(B)+0.5*(N-M);%find original diameter
    [m2,n2max]=find(B==max(B));%find the columns of maxB, equal
to rows of largest width
    L=myimg(n2max,:);%the rows of n2max in the image matrix,
presenting largest width
    [m3,n3]=find(L==1);
    S=myimg(N,:);%the row of N in the image matrix, corresponding
to the contact line
    [m4,n4]=find(S==1);
    Maximumdiameter(a)=max(B);
    Spreadingdiameter(a)=max(n4)-min(n4);

end
```

References

- Abolghasemibizaki, M., & Mohammadi, R. (2018). Droplet impact on superhydrophobic surfaces fully decorated with cylindrical macrottextures. *Journal of Colloid and Interface Science*, *509*, 422-431.
- Aboud, D. G. K., & Kietzig, A.-M. (2015). Splashing Threshold of Oblique Droplet Impacts on Surfaces of Various Wettability. *Langmuir*, *31*(36), 10100-10111. doi:10.1021/acs.langmuir.5b02447
- Ahmad, D., van den Boogaert, I., Miller, J., Presswell, R., & Jouhara, H. (2018). Hydrophilic and hydrophobic materials and their applications. *Energy Sources, Part A: Recovery, Utilization, and Environmental Effects*, *40*(22), 2686-2725. doi:10.1080/15567036.2018.1511642
- Ahmad, Z., Rehman, S., & Ahsan, M. (2009). Methods of fabrication of superhydrophobic engineering surfaces: a review. *International Review of Mechanical Engineering*, *3*(3), 312-321.
- Ahmed, K., Grambow, C., & Kietzig, A.-M. (2014). Fabrication of micro/nano structures on metals by femtosecond laser micromachining. *Micromachines*, *5*(4), 1219-1253.
- Al-Ghamdi, A., Al-Hazmi, F., Al-Hartomy, O. A., El-Tantawy, F., & Yakuphanoglu, F. (2012). A novel synthesis and optical properties of cuprous oxide nano octahedrons via microwave hydrothermal route. *Journal of sol-gel science and technology*, *63*(1), 187-193.
- Ang, B. T. W., Zhang, J., Lin, G. J., Wang, H., Lee, W. S. V., & Xue, J. (2019). Enhancing Water Harvesting through the Cascading Effect. *ACS applied materials & interfaces*, *11*(30), 27464-27469.

- Antonijevic, M., & Petrovic, M. (2008). Copper corrosion inhibitors. A review. *Int. J. Electrochem. Sci*, 3(1), 1-28.
- Antonini, C., Amirfazli, A., & Marengo, M. (2012). Drop impact and wettability: From hydrophilic to superhydrophobic surfaces. *Physics of Fluids*, 24(10), 102104.
- Antonini, C., Villa, F., Bernagozzi, I., Amirfazli, A., & Marengo, M. (2013). Drop rebound after impact: The role of the receding contact angle. *Langmuir*, 29(52), 16045-16050.
- BAEYER, H. C. (2000). The lotus effect. *The Sciences*, 40(1), 12-15.
- Baker, E. (1982). *Chemistry and morphology of plant epicuticular waxes*. Paper presented at the Linnean Society symposium series.
- Ball, P. (1999). Engineering shark skin and other solutions. *Nature*, 400(6744), 507-509.
- Barber, A. H., Cohen, S. R., & Wagner, H. D. (2004). Static and dynamic wetting measurements of single carbon nanotubes. *Physical Review Letters*, 92(18), 186103.
- Barthlott, W., & Ehler, N. (1977). Raster-Elektronen-mikroskopie der Epidermis-Oberflächen von Spermatophyten. *Scanning electron microscopy of epidermal surfaces of Spermatophyta.* *Abh. Akad. Wiss. Lit. Mainz, Math.-Naturwiss. Klasse, Trop. Subtrop. Pflanzenwelt*, 19, 367-467.
- Barthlott, W., & Neinhuis, C. (1997). Purity of the sacred lotus, or escape from contamination in biological surfaces. *Planta*, 202(1), 1-8.
doi:10.1007/s004250050096

- Bhushan, B., & Jung, Y. C. (2006). Micro-and nanoscale characterization of hydrophobic and hydrophilic leaf surfaces. *Nanotechnology*, *17*(11), 2758.
- Biance, A.-L., Chevy, F., Clanet, C., Lagubeau, G., & Quéré, D. (2006). On the elasticity of an inertial liquid shock. *Journal of Fluid Mechanics*, *554*, 47.
- Bico, J., Marzolin, C., & Quéré, D. (1999). Pearl drops. *EPL (Europhysics Letters)*, *47*(2), 220.
- Bird, J. C., Dhiman, R., Kwon, H.-M., & Varanasi, K. K. (2013). Reducing the contact time of a bouncing drop. *Nature*, *503*(7476), 385-388.
- Bormashenko, E., Bormashenko, Y., Stein, T., Whyman, G., Pogreb, R., & Barkay, Z. (2007). Environmental scanning electron microscopy study of the fine structure of the triple line and Cassie–Wenzel wetting transition for sessile drops deposited on rough polymer substrates. *Langmuir*, *23*(8), 4378-4382.
- Bormashenko, E., Pogreb, R., Whyman, G., Bormashenko, Y., & Erlich, M. (2007). Vibration-induced Cassie-Wenzel wetting transition on rough surfaces. *Applied physics letters*, *90*(20), 201917.
- Bormashenko, E., Pogreb, R., Whyman, G., & Erlich, M. (2007). Cassie–wenzel wetting transition in vibrating drops deposited on rough surfaces: Is the dynamic cassie–wenzel wetting transition a 2d or 1d affair? *Langmuir*, *23*(12), 6501-6503.
- Bormashenko, E. Y. (2018). *Wetting of real surfaces* (Vol. 19): Walter de Gruyter GmbH & Co KG.
- Brinksmeier, E., Gläbe, R., & Schönemann, L. (2012). Review on diamond-machining processes for the generation of functional surface structures.

CIRP Journal of Manufacturing Science and Technology, 5(1), 1-7.

doi:<https://doi.org/10.1016/j.cirpj.2011.10.003>

- Brinksmeier, E., Mutlugünes, Y., Klocke, F., Aurich, J., Shore, P., & Ohmori, H. (2010). Ultra-precision grinding. *CIRP annals*, 59(2), 652-671.
- Buehrle, J., Herminghaus, S., & Mugele, F. (2003). Interface profiles near three-phase contact lines in electric fields. *Physical Review Letters*, 91(8), 086101.
- Burkarter, E., Saul, C. K., Thomazi, F., Cruz, N. C., Zanata, S. M., Roman, L. S., & Schreiner, W. H. (2007). Electrospayed superhydrophobic PTFE: a non-contaminating surface. *Journal of Physics D: Applied Physics*, 40(24), 7778.
- Byun, D., Kim, J., Ko, H. S., & Park, H. C. (2008). Direct measurement of slip flows in superhydrophobic microchannels with transverse grooves. *Physics of Fluids*, 20(11), 113601.
- Cassie, A., & Baxter, S. (1944). Wettability of porous surfaces. *Transactions of the Faraday society*, 40, 546-551.
- Changwei, Y., Hao, P., & He, F. (2009). Effect of upper contact line on sliding behavior of water droplet on superhydrophobic surface. *Chinese Science Bulletin*, 54, 727-731. doi:10.1007/s11434-009-0029-2
- Chantal, B., Thierry, P., Mireille, T., & Daniel, L. (2007). A ZnO nanowire array film with stable highly water-repellent properties. *Nanotechnology*, 18(36), 365705. Retrieved from <http://stacks.iop.org/0957-4484/18/i=36/a=365705>
- Chen, G., Liang, Y., Sun, Y., Chen, W., & Wang, B. (2013). Volumetric error modeling and sensitivity analysis for designing a five-axis ultra-precision

- machine tool. *The International Journal of Advanced Manufacturing Technology*, 68(9-12), 2525-2534.
- Chen, L., Xiao, Z., Chan, P. C., Lee, Y.-K., & Li, Z. (2011). A comparative study of droplet impact dynamics on a dual-scaled superhydrophobic surface and lotus leaf. *Applied Surface Science*, 257(21), 8857-8863.
- Chen, M.-H., Hsu, T.-H., Chuang, Y.-J., & Tseng, F.-G. (2009). Dual hierarchical biomimic superhydrophobic surface with three energy states. *Applied physics letters*, 95(2), 023702.
- Chen, Y., Chen, S., Yu, F., Sun, W., Zhu, H., & Yin, Y. (2009). Fabrication and anti-corrosion property of superhydrophobic hybrid film on copper surface and its formation mechanism. *Surface and Interface Analysis: An International Journal devoted to the development and application of techniques for the analysis of surfaces, interfaces and thin films*, 41(11), 872-877.
- Cheng, C. T., Zhang, G., & To, S. (2016). Wetting characteristics of bare micro-patterned cyclic olefin copolymer surfaces fabricated by ultra-precision raster milling. *RSC advances*, 6(2), 1562-1570.
- Cheng, J., Liu, C.-s., Shang, S., Liu, D., Perrie, W., Dearden, G., & Watkins, K. (2013). A review of ultrafast laser materials micromachining. *Optics & Laser Technology*, 46, 88-102.
- Cheng, Y., Lu, S., Xu, W., Boukherroub, R., Szunerits, S., & Liang, W. (2017). Controlled fabrication of NiO/ZnO superhydrophobic surface on zinc substrate with corrosion and abrasion resistance. *Journal of Alloys and Compounds*, 723, 225-236.

- Choi, C.-H., Ulmanella, U., Kim, J., Ho, C.-M., & Kim, C.-J. (2006). Effective slip and friction reduction in nanograted superhydrophobic microchannels. *Physics of Fluids*, *18*(8), 087105.
- Choi, Y.-W., Han, J.-E., Lee, S., & Sohn, D. (2009). Preparation of a superhydrophobic film with UV imprinting technology. *Macromolecular research*, *17*(10), 821-824.
- Chu, J., Sun, G., Tong, L., & Jiang, Z. (2021). Facile one-step hydrothermal fabrication of Allium giganteum-like superhydrophobic coating on Mg alloy with self-cleaning and anti-corrosion properties. *Colloids and Surfaces A: Physicochemical and Engineering Aspects*, *617*, 126370.
- Clanet, C., Béguin, C., Richard, D., & Quéré, D. (2004). Maximal deformation of an impacting drop. *Journal of Fluid Mechanics*, *517*, 199.
- Crick, C., Parkin, & I. (2011). Water droplet bouncing—a definition for superhydrophobic surfaces. *Chemical Communications Royal Society of Chemistry*.
- Crick, C. R., & Parkin, I. P. (2011). Water droplet bouncing—a definition for superhydrophobic surfaces. *Chemical Communications*, *47*(44), 12059-12061. doi:10.1039/C1CC14749H
- Dalawai, S. P., Saad Aly, M. A., Lathe, S. S., Xing, R., Sutar, R. S., Nagappan, S., . . . Liu, S. (2020). Recent Advances in durability of superhydrophobic self-cleaning technology: A critical review. *Progress in Organic Coatings*, *138*, 105381.
doi:<https://doi.org/10.1016/j.porgcoat.2019.105381>

- Davies, M. A., Evans, C. J., Vohra, R. R., Bergner, B. C., & Patterson, S. R. (2003). *Application of precision diamond machining to the manufacture of microphotonic components* (Vol. 5183): SPIE.
- Dehghan Manshadi, M. K., Khojasteh, D., Mohammadi, M., & Kamali, R. (2016). Electroosmotic micropump for lab-on-a-chip biomedical applications. *International Journal of Numerical Modelling: Electronic Networks, Devices and Fields*, 29(5), 845-858.
- del Barrio, J., & Sánchez-Somolinos, C. (2019). Light to shape the future: from photolithography to 4D printing. *Advanced Optical Materials*, 7(16), 1900598.
- Di Mundo, R., & Palumbo, F. (2011). Comments regarding ‘an essay on contact angle measurements’. *Plasma Processes and Polymers*, 8(1), 14-18.
- Ding, W., Cao, Z., Wang, B., Xu, S., & Wang, Z. (2019). Research on Hydrophobic Properties of Grating Structure on Monocrystalline Silicon Fabricated Using Micromachining. *Advances in Materials Science and Engineering*, 2019, 3706750. doi:10.1155/2019/3706750
- Dong, L., Zhang, Z., Ding, R., Wang, L., Liu, M., Weng, Z., . . . Li, D. (2019). Controllable superhydrophobic surfaces with tunable adhesion fabricated by laser interference lithography. *Surface and Coatings Technology*, 372, 434-441.
- Emelyanenko, K. A., Sanzharovsky, N. A., Chulkova, E. V., Ganne, A. A., Emelyanenko, A. M., & Boinovich, L. B. (2018). Superhydrophobic corrosion resistant coatings for copper via IR nanosecond laser processing. *Materials Research Express*, 5(11), 115001.

- Ensikat, H. J., Ditsche-Kuru, P., Neinhuis, C., & Barthlott, W. (2011). Superhydrophobicity in perfection: the outstanding properties of the lotus leaf. *Beilstein Journal of Nanotechnology*, 2(1), 152-161.
- Ensikat, H. J., Ditsche-Kuru, P., Neinhuis, C., & Barthlott, W. (2011). Superhydrophobicity in perfection: the outstanding properties of the lotus leaf. *Beilstein Journal of Nanotechnology*, 2, 152-161.
doi:10.3762/bjnano.2.19
- Eral, H. B., 't Mannetje, D. J. C. M., & Oh, J. M. (2013). Contact angle hysteresis: a review of fundamentals and applications. *Colloid and Polymer Science*, 291(2), 247-260. doi:10.1007/s00396-012-2796-6
- Erbil, H. Y. (2020). Practical Applications of Superhydrophobic Materials and Coatings: Problems and Perspectives. *Langmuir*, 36(10), 2493-2509.
doi:10.1021/acs.langmuir.9b03908
- Faisal, N., Zindani, D., Kumar, K., & Bhowmik, S. (2019). Laser micromachining of engineering materials—a review. In *Micro and Nano Machining of Engineering Materials* (pp. 121-136): Springer.
- Fan, Y., Chen, Z., Liang, J., Wang, Y., & Chen, H. (2014). Preparation of superhydrophobic films on copper substrate for corrosion protection. *Surface and Coatings Technology*, 244, 1-8.
doi:<https://doi.org/10.1016/j.surfcoat.2014.01.005>
- Fedorchenko, A. I., Wang, A.-B., & Wang, Y.-H. (2005). Effect of capillary and viscous forces on spreading of a liquid drop impinging on a solid surface. *Physics of Fluids*, 17(9), 093104.
- Feng, J., Wang, F.-C., & Zhao, Y. (2009). Electrowetting on a lotus leaf. *Biomicrofluidics*, 3 2, 22406.

- Feng, L., Li, S., Li, Y., Li, H., Zhang, L., Zhai, J., . . . Zhu, D. (2002). Superhydrophobic surfaces: from natural to artificial. *Advanced materials*, 14(24), 1857-1860.
- Forbes, P. (2008). Self-cleaning materials. *Scientific American*, 299(2), 88-95.
- Forsberg, P., Nikolajeff, F., & Karlsson, M. (2011). Cassie–Wenzel and Wenzel–Cassie transitions on immersed superhydrophobic surfaces under hydrostatic pressure. *Soft Matter*, 7(1), 104-109.
- Frenkel, Y. I. (2005). On the behavior of liquid drops on a solid surface. 1. The sliding of drops on an inclined surface. *arXiv preprint physics/0503051*.
- Fujimoto, H., & Hatta, N. (1996). Deformation and rebounding processes of a water droplet impinging on a flat surface above Leidenfrost temperature.
- Furmidge, C. (1962). Studies at phase interfaces. I. The sliding of liquid drops on solid surfaces and a theory for spray retention. *Journal of colloid science*, 17(4), 309-324.
- Gao, W., & Li, Z. (2010). 21 - Nanostructured transition metal oxides and their applications in composites. In S. C. Tjong & Y. W. Mai (Eds.), *Physical Properties and Applications of Polymer Nanocomposites* (pp. 723-742): Woodhead Publishing.
- Ge, S., Liu, W., Zhou, S., Li, S., Sun, X., Huang, Y., . . . Lin, D. (2018). Design and preparation of a micro-pyramid structured thin film for broadband infrared antireflection. *Coatings*, 8(5), 192.
- Gerbreders, V., Krasovska, M., Sledevskis, E., Gerbreders, A., Mihailova, I., Tamanis, E., & Ogurcovs, A. (2020). Hydrothermal synthesis of ZnO nanostructures with controllable morphology change. *CrystEngComm*, 22(8), 1346-1358.

- Good, R. J. (1992). Contact angle, wetting, and adhesion: a critical review. *Journal of Adhesion Science and Technology*, 6(12), 1269-1302.
- Gregorčič, P., Šetina-Batič, B., & Hočevar, M. (2017). Controlling the stainless steel surface wettability by nanosecond direct laser texturing at high fluences. *Applied Physics A*, 123(12), 766.
- Guo, L., Gu, C., Feng, J., Guo, Y., Jin, Y., & Tu, J. (2020). Hydrophobic epoxy resin coating with ionic liquid conversion pretreatment on magnesium alloy for promoting corrosion resistance. *Journal of Materials Science & Technology*, 37, 9-18.
- Hao, C., Li, J., Liu, Y., Zhou, X., Liu, Y., Liu, R., . . . Li, L. (2015). Superhydrophobic-like tunable droplet bouncing on slippery liquid interfaces. *Nature Communications*, 6(1), 1-7.
- Hatefi, S., & Abou-El-Hossein, K. (2020). Review of single-point diamond turning process in terms of ultra-precision optical surface roughness. *The International Journal of Advanced Manufacturing Technology*, 106(5), 2167-2187.
- He, S., Shi, J., Huang, J., Hu, J., Lai, Y., & Chen, Z. (2021). Rational designed structured superhydrophobic iron oxide surface towards sustainable anti-corrosion and self-cleaning. *Chemical Engineering Journal*, 416, 127768.
- Hosono, E., Fujihara, S., Honma, I., & Zhou, H. (2005). Superhydrophobic perpendicular nanopin film by the bottom-up process. *Journal of the American Chemical Society*, 127(39), 13458-13459.
- Hu, H., Chen, L., Huang, S., & Song, B. (2013). Rebound behaviors of droplets impacting on a superhydrophobic surface. *Science China Physics, Mechanics and Astronomy*, 56(5), 960-965.

- Hu, J., He, S., Wang, Z., Zhu, J., Wei, L., & Chen, Z. (2019). Stearic acid-coated superhydrophobic Fe₂O₃/Fe₃O₄ composite film on N80 steel for corrosion protection. *Surface and Coatings Technology*, 359, 47-54.
doi:<https://doi.org/10.1016/j.surfcoat.2018.12.040>
- Huang, S., Yu, N., Wang, T., & Li, J. (2018). Simple fabrication of UV photo-detector based on NiO/ZnO structure grown by hydrothermal process. *Functional Materials Letters*, 11(02), 1850045.
- Huang, Y., Sarkar, D. K., Gallant, D., & Chen, X.-G. (2013). Corrosion resistance properties of superhydrophobic copper surfaces fabricated by one-step electrochemical modification process. *Applied Surface Science*, 282, 689-694.
- Huang, Z., Wang, X., Sun, F., Fan, C., Sun, Y., Jia, F., . . . Liu, B. (2021). Super response and selectivity to H₂S at room temperature based on CuO nanomaterials prepared by seed-induced hydrothermal growth. *Materials & Design*, 201, 109507.
- Jeevahan, J., Chandrasekaran, M., Joseph, G. B., Durairaj, R., & Mageshwaran, G. (2018). Superhydrophobic surfaces: A review on fundamentals, applications, and challenges. *Journal of Coatings Technology and Research*, 1-20.
- Jeffree, C. (1986). The cuticle, epicuticular waxes and trichomes of plants, with reference to their structure, functions and evolution. *Insects and the plant surface*. Edward Arnold: London, 23-64.
- Jeong, S.-W., Bolortuya, S., Eadi, S. B., & Kim, S. (2020). Fabrication of superhydrophobic surfaces based on PDMS coated hydrothermal grown

- ZnO on PET fabrics. *Journal of Adhesion Science and Technology*, 34(1), 102-113.
- Jiang, L., Wang, R., Yang, B., Li, T., Tryk, D., Fujishima, A., . . . Zhu, D. (2000). Binary cooperative complementary nanoscale interfacial materials. *Pure and applied chemistry*, 72(1-2), 73-81.
- Jung, Y. C., & Bhushan, B. (2008). Dynamic effects of bouncing water droplets on superhydrophobic surfaces. *Langmuir*, 24(12), 6262-6269.
- Jung, Y. C., & Bhushan, B. (2009). Mechanically durable carbon nanotube–composite hierarchical structures with superhydrophobicity, self-cleaning, and low-drag. *ACS nano*, 3(12), 4155-4163.
- Jung, Y. C., & Bhushan, B. (2010). Biomimetic structures for fluid drag reduction in laminar and turbulent flows. *Journal of Physics-Condensed Matter*, 22(3). doi:10.1088/0953-8984/22/3/035104
- Kang, C., Lu, H., Yuan, S., Hong, D., Yan, K., & Liang, B. (2012). Superhydrophilicity/superhydrophobicity of nickel micro-arrays fabricated by electroless deposition on an etched porous aluminum template. *Chemical Engineering Journal*, 203, 1-8.
- Kashaninejad, N., Nguyen, N.-T., & Chan, W. K. (2012). Eccentricity effects of microhole arrays on drag reduction efficiency of microchannels with a hydrophobic wall. *Physics of Fluids*, 24(11), 112004.
- Khojasteh, D., Manshadi, M. D., Mousavi, S. M., & Kamali, R. (2016). *Droplet impact on superhydrophobic surface under the influence of an electric field*. Paper presented at the annual meeting for 3rd Annual International Conference on New Research Achievements in Chemistry & Chemical Engineering, Tehran, Iran, September.

- Kietzig, A.-M., Negar Mirvakili, M., Kamal, S., Englezos, P., & Hatzikiriakos, S. G. (2011). Laser-patterned super-hydrophobic pure metallic substrates: Cassie to Wenzel wetting transitions. *Journal of Adhesion Science and Technology*, 25(20), 2789-2809.
- Kim, H., Lee, C., Kim, M. H., & Kim, J. (2012). Drop Impact Characteristics and Structure Effects of Hydrophobic Surfaces with Micro- and/or Nanoscaled Structures. *Langmuir*, 28(30), 11250-11257.
doi:10.1021/la302215n
- Koch, K., Bhushan, B., & Barthlott, W. (2009). Multifunctional surface structures of plants: An inspiration for biomimetics. *Progress in Materials Science*, 54(2), 137-178.
doi:<https://doi.org/10.1016/j.pmatsci.2008.07.003>
- Koch, K., Bhushan, B., Jung, Y. C., & Barthlott, W. (2009). Fabrication of artificial Lotus leaves and significance of hierarchical structure for superhydrophobicity and low adhesion. *Soft Matter*, 5(7), 1386-1393.
doi:10.1039/B818940D
- Koishi, T., Yasuoka, K., Fujikawa, S., Ebisuzaki, T., & Zeng, X. C. (2009). Coexistence and transition between Cassie and Wenzel state on pillared hydrophobic surface. *Proceedings of the National Academy of Sciences*, 106(21), 8435-8440.
- Kong, L., Chen, X., Yang, G., Yu, L., & Zhang, P. (2008). Preparation and characterization of slice-like $\text{Cu}_2(\text{OH})_3\text{NO}_3$ superhydrophobic structure on copper foil. *Applied Surface Science*, 254(22), 7255-7258.

- Krasovitski, B., & Marmur, A. (2005). Drops down the hill: theoretical study of limiting contact angles and the hysteresis range on a tilted plate. *Langmuir*, 21(9), 3881-3885.
- Krishnan, A., Liu, Y.-H., Cha, P., Woodward, R., Allara, D., & Vogler, E. A. (2005). An evaluation of methods for contact angle measurement. *Colloids and Surfaces B: Biointerfaces*, 43(2), 95-98.
- Kurokawa, Y., Nagai, K., Huan, P. D., Shimazaki, K., Qu, H., Mori, Y., . . . Ashikari, M. (2018). Rice leaf hydrophobicity and gas films are conferred by a wax synthesis gene (LGF1) and contribute to flood tolerance. *New Phytologist*, 218(4), 1558-1569. doi:<https://doi.org/10.1111/nph.15070>
- Kwon, Y., Patankar, N., Choi, J., & Lee, J. (2009). Design of surface hierarchy for extreme hydrophobicity. *Langmuir*, 25(11), 6129-6136.
- Laan, N., de Bruin, K. G., Bartolo, D., Josserand, C., & Bonn, D. (2014). Maximum diameter of impacting liquid droplets. *Physical Review Applied*, 2(4), 044018.
- Lakehal, D., Narayanan, C., Caviezel, D., von Rickenbach, J., & Reboux, S. (2013). Progress in computational microfluidics using TransAT. *Microfluidics and nanofluidics*, 15(3), 415-429.
- Lan, X., Zhang, B., Wang, J., Fan, X., & Zhang, J. (2021). Hydrothermally structured superhydrophobic surface with superior anti-corrosion, anti-bacterial and anti-icing behaviors. *Colloids and Surfaces A: Physicochemical and Engineering Aspects*, 624, 126820.
- Lathe, S. S., Gurav, A. B., Maruti, C. S., & Vhatkar, R. S. (2012). Recent progress in preparation of superhydrophobic surfaces: a review. *Journal of Surface Engineered Materials and Advanced Technology*, 2(02), 76.

- Latthe, S. S., Sutar, R. S., Kodag, V. S., Bhosale, A. K., Kumar, A. M., Kumar Sadasivuni, K., . . . Liu, S. (2019). Self – cleaning superhydrophobic coatings: Potential industrial applications. *Progress in Organic Coatings*, 128, 52-58. doi:<https://doi.org/10.1016/j.porgcoat.2018.12.008>
- Latthe, S. S., Terashima, C., Nakata, K., & Fujishima, A. (2014). Superhydrophobic surfaces developed by mimicking hierarchical surface morphology of lotus leaf. *Molecules*, 19(4), 4256-4283.
- Lee, C., Choi, C.-H., & Kim, C.-J. (2016). Superhydrophobic drag reduction in laminar flows: a critical review. *Experiments in Fluids*, 57(12), 176.
- Lee, J. B., & Lee, S. H. (2011). Dynamic wetting and spreading characteristics of a liquid droplet impinging on hydrophobic textured surfaces. *Langmuir*, 27(11), 6565-6573.
- Li, D., Ma, L., Zhang, B., & Chen, S. (2021). Large-scale fabrication of a durable and self-healing super-hydrophobic coating with high thermal stability and long-term corrosion resistance. *Nanoscale*, 13(16), 7810-7821.
- Li, D., Wang, B., Tong, Z., Blunt, L., & Jiang, X. (2019). On-machine surface measurement and applications for ultra-precision machining: a state-of-the-art review. *The International Journal of Advanced Manufacturing Technology*, 104(1-4), 831-847.
- Li, L., & Allen, Y. Y. (2011). Design and fabrication of a freeform microlens array for uniform beam shaping. *Microsystem technologies*, 17(12), 1713-1720.

- Li, L., & Allen, Y. Y. (2012). Design and fabrication of a freeform microlens array for a compact large-field-of-view compound-eye camera. *Applied optics*, 51(12), 1843-1852.
- Li, P., Chen, X., Yang, G., Yu, L., & Zhang, P. (2014). Preparation of silver-cuprous oxide/stearic acid composite coating with superhydrophobicity on copper substrate and evaluation of its friction-reducing and anticorrosion abilities. *Applied Surface Science*, 289, 21-26.
- Liang, Q., Qiao, F., Cui, X., & Hou, X. (2019). Controlling the morphology of ZnO structures via low temperature hydrothermal method and their optoelectronic application. *Materials Science in Semiconductor Processing*, 89, 154-160.
- Liu, M., Zheng, Y., Zhai, J., & Jiang, L. (2010). Bioinspired Super-antiwetting Interfaces with Special Liquid–Solid Adhesion. *Accounts of Chemical Research*, 43(3), 368-377. doi:10.1021/ar900205g
- Liu, T., Chen, S., Cheng, S., Tian, J., Chang, X., & Yin, Y. (2007). Corrosion behavior of super-hydrophobic surface on copper in seawater. *Electrochimica Acta*, 52(28), 8003-8007.
- Liu, Y., Li, S., Zhang, J., Liu, J., Han, Z., & Ren, L. (2015). Corrosion inhibition of biomimetic super-hydrophobic electrodeposition coatings on copper substrate. *Corrosion Science*, 94, 190-196.
doi:<https://doi.org/10.1016/j.corsci.2015.02.009>
- Liu, Y., Moevius, L., Xu, X., Qian, T., Yeomans, J. M., & Wang, Z. (2014). Pancake bouncing on superhydrophobic surfaces. *Nature Physics*, 10(7), 515-519. doi:10.1038/nphys2980

- Liu, Y., Whyman, G., Bormashenko, E., Hao, C., & Wang, Z. (2015). Controlling drop bouncing using surfaces with gradient features. *Applied physics letters*, *107*(5), 051604.
- Long, C. J., Schumacher, J. F., & Brennan, A. B. (2009). Potential for tunable static and dynamic contact angle anisotropy on gradient microscale patterned topographies. *Langmuir*, *25*(22), 12982-12989.
- Long, J., Zhong, M., Fan, P., Gong, D., & Zhang, H. (2015). Wettability conversion of ultrafast laser structured copper surface. *Journal of Laser Applications*, *27*(S2), S29107.
- Long, J., Zhong, M., Zhang, H., & Fan, P. (2015). Superhydrophilicity to superhydrophobicity transition of picosecond laser microstructured aluminum in ambient air. *Journal of Colloid and Interface Science*, *441*, 1-9.
- Lu, H., Lee, D.-W., Lee, S.-M., & Park, J.-W. (2012). Diamond machining of sinusoidal grid surface using fast tool servo system for fabrication of hydrophobic surface. *Transactions of Nonferrous Metals Society of China*, *22*, s787-s792. doi:[https://doi.org/10.1016/S1003-6326\(12\)61805-6](https://doi.org/10.1016/S1003-6326(12)61805-6)
- Lv, C., Yang, C., Hao, P., He, F., & Zheng, Q. (2010). Sliding of Water Droplets on Microstructured Hydrophobic Surfaces. *Langmuir*, *26*(11), 8704-8708. doi:10.1021/la9044495
- Ma, M., & Hill, R. M. (2006). Superhydrophobic surfaces. *Current opinion in colloid & interface science*, *11*(4), 193-202.
- Mali, S. S., Betty, C. A., Bhosale, P. N., Patil, P. S., & Hong, C. K. (2014). From nanocorals to nanorods to nanoflowers nanoarchitecture for efficient dye-

sensitized solar cells at relatively low film thickness: All Hydrothermal Process. *Scientific Reports*, 4, 5451. doi:10.1038/srep05451

<https://www.nature.com/articles/srep05451#supplementary-information>

Marmur, A., & Bittoun, E. (2009). When Wenzel and Cassie are right: reconciling local and global considerations. *Langmuir*, 25(3), 1277-1281.

Meng, H., Wang, S., Xi, J., Tang, Z., & Jiang, L. (2008). Facile means of preparing superamphiphobic surfaces on common engineering metals. *The Journal of Physical Chemistry C*, 112(30), 11454-11458.

Mittal, K. L. (2003). *Contact Angle, Wettability and Adhesion, Volume 3* (Vol. 3): CRC Press.

Mohamed, A. M. A., Abdullah, A. M., & Younan, N. A. (2015). Corrosion behavior of superhydrophobic surfaces: A review. *Arabian Journal of Chemistry*, 8(6), 749-765.

doi:<https://doi.org/10.1016/j.arabjc.2014.03.006>

Montes Ruiz-Cabello, F., Rodríguez-Valverde, M., Marmur, A., & Cabrerizo-Vílchez, M. (2011). Comparison of sessile drop and captive bubble methods on rough homogeneous surfaces: a numerical study. *Langmuir*, 27(15), 9638-9643.

Može, M., Zupančič, M., Hočevár, M., Golobič, I., & Gregorčič, P. (2019). Surface chemistry and morphology transition induced by critical heat flux incipience on laser-textured copper surfaces. *Applied Surface Science*.

Müller, M., & Oehr, C. (2011). Comments on “an essay on contact angle measurements” by Strobel and Lyons. *Plasma Processes and Polymers*, 8(1), 19-24.

- Neužil, P., Giselbrecht, S., Länge, K., Huang, T. J., & Manz, A. (2012). Revisiting lab-on-a-chip technology for drug discovery. *Nature reviews Drug discovery*, *11*(8), 620-632.
- Nikam, A. V., Prasad, B. L. V., & Kulkarni, A. A. (2018). Wet chemical synthesis of metal oxide nanoparticles: a review. *CrystEngComm*, *20*(35), 5091-5107. doi:10.1039/C8CE00487K
- Nosonovsky, M. (2007). On the range of applicability of the Wenzel and Cassie equations. *Langmuir*, *23*(19), 9919-9920.
- Nosonovsky, M., & Bhushan, B. (2008). Energy transitions in superhydrophobicity: low adhesion, easy flow and bouncing. *Journal of Physics: Condensed Matter*, *20*(39), 395005.
- Okumura, K., Chevy, F., Richard, D., Quéré, D., & Clanet, C. (2003). Water spring: A model for bouncing drops. *EPL (Europhysics Letters)*, *62*(2), 237.
- Onda, T., Shibuichi, S., Satoh, N., & Tsujii, K. (1996). Super-water-repellent fractal surfaces. *Langmuir*, *12*(9), 2125-2127.
- Öner, D., & McCarthy, T. J. (2000). Ultrahydrophobic surfaces. Effects of topography length scales on wettability. *Langmuir*, *16*(20), 7777-7782.
- Ou, J., Moss, G. R., & Rothstein, J. P. (2007). Enhanced mixing in laminar flows using ultrahydrophobic surfaces. *Physical Review E*, *76*(1), 016304.
- Ou, P., Zhou, Q., Li, J., Chen, W., Huang, J., Yang, L., . . . Sheng, M. (2019). Facile ethylene glycol-assisted hydrothermal synthesis of MoO₂ nanospheres for high-performance supercapacitors. *Materials Research Express*, *6*(9), 095044.

- Panão, M. R., & Moreira, A. L. (2009). Intermittent spray cooling: a new technology for controlling surface temperature. *International Journal of Heat and Fluid Flow*, 30(1), 117-130.
- Pasandideh-Fard, M., Qiao, Y., Chandra, S., & Mostaghimi, J. (1996). Capillary effects during droplet impact on a solid surface. *Physics of Fluids*, 8(3), 650-659.
- Patankar, N. A. (2003). On the modeling of hydrophobic contact angles on rough surfaces. *Langmuir*, 19(4), 1249-1253.
- Petlin, D. G., Tverdokhlebov, S. I., & Anissimov, Y. G. (2017). Plasma treatment as an efficient tool for controlled drug release from polymeric materials: A review. *Journal of Controlled Release*, 266, 57-74.
doi:<https://doi.org/10.1016/j.jconrel.2017.09.023>
- Pierce, E., Carmona, F., & Amirfazli, A. (2008). Understanding of sliding and contact angle results in tilted plate experiments. *Colloids and Surfaces A: Physicochemical and Engineering Aspects*, 323(1-3), 73-82.
- Prado, L. A. S. A., Sriyai, M., Ghislandi, M., Barros-Timmons, A., & Schulte, K. (2010). Surface modification of alumina nanoparticles with silane coupling agents. *Journal of the Brazilian Chemical Society*, 21, 2238-2245. Retrieved from
http://www.scielo.br/scielo.php?script=sci_arttext&pid=S0103-50532010001200010&nrm=iso
- Renardy, Y., Popinet, S., Duchemin, L., Renardy, M., Zaleski, S., Josserand, C., . . . Quéré, D. (2003). Pyramidal and toroidal water drops after impact on a solid surface.

- Reyssat, M., & Quéré, D. (2009). Contact angle hysteresis generated by strong dilute defects. *The Journal of Physical Chemistry B*, 113(12), 3906-3909.
- Richard, D., Clanet, C., & Quéré, D. (2002). Contact time of a bouncing drop. *Nature*, 417(6891), 811-811. doi:10.1038/417811a
- Richard, D., & Quéré, D. (2000). Bouncing water drops. *Europhysics Letters (EPL)*, 50(6), 769-775. doi:10.1209/epl/i2000-00547-6
- Ridhuan, N. S., Razak, K. A., & Lockman, Z. (2018). Fabrication and Characterization of Glucose Biosensors by Using Hydrothermally Grown ZnO Nanorods. *Scientific Reports*, 8(1), 13722.
- Rioboo, R., Tropea, C., & Marengo, M. (2001). Outcomes from a drop impact on solid surfaces. *Atomization and sprays*, 11(2).
- Rothstein, J. P. (2010). Slip on Superhydrophobic Surfaces. *Annual Review of Fluid Mechanics*, 42(1), 89-109. doi:10.1146/annurev-fluid-121108-145558
- Ryu, J., Kim, K., Park, J., Hwang, B. G., Ko, Y., Kim, H., . . . Lee, S. J. (2017). Nearly perfect durable superhydrophobic surfaces fabricated by a simple one-step plasma treatment. *Scientific Reports*, 7(1), 1-8.
- Sarkar, D. K., & Farzaneh, M. (2009). Superhydrophobic coatings with reduced ice adhesion. *Journal of Adhesion Science and Technology*, 23(9), 1215-1237.
- Schneider, F., Das, J., Kirsch, B., Linke, B., & Aurich, J. C. (2019). Sustainability in ultra precision and micro machining: a review. *International Journal of Precision Engineering and Manufacturing-Green Technology*, 6(3), 601-610.

- Sethi, S. K., & Manik, G. (2018). Recent Progress in Super Hydrophobic/Hydrophilic Self-Cleaning Surfaces for Various Industrial Applications: A Review. *Polymer-Plastics Technology and Engineering*, 57(18), 1932-1952. doi:10.1080/03602559.2018.1447128
- She, Z., Li, Q., Wang, Z., Li, L., Chen, F., & Zhou, J. (2012). Novel Method for Controllable Fabrication of a Superhydrophobic CuO Surface on AZ91D Magnesium Alloy. *ACS applied materials & interfaces*, 4(8), 4348-4356. doi:10.1021/am3009949
- Shen, S. F., Xu, M. L., Lin, D. B., & Pan, H. B. (2017). The growth of urchin-like Co₃O₄ directly on sensor substrate and its gas sensing properties. *Applied Surface Science*, 396, 327-332.
- Shen, Y., Tao, J., Tao, H., Chen, S., Pan, L., & Wang, T. (2015). Approaching the theoretical contact time of a bouncing droplet on the rational macrostructured superhydrophobic surfaces. *Applied physics letters*, 107(11), 111604.
- Shen, Y., Tao, J., Tao, H., Chen, S., Pan, L., & Wang, T. (2015). Relationship between wetting hysteresis and contact time of a bouncing droplet on hydrophobic surfaces. *ACS applied materials & interfaces*, 7(37), 20972-20978.
- Shi, W., Song, S., & Zhang, H. (2013). Hydrothermal synthetic strategies of inorganic semiconducting nanostructures. *Chemical Society Reviews*, 42(13), 5714-5743.
- Shumakovich, G. P., Otrokhov, G. V., Khlupova, M. E., Vasil'eva, I. S., Zaitseva, E. A., Morozova, O. V., & Yaropolov, A. I. (2014). Laccase-catalyzed synthesis of aniline oligomers and their application for the

- protection of copper against corrosion. *RSC advances*, 4(57), 30193-30196.
- Sinapi, F., Julien, S., Auguste, D., Hevesi, L., Delhalle, J., & Mekhalif, Z. (2008). Monolayers and mixed-layers on copper towards corrosion protection. *Electrochimica Acta*, 53(12), 4228-4238.
- Song, H.-J., Shen, X.-Q., Ji, H.-Y., & Jing, X.-J. (2010). Superhydrophobic iron material surface with flower-like structures obtained by a facile self-assembled monolayer. *Applied Physics A*, 99(3), 685-689.
- Strobel, M., & Lyons, C. S. (2011). An Essay on Contact Angle Measurements. *Plasma Processes and Polymers*, 8(1), 8-13.
doi:10.1002/ppap.201000041
- Su, F., & Yao, K. (2014). Facile fabrication of superhydrophobic surface with excellent mechanical abrasion and corrosion resistance on copper substrate by a novel method. *ACS applied materials & interfaces*, 6(11), 8762-8770.
- Sun, M., Watson, G. S., Watson, J. A., Zheng, Y., Jiang, L., Han, D., & Liang, A. (2014). Wettability and adhesional differences on a natural template: the cicada wing. *Science of Advanced Materials*, 6(7), 1493-1500.
- Sun, Y.-Y., Zong, Z.-M., Li, Z.-K., & Wei, X.-Y. (2018). Hydrothermal synthesis of TiO₂ nanotubes from one-dimensional TiO₂ nanowires on flexible non-metallic substrate. *Ceramics International*, 44(3), 3501-3504.
- Sun, Y., & Guo, Z. (2019). Recent advances of bioinspired functional materials with specific wettability: from nature and beyond nature. *Nanoscale Horizons*, 4(1), 52-76.

- Ta, D. V., Dunn, A., Wasley, T. J., Kay, R. W., Stringer, J., Smith, P. J., . . . Shephard, J. D. (2015). Nanosecond laser textured superhydrophobic metallic surfaces and their chemical sensing applications. *Applied Surface Science*, *357*, 248-254.
- Tadmor, R., Bahadur, P., Leh, A., N'guessan, H. E., Jaini, R., & Dang, L. (2009). Measurement of lateral adhesion forces at the interface between a liquid drop and a substrate. *Physical Review Letters*, *103*(26), 266101.
- Takino, H., Kanaoka, M., & Nomura, K. (2011). *Ultraprecision machining of optical surfaces*. Paper presented at the Proc. ISUPEN (2011 JSPE Spring Meeting).
- Thirumalai, K., Shanthi, M., & Swaminathan, M. (2019). Ho₂WO₆/ZnO nanoflakes for photo–electrochemical and self cleaning applications. *Materials Science in Semiconductor Processing*, *90*, 78-86.
doi:<https://doi.org/10.1016/j.mssp.2018.10.007>
- Trdan, U., Hočevár, M., & Gregorčič, P. (2017). Transition from superhydrophilic to superhydrophobic state of laser textured stainless steel surface and its effect on corrosion resistance. *Corrosion Science*, *123*, 21-26.
- Tsai, P., Pacheco, S., Pirat, C., Lefferts, L., & Lohse, D. (2009). Drop impact upon micro-and nanostructured superhydrophobic surfaces. *Langmuir*, *25*(20), 12293-12298.
- Ukiwe, C., & Kwok, D. Y. (2005). On the Maximum Spreading Diameter of Impacting Droplets on Well-Prepared Solid Surfaces. *Langmuir*, *21*(2), 666-673. doi:10.1021/la0481288

- Varanasi, K. K., Deng, T., Hsu, M., & Bhate, N. (2009). Hierarchical superhydrophobic surfaces resist water droplet impact.
- Vazirinasab, E., Jafari, R., & Momen, G. (2018). Application of superhydrophobic coatings as a corrosion barrier: A review. *Surface and Coatings Technology*, 341, 40-56.
doi:<https://doi.org/10.1016/j.surfcoat.2017.11.053>
- Volpe, C. D., & Siboni, S. (2018). The Wilhelmy method: a critical and practical review. *Surface Innovations*, 6(3), 120-132.
- Wachters, L., & Westerling, N. (1966). The heat transfer from a hot wall to impinging water drops in the spheroidal state. *Chemical Engineering Science*, 21(11), 1047-1056.
- Wan, Y., Chen, M., Liu, W., Shen, X., Min, Y., & Xu, Q. (2018). The research on preparation of superhydrophobic surfaces of pure copper by hydrothermal method and its corrosion resistance. *Electrochimica Acta*, 270, 310-318.
- Wang, B.-B., Zhao, Y.-P., & Yu, T. (2011). Fabrication of Novel Superhydrophobic Surfaces and Droplet Bouncing Behavior — Part 2: Water Droplet Impact Experiment on Superhydrophobic Surfaces Constructed Using ZnO Nanoparticles. *Journal of Adhesion Science and Technology*, 25(1-3), 93-108. doi:10.1163/016942410X501115
- Wang, P., Zhang, D., & Qiu, R. (2012). Liquid/solid contact mode of superhydrophobic film in aqueous solution and its effect on corrosion resistance. *Corrosion Science*, 54, 77-84.
doi:<https://doi.org/10.1016/j.corsci.2011.08.050>
- Wang, S., & Jiang, L. (2007). Definition of superhydrophobic states.

- Wang, Z., Cong, Y., & Zhang, B. (2016). Controllable wetting state high adhesion hydrophobic surface. *RSC advances*, 6(76), 72815-72820.
- Wang, Z., Lopez, C., Hirska, A., & Koratkar, N. (2007). Impact dynamics and rebound of water droplets on superhydrophobic carbon nanotube arrays. *Applied physics letters*, 91(2), 023105.
- Weisensee, P. B., Tian, J., Miljkovic, N., & King, W. P. (2016). Water droplet impact on elastic superhydrophobic surfaces. *Scientific Reports*, 6, 30328.
- Wenzel, R. N. (1936). Resistance of solid surfaces to wetting by water. *Industrial & Engineering Chemistry*, 28(8), 988-994.
- Worthington, A. M. (1908). *A study of splashes*: Longmans, Green, and Company.
- Wu, B., Zhou, M., Li, J., Ye, X., Li, G., & Cai, L. (2009). Superhydrophobic surfaces fabricated by microstructuring of stainless steel using a femtosecond laser. *Applied Surface Science*, 256(1), 61-66.
- Wu, W., Zhang, F., Li, Y., Song, L., Jiang, D., Zeng, R.-C., . . . Chen, D.-C. (2020). Corrosion resistance of dodecanethiol-modified magnesium hydroxide coating on AZ31 magnesium alloy. *Applied Physics A*, 126(1), 1-11.
- Xiao, F., Yuan, S., Liang, B., Li, G., Pehkonen, S. O., & Zhang, T. (2015). Superhydrophobic CuO nanoneedle-covered copper surfaces for anticorrosion. *Journal of Materials Chemistry A*, 3(8), 4374-4388.
- Xu, H., Wang, W., & Zhu, W. (2006). Shape evolution and size-controllable synthesis of Cu₂O octahedra and their morphology-dependent photocatalytic properties. *The Journal of Physical Chemistry B*, 110(28), 13829-13834.

- Yan, Y., Liu, X., Xiong, H., Zhou, J., Yu, H., Qin, C., & Wang, Z. (2020). Stearic Acid Coated MgO Nanoplate Arrays as Effective Hydrophobic Films for Improving Corrosion Resistance of Mg-Based Metallic Glasses. *Nanomaterials*, 10(5), 947.
- Yan, Y. Y., Gao, N., & Barthlott, W. (2011). Mimicking natural superhydrophobic surfaces and grasping the wetting process: A review on recent progress in preparing superhydrophobic surfaces. *Advances in colloid and interface science*, 169(2), 80-105.
- Yang, C., Wang, F., Li, W., Ou, J., Li, C., & Amirfazli, A. (2016). Anti-icing properties of superhydrophobic ZnO/PDMS composite coating. *Applied Physics A*, 122(1), 1.
- Yang, M., Liu, W., Jiang, C., He, S., Xie, Y., & Wang, Z. (2018). Fabrication of superhydrophobic cotton fabric with fluorinated TiO₂ sol by a green and one-step sol-gel process. *Carbohydrate polymers*, 197, 75-82.
- Yarin, A. L. (2006). Drop impact dynamics: splashing, spreading, receding, bouncing.... *Annu. Rev. Fluid Mech.*, 38, 159-192.
- Yi, M., Liu, L., Wu, L., & Li, X. (2019). Research on sliding angles of water droplets on the hierarchical structured superhydrophobic surfaces. *Applied Physics A*, 126(1), 47. doi:10.1007/s00339-019-3137-0
- Young, T. (1832). *An essay on the cohesion of fluids*. Paper presented at the Abstracts of the Papers Printed in the Philosophical Transactions of the Royal Society of London.
- Yuan, J., Lyu, B., Hang, W., & Deng, Q. (2017). Review on the progress of ultra-precision machining technologies. *Frontiers of Mechanical Engineering*, 12(2), 158-180. doi:10.1007/s11465-017-0455-9

- Yuan, Z. Q., Hao, X. H., Bin, J. P., Wang, X., & Chen, H. (2012). Preparation and Characterization of Nickel Oxide-Based Superhydrophobic Surface. *Advanced Materials Research*, 557-559, 1807-1810. doi:10.4028/www.scientific.net/AMR.557-559.1807
- Yusof, A., Keegan, H., Spillane, C. D., Sheils, O. M., Martin, C. M., O'Leary, J. J., . . . Koltay, P. (2011). Inkjet-like printing of single-cells. *Lab on a Chip*, 11(14), 2447-2454.
- Zhai, J., Li, H.-J., Li, Y.-S., Li, S.-H., & Jiang, L. (2002). Discovery of super-amphiphobic properties of aligned carbon nanotube films. *PHYSICS-BEIJING-*, 31(8), 483-486.
- Zhang, F., Shi, Z., Chen, L., Jiang, Y., Xu, C., Wu, Z., . . . Peng, C. (2017). Porous superhydrophobic and superoleophilic surfaces prepared by template assisted chemical vapor deposition. *Surface and Coatings Technology*, 315, 385-390.
- Zhang, J.-P., Liu, W., Luo, Y., Chu, G.-W., Zou, H.-K., & Chen, J.-F. (2019). Enhancing liquid droplet breakup by hydrophobic wire mesh: Visual study and application in a rotating packed bed. *Chemical Engineering Science*, 209, 115180. doi:<https://doi.org/10.1016/j.ces.2019.115180>
- Zhang, Q., Zhang, K., Xu, D., Yang, G., Huang, H., Nie, F., . . . Yang, S. (2014). CuO nanostructures: synthesis, characterization, growth mechanisms, fundamental properties, and applications. *Progress in Materials Science*, 60, 208-337.
- Zhang, S., To, S., Wang, S., & Zhu, Z. (2015). A review of surface roughness generation in ultra-precision machining. *International Journal of Machine Tools and Manufacture*, 91, 76-95.

- Zhang, S., To, S., Zhu, Z., & Zhang, G. (2016). A review of fly cutting applied to surface generation in ultra-precision machining. *International Journal of Machine Tools and Manufacture*, 103, 13-27.
- Zhang, S., Zhou, Y., Zhang, H., Xiong, Z., & To, S. (2019). Advances in ultra-precision machining of micro-structured functional surfaces and their typical applications. *International Journal of Machine Tools and Manufacture*, 142, 16-41.
- Zhang, X., Shi, F., Niu, J., Jiang, Y., & Wang, Z. (2008). Superhydrophobic surfaces: from structural control to functional application. *Journal of Materials Chemistry*, 18(6), 621-633.
- Zhang, X., Zhang, J., Ren, Z., Li, X., Zhang, X., Zhu, D., . . . Yang, B. (2009). Morphology and wettability control of silicon cone arrays using colloidal lithography. *Langmuir*, 25(13), 7375-7382.
- Zhang, X., Zhao, J., Mo, J., Sun, R., Li, Z., & Guo, Z. (2019). Fabrication of superhydrophobic aluminum surface by droplet etching and chemical modification. *Colloids and Surfaces A: Physicochemical and Engineering Aspects*, 567, 205-212.
- Zhang, Z., Ge, B., Men, X., & Li, Y. (2016). Mechanically durable, superhydrophobic coatings prepared by dual-layer method for anti-corrosion and self-cleaning. *Colloids and Surfaces A: Physicochemical and Engineering Aspects*, 490, 182-188.
doi:<https://doi.org/10.1016/j.colsurfa.2015.11.049>
- Zhang, Z., Yan, J., & Kuriyagawa, T. (2019). Manufacturing technologies toward extreme precision. *International Journal of Extreme Manufacturing*.

- Zhao, T., & Jiang, L. (2018). Contact angle measurement of natural materials. *Colloids and Surfaces B: Biointerfaces*, *161*, 324-330.
doi:<https://doi.org/10.1016/j.colsurfb.2017.10.056>
- Zhao, W., Wang, L., & Xue, Q. (2010). Fabrication of low and high adhesion hydrophobic Au surfaces with micro/nano-biomimetic structures. *The Journal of Physical Chemistry C*, *114*(26), 11509-11514.
- Zhou, S., Zhu, X., & Yan, Q. (2018). One-step electrochemical deposition to achieve superhydrophobic cobalt incorporated amorphous carbon-based film with self-cleaning and anti-corrosion. *Surface and Interface Analysis*, *50*(3), 290-296.
- Zhu, J., & Hu, X. (2018). A new route for fabrication of the corrosion-resistant superhydrophobic surface by milling process. *Journal of Coatings Technology and Research*. doi:10.1007/s11998-018-0133-9